Hypsometric and Geometric Controls on

Hydrodynamics, Tidal Asymmetry, and Sediment Connectivity

in Shallow Estuarine Systems

A thesis

submitted in fulfilment

of the requirements for the degree

of

Doctor of Philosophy in Earth Sciences

at

The University of Waikato

by

Peter Jaap de Ruiter

THE UNIVERSITY OF
WAIKATO
Te Whare Wānanga o Waikato

2022

Abstract

Estuaries and tidal basins are highly dynamic coastal systems that serve as a transition zone between the river and the ocean. The morphological evolution of these diverse environments is modulated by non-linear feedbacks between tides, meteorological forcing, and sediment transport processes. This thesis focuses on the fundamental links between these physical processes, and the geomorphologic characteristics of shallow estuarine systems, specifically: (i) how shallow basin geometries and hypsometries affect hydrodynamics and tidal asymmetry, (ii) how wind-induced currents modify velocity asymmetry in shallow basins, and (iii) defining the relationships between geometry, hypsometry, and sediment connectivity inside shallow estuarine systems.

Linking geomorphological characteristics and tidal processes in shallow tidal basins

The links between tidal basin geometry and hypsometry, bed shear stress patterns, tidal velocity- and slack water asymmetry, and hypsometric profile shapes were explored for six shallow microtidal basins of Tauranga Harbour, New Zealand. Model results, obtained from a depth-averaged numerical model developed in Delft3D for the full estuarine system, indicated that tidal distortion increases with distance from basin entrance. A simple ratio between tidal basin width and entrance width was defined to describe the planform shape of the basin. This metric, termed the 'basin dilation factor' indicates whether a basin can be designated as a divergent or convergent geometry. Shallow basins with a constricted geometry and relatively deep entrance channels were found to be associated with small bed shear stress values and high rates of flood-directed tidal velocity asymmetry in the sheltered basin centres. These results suggest substantial potential for sediment deposition of larger particles. Moreover, slack water asymmetry within these basins was weakly ebb-directed, indicating a small potential for export of fine sediments. These divergent, depositional basins were found to be characterized by convex hypsometric profiles with elevated intertidal regions. Conversely, unconstricted, convergent basins were associated with larger bed shear stress values and more ebb-directed tidal velocity asymmetry within basin centres. Consequently, there was limited potential for overall sediment deposition inside these basins. The slack water asymmetry was weakly flood-dominant, suggesting limited potential for fine sediment input. The comparatively high-energy conditions within these exposed tidal basins were associated with a less convex hypsometric intertidal profile. This study highlights the impacts of

specific geomorphologic basin characteristics on tidal processes in shallow estuarine systems. The ability to predict the links between tidal asymmetry and morphological changes in tide-dominated systems is beneficial for coastal management, as the morphological evolution of estuarine systems affects coastal ecosystem functioning, port and estuary navigability, and potential for coastal protection.

Understanding the effects of wind-driven currents on velocity asymmetry in shallow tidal basins

Numerical modelling experiments were conducted for a series of idealized basins in which planform shape and bathymetry were varied. The model results were used to examine how wind-generated currents modulate horizontal velocity asymmetry patterns in shallow tidal basins. This study revealed that wind-driven currents primarily influence mean and peak flow velocities inside the basins, with a limited effect on tidal harmonics. Faster wind speeds led to more extreme horizontal velocity asymmetry (larger velocity asymmetry values), without substantially modifying overall spatial patterns of velocity asymmetry. The velocity asymmetry was found to be strongly depth-dependent, with changes to asymmetry patterns being most evident for wind speeds of 6 m/s and greater, and for wind directions parallel to the main axes of the tidal channels in the basins. Shallow intertidal regions inside the basins were characterized by a downwind-directed increase in velocity asymmetry, whereas deeper subtidal channels experienced asymmetry changes in the opposite direction. Wind event duration and timing were also found to influence the velocity asymmetry patterns. The differences between the relative size of the peak flood- and ebb directed currents were most evident for wind events with a duration of 6 hours or less that coincide with flooding tides. The results of this study highlight that hydrodynamics, sediment transport, and morphological evolution in shallow estuaries are modulated by tidal processes as well as meteorological forcing. Since anthropogenically induced climate change is expected to increase the intensity of extreme meteorological events, the ability to predict future pathways of morphological change in shallow estuarine systems, based on specific meteorological conditions as well as well-defined local tidal regimes, is vital for the management of these dynamic systems.

An examination of sediment connectivity in a shallow estuarine system

The sediment connectivity framework was used to examine links between hydrodynamics, sediment transport pathways, and local hypsometry inside a shallow estuarine system

(Tauranga Harbour, New Zealand). The estuary was divided into twenty geomorphic cells, representing tidal channels, intertidal flats, and shallow sub-basins. Depth-averaged numerical modelling simulations were carried out to quantify tide-driven sediment connectivity between the cells for five sediment grainsize classes. Connectivity matrices were developed for the different grainsize classes, based on modelled sediment mass loads. Sediment connectivity inside the estuary was found to be modulated by tidal energy, estuarine morphology (depth), sub-basin hypsometry and geometry (planform shape), and sediment characteristics. The connectivity matrices, combined with metrics such as link density and cell strength, illustrated that sediment mass loads, and hence connectivity, were largest in the high-energy environments of the deep tidal channels located in the main estuary. In the more sheltered upper estuary, and inside the shallow sub-basins, connectivity was reduced. For fine sediments (< 125 μm) connectivity was found to be substantial throughout the shallow estuarine system, with estuary-level connectivity (link density) being greater than 50%. Link density for coarser sediments (> 275 μm) was found to be ~20%, with transport pathways primarily confined to the deeper regions of the estuary. An in-depth analysis of sediment transport pathways between the shallow sub-basins emphasized that flood-dominant, divergent basins with a convex-shaped hypsometric profile mainly function as sediment sinks, whereas ebb-dominant convergent basins act as sediment sources.

This thesis highlights the substantial dependence of tidal asymmetry, morphology, sediment transport and connectivity on hypsometry, geometry, and grainsize characteristics inside shallow estuaries. Additionally, the effects of wind-driven currents on the non-linear physical processes inside these highly dynamic environments are described. Overall, this work provides a novel elucidation of some of the relationships between geometric parameters and forcing mechanisms applicable to many shallow coastal systems.

Acknowledgements

many people to list here individually, but I consider myself very lucky to have had the opportunity to get to know you all, and to enjoy your companionship and lunch conversations.

Thank you as well to friends and family in New Zealand and the Netherlands for all your support, especially my Mom, Dad, Erik, and the other wonderful people who have become my whānau in Hamilton and beyond.

Finally, but most importantly, thank you to my amazing partner Anna-Lena. Your emotional (and sometimes financial) support has been invaluable to me through the years since we met here in New Zealand. Of course, I cannot forget our little girl Leah, who was born a few years into my research, and who made the journey even more special. Thank you both for your never-ending support and encouragement through the difficult times; I'm not sure I could have completed this journey without you by my side.

Table of Contents

List of Figures

List of Tables

List of Symbols

ADCP	Acoustic Doppler Current Profiler	M_2	Semi-diurnal tidal constituent
a	basin area above specific elevation	$M_{2\theta}$	Semi-diurnal tidal constituent phase
A	total basin area	M_4	Quarter-diurnal tidal constituent
a/h	ratio between offshore tidal (M_2) amplitude and mean water depth	$M_{4\theta}$	Semi-diurnal tidal constituent phase
A_m	basin mouth cross-sectional area	M_6	Shallow water overtide (lunar)
BDF	Basin Dilation Factor	MAE	Mean Absolute Error
BSS	Brier Skill Score	MHWS	Mean High Water Spring
C	sediment concentration	MLOS	Mean Level Of the Sea
C_d	drag coeffient	MORFAC	Morphological Acceleration Factor
C_{ij}	Connectivity between basins i and j	m_{max}	maximum number of connections in matrix
D	link density	M_{tide}	sediment mass load over a tidal cycle
h	water depth	n	number of cells
H	maximum water depth	r	empirical hypsometry parameter
HWS	High Water Slack	RMSE	Root Mean Square Error
LiDAR	Light Detection and Ranging	S_b	maximum basin surface area
LWS	Low Water Slack		
m	number of connections in matrix		

SD	Standard Deviation	U_{m4}	M$_4$ tidal velocity component
SDA	Slack Duration Asymmetry	V	grid cell volume
S_{in}	Sediment import	VA	Velocity Asymmetry
S_n	normalised sediment load	VA_t	Velocity Asymmetry due to tides
S_{out}	Sediment export		
S_{tide}	Sediment transport over tidal cycle	VA_{tw}	Velocity Asymmetry due to tides and winds
T_TIDE	MATLAB package for classical harmonic analysis	W_{entr}	basin entrance width
		W_{est}	average width of landward half of basin
t	timestep		
t_{HWS}	high water slack duration	γ	Hypsometry exponent
t_{LWS}	low water slack duration	τ	bed shear stress
TVA	Tidal Velocity Asymmetry	τ_{max}	maximum bed shear stress
u	current velocity		
u_{cr}	critical entrainment velocity	**Other**	
		$<$	smaller than
u_{fl_max}	peak flood current velocity	$>$	larger than
u_{ebb_max}	peak ebb current velocity	$\approx$	approximately
U_{m2}	M$_2$ tidal velocity component	$\sum$	sum

Chapter 1

Introduction

1.1 General Introduction

Estuaries and tidal basins form a transition zone between fresh- and saltwater environments, and represent a vital part of the coastal ecosystem. These semi-enclosed bodies of water are encountered in a wide range of climatic zones and across a variety of tidal ranges, with over 1200 major estuarine systems covering a total area of roughly 500,000 km^2 mapped throughout the globe (Dyer, 1997; Agardy and Alder, 2005). There is an increasing recognition of the economic value of the natural capital in the marine coastal zone (Barbier et al., 2008). High levels of nutrients present in the water column and the sediments, provided by the inflows of both fresh water and sea water, make estuarine environments one of the most productive natural habitats in the world (McLusky and Elliott, 2004). As a result, these coastal systems support a diverse range of flora and fauna. Additionally, estuaries and tidal basins in particular provide a number of other economic and social functions, such as protecting adjacent land from flooding and erosion, through the dissipative properties of tidal flats, intertidal mangroves and salt marshes, and offering sheltered environments for port development, commercial shipping, and recreational boating activities.

Despite this functionality, estuarine systems worldwide are being stressed by terrestrial sediment input, and anthropological modifications of local morphology. Terrestrial sediments can have several adverse effects on navigability within ports and estuaries and tidal basins, and on the functioning of estuarine ecosystems. The latter effects include smothering of sea grass- and shellfish beds (Thrush et al., 2004; Rodil et al., 2011), hampering phytoplankton productivity by reducing water clarity (Morrison et al., 2009), altering the seabed biogeochemistry (Gilbert et al., 2003; Tang and Kristensen, 2007) and killing infauna (Woodin et al., 2012). Anthropological modifications in estuarine systems include channel dredging to facilitate navigation, land reclamation for port development, and the construction of sea walls for coastal protection. These modifications can directly disrupt coastal ecosystems and marine life, and fundamentally alter estuarine tidal prisms,

influence patterns of tidal currents (Colby et al., 2010), and alter sediment and nutrient transport (e.g. Tay et al., 2012).

Estuarine systems transport and trap terrestrially derived sediments through the combined action of various forcings such as tides, wind, waves, and freshwater flow (Hansen and Rattray, 1966). These forcings can influence the topography of these systems on different temporal and spatial scales (Hibma et al., 2004). The amount of sediment within an estuarine system controls the distribution and extent of relatively shallow intertidal flat regions (e.g. Dalrymple et al., 1992). Estuarine and tidal basin morphology is modulated by tidal processes, meteorological forcing, and sediment transport processes in a non-linear fashion, whereby sediment deposition and erosion modify the morphology, which in turn affects hydrodynamic processes and sediment distribution. In order to counter adverse effects in estuarine systems, for example through development of management strategies, a deeper understanding of the physical processes controlling the movement and deposition of sediments is of key importance.

1.2   Sediment transport and morphological evolution of estuaries

Two distinct estuary types can be recognized on the basis of dominant hydrodynamic processes: tide- and wave-dominated systems. In theory, all estuarine systems are characterised by a three-fold structure: an outer, marine-dominated section; a lower-energy central zone; and an inner, more river-dominated region. The relative importance of these three regions within a specific estuarine system depends on factors such as tidal range, sediment availability, and the stage of estuary evolution. Estuarine systems can experience progradation or transgression, and these processes are modulated by changes in sea-level and sediment supply (e.g. Boyd et al., 1992; Dalrymple et al., 1992).

In estuaries and tidal basins in which propagation of swell from the open coast is limited, or where the geometry of the estuary limits the fetch over which swell within the estuary can develop, sediment transport and morphological changes are highly dependent on tidal processes (Friedrichs, 2011; Hunt et al., 2015). Tidal asymmetry within such tide-dominated systems affects sediment deposition patterns as a result of non-linear feedbacks between tides and morphology, with the modified morphology controlling whether the seaward (ebb) tidal currents dominate over the landward (flood) tidal currents (Friedrichs and Aubrey, 1988; Wang et al., 2002). Estuaries and tidal basins can be classed in terms of tidal asymmetry as either a net importer of sediment (flood dominant) or a net exporter of sediment (ebb dominant). Net sediment transport over a tidal cycle

can occur because of Eulerian- or Lagrangian effects (Ridderinkhof, 1997; Friedrichs, 2011). Eulerian asymmetry refers to the distortion of the tidal wave from a sinusoidal shape. This distortion creates an asymmetry between the magnitude of flood and ebb velocities, owing to relative differences in duration or speed of the ebb and flood stages of the tidal cycle (Friedrichs and Aubrey, 1988; Friedrichs, 2010). Coarser sediments are mainly affected, with transport being initiated once a critical threshold velocity is exceeded (Dronkers, 1986; Le Hir et al., 2000). A small velocity asymmetry can result in a large increase in potential for net sediment transport over a tidal cycle. Fine suspended sediments (muds, silts and clays) have slower settling velocities than coarse sediments (Whitehouse et al., 2000), and are consequently more affected by Lagrangian effects such as the duration of slack water. During slack water, if fine suspended sediments are present in the water column, these particles are deposited when tidal velocities fall below a critical threshold velocity (Le Hir et al., 2000).

The shape of estuarine intertidal flat regions depends on several factors, including tidal processes, local morphology and geology, and meteorological forcing. Intertidal profiles that experience sediment accretion may evolve towards a convex and relatively shallow equilibrium profile, which can be described by a convex-shaped hypsometric curve. Shallow tidal flats can host coastal vegetation such as sea grasses, salt marsh and mangroves, which provide vital habitats for bird and marine life (Dayton, 2003). Salt marsh and mangroves can influence intertidal hydrodynamics through processes such as flow routing and stabilisation of tidal channel networks, and by affecting patterns or erosion and deposition (e.g. van Maanen et al., 2015, Mullarney and Henderson, 2018). Extensive shallow and vegetated intertidal regions are advantageous for coastal protection, by decreasing the risk of flooding of the hinterland, and by forming a buffer for shorelines against damage during extreme events (e.g. Temmerman et al., 2013; Bouma et al., 2014; Montgomery et al., 2019). Large waves can also be effectively dissipated by salt marshes (Hu et al., 2015), while mangroves may provide resistance to damage from hurricanes (Krauss et al., 2009) or tsunamis (Danielsen et al., 2005). Increasingly erosional estuarine environments can result in an intertidal profile which is deeper relative to mean sea level and can be described by a more concave-shaped hypsometric curve (Friedrichs and Aubrey, 1996; Roberts et al., 2000; Mariotti and Fagherazzi, 2013). Such less-infilled conditions may be preferred in coastal regions where navigability is of prime importance.

Meteorological forcing can play an important role in modulating hydrodynamic and sediment transport processes in estuaries (Bolle et al., 2010). Wind-driven currents

generated by strong wind events may influence tide-driven hydrodynamics, sedimentary processes and associated morphological changes in shallow estuarine regions (e.g. Sanay & Valle-Levinson, 2005; Hunt et al., 2015; Juarez et al, 2019). Additionally, in regions in which open ocean swell is able to propagate into a coastal system, or where fetch is sufficiently large to allow for the generation of local wind swell, waves can play an important role in the physical and biological functioning of estuarine systems (e.g. Christiansen et al, 2006; Hunt et al., 2016). Shear stresses resulting from moderate to stormy wind events have been shown to be capable of modulating flow directions and sediment transport in shallow coastal systems (e.g. Green and Coco, 2014; de Vet et al, 2017).

Sediment transfer in estuarine systems occurs on varying spatial and temporal scales. Sediment connectivity can be used as a framework for understanding processes controlling sediment movement in these shallow coastal environments. Connectivity aids the explanation of connected sediment transfer between different regions of an estuary, such as sediment movement from sources to sinks, creating an understanding of pathways, routes and scales of movement of sediment (Pearson et al., 2020). Numerical models can provide a convenient way of exploring sediment connectivity in estuarine systems (Wohl et al., 2019).

Results from existing numerical modelling studies that examine the physical processes affecting sediment transport and morphological changes in shallow estuarine systems and tidal basins often do not consider the effects of detailed, site-specific geometric and hypsometric characteristics, geological settings, and meteorological conditions, which can substantially modulate hydrodynamics and sediment transport pathways in shallow estuaries.

1.3   Estuaries under climate change

Estuaries and tidal basins globally are becoming more vulnerable to climate change and sea level rise. The potential impacts of changes in sea level on an estuarine system depend on a range of factors, such as sediment supply, local tidal characteristics, and geological constraints (i.e. Robins et al., 2010; Fagherazzi et al., 2012; Hanslow et al., 2018). A change in water depths will influence tidal dynamics within an estuary and can potentially result in morphological and habitat changes. In general, an increase in water depth will result in a greater flood dominance which will be accompanied by the transportation of sediment further into an estuary. Three simplified models of estuarine system response to

sea level rise can be described (Townend and Pethick, 2002). Firstly, when sediment supply is limited relative to the rate of sea level rise, morphological processes will be unable to keep up with the rise in sea level. The combination of these processes results in increased transgression of the system, which may lead to drowning of the estuary. Consequently, intertidal areas may be flooded and eroded (Dalrymple et al, 1992; Kirwan and Temmerman, 2009). The presence of a fixed landward boundary (e.g. dikes) may prevent intertidal areas and associated habitats to migrate upward, resulting in what is often referred to as 'coastal squeeze' (Wolters et al., 2005). Secondly, in cases in which sediment from external sources is somewhat more abundant, and internal redistribution of sediment also occurs, the term 'rollover' is used (Townend and Pethick, 2002). As sea level rises, the flood dominant estuary adjusts to maintain its form, bringing more sediment into the upper estuary, and in doing so moves landward. Lastly, when the external sediment supply is greater than the rate of sea level rise, the estuary becomes flood dominant, resulting in accretion which can keep pace with sea level rise (e.g. Kirwan et al., 2010). If very large amounts of sediment are imported, this progradation of the system may lead to the conversion of the estuarine system into a tidal delta (e.g. Dalrymple et al., 1992). The above descriptions are considerably simplified versions of the full system response to sea level rise, which also incorporates numerous feedback loops and the interaction of multiple spatial and temporal scales (Townend, 2004). However, this analysis does nonetheless highlight some of the interrelated processes shaping estuarine morphology that should be considered when studying sediment transport processes and connectivity patterns in coastal systems.

Changes in precipitation rates in estuarine regions as a result of climate change will influence the volume of freshwater entering an estuarine system. In regions where extreme rainfall events, or wet storms, are predicted to intensify, the associated sediment fluxes into the system are expected to increase significantly (e.g. Elliott et al., 2010). Dry storms have been shown to rework sediments deposited by wet storms (Bever et al., 2011). Local winds that accompany both wet and dry storm events can influence estuarine and tidal basin circulation by inducing wind-generated currents as well as increased wave energy (e.g. Bever and Harris, 2014). Hence, any change in wind speed or direction may have an impact on sediment deposition and erosion patterns, and consequently impact morphological and biological changes inside these shallow coastal systems. The level of impact may be highly site specific and sensitive to predicted changes in wind climate,

available fetch, as well as morphological and geometrical characteristics of a relevant estuary or tidal basin.

In summary, estuaries and tidal basins are highly dynamic environments that provide valuable ecosystem services and economic functions. To efficiently manage these shallow coastal systems into the future, an improved understanding of physical and morphological processes is critical. The objective of this research is to explore the links between tidal processes, hypsometric and geometric basin characteristics, sediment connectivity, and meteorological forcing in shallow estuarine systems, by addressing three main research questions which are outlined in the following section.

1.4   Approach and research questions

The processes affecting sediment transport rates and associated changes in the morphological equilibrium profiles within estuaries and tidal basins have been examined in a wide range of hydrodynamic modelling studies. The results of these studies are often considered to be accurate for a diverse range of estuarine systems. However, the specific geomorphologic properties of these systems, such as entrance constrictedness, basin width, and intertidal profile shape, can substantially modulate local hydrodynamics and patterns of tidal asymmetry. Such variations in tidal process can in turn affect sediment transport pathways, and morphological feedbacks. These fundamental links and stability relationships that exist between specific geomorphologic characteristics of shallow estuarine systems and the physical processes inside these systems have not yet been quantified (e.g. Townend, 2012; Zhou et al., 2017).

The present work aims to improve our understanding of the geometric and hypsometric effects on hydrodynamics, tidal asymmetry, and sediment connectivity in shallow estuarine systems. The role of meteorological forcing in modulating these relationships is also examined. These topics have been explored in this thesis through the following research questions:

1. How do basin geometry and hypsometry affect hydrodynamics and tidal asymmetry in shallow tidally dominated basins?
2. How do wind-generated currents modulate velocity asymmetry in shallow tidal basins with varying geometries?
3. What are the relationships between geometry, hypsometry, and sediment connectivity in shallow estuarine systems?

These questions have been answered using a combination of field work, idealised numerical modelling, and numerical modelling of a real-world estuarine system, producing scientifically robust research results.

1.5   Case study site

Tauranga Harbour is situated within the Bay of Plenty region, on the east coast of the North Island of New Zealand (Figure 1.1). The harbour, which is managed by the Bay of Plenty Regional Council (BoPRC), is a large barrier-enclosed estuarine lagoon (over 200 km^2) with extensive sandy tidal flats, exposed at low tide (Healy et al., 1996). It is an area of great cultural significance for New Zealand's Maori community (Sinner et al., 2011) and provides opportunities for activities such as shellfish collecting, boating and swimming. Commercial development is mainly centred within the southern basin, which features the country's largest export port, the Port of Tauranga (PoT). The Matakana barrier island protects the harbour from the Pacific Ocean. Intertidal flats make up approximately 66% of the estuary, with large flats dividing the lagoon into the northern (Katikati) and the southern (Taraunga) basin. Both interconnected basins have a connection to the open coast constricted by a Holocene barrier tombolo (Healy and Kirk, 1982); near Bowentown in the north, and near Mount Maunganui in the south. The harbour has an average water depth of 3 m at low tide (Tay et al., 2012) and features a semi-diurnal tide with tidal ranges of 1.62 m at spring tide and 1.24 m at neap tide (Heath, 1985). The estuary is characterised by several small sub-basins that drain local catchments on the landward of both the northern and southern basin.

Tauranga Harbour is facing increasing population pressure (Nichol et al., 2000; Morrison et al., 2009), and is experiencing a decline in shellfish populations and seagrass beds, increased infilling, mangrove expansion (e.g. Stokes et al., 2010), and Ulva blooms (BoPRC, 2011). These issues are driven partially by natural climatic variations and partially by anthropogenic influences.

Figure 1.1: Overview of Tauranga Harbour; location in New Zealand shown in bottom left overview map in red. Te Puna, Apata, and Welcome Bay sub-basins indicated by red crosses.

Sediments within Tauranga Harbour are predominantly sandy, with average mud content of 10 – 30%, similar to other New Zealand estuaries (Ellis et al., 2013). Work by the National Institute of Water and Atmospheric Research (NIWA) identified increased sediment input, leading to infilling and turbid waters, as a key stressor to the Tauranga Harbour estuary (Hume et al., 2010). This increase, partially a result of land use changes, is expected to continue in the near future. The research by NIWA focused on the southern part of the harbour. The results also showed that present-day sedimentation rates within the southern harbour are elevated where sediments are trapped along the fringes of larger embayments (e.g. Welcome Bay), and where causeways obstruct flushing (e.g. Te Puna inner, see Figure 1.1). The Te Puna sub-basin was identified as the most depositional, together with the Apata sub-basin (Ellis et al., 2013), as shown in Figure 1.1. The Wairoa River sub catchment was found to be the main sediment contributor to the southern harbour, discharging 45.6% of the total sediment load (Elliott et al., 2010).

A quantification of hydrodynamic forcings and morphological responses within Tauranga Harbour at different spatial scales, would allow the BoPRC to create more detailed

predictions of sand and mud movement and consequently aid the development of targeted mitigation strategies. Most of the previous work in the harbour has focused on the southern basin (e.g. Ellis et al., 2013; Tay et al., 2013; MacPherson et al., 2017). The scope of this thesis includes the northern basin, in order to provide a calibrated numerical model of the full harbour.

1.6   Data collection

Field data were collected during a large-scale field campaign carried out in October and November of 2015. Co-located current meters and pressure sensors were deployed in both the northern and southern basins of Tauranga Harbour. Instrument locations were chosen in such a way that a dataset of estuarine hydrodynamics was collected for both relatively deep areas, such as the main tidal channels, as well as shallower areas such as sub-basin channels and tidal flat regions. The main aim of the field deployment was to collect data in the northern and central part of the estuary, as knowledge of hydrodynamic processes in the northern basin were especially limited. Currents and water levels were measured in the channel of the northern mouth of the harbour, and in, or near, the main tidal channels further upstream (southwards) in the northern basin. Additionally, the channel crossing the tidal flats that separate the northern and southern basin was also equipped with a current meter and pressure sensor. To encompass the variety of sub-basins present in Tauranga Harbour, additional current meters and pressure sensors were placed in the channels of five sub-basins in both the northern and southern parts of the estuary. Current velocity and turbidity data from the vicinity southern harbour mouth were also supplemented by permanent monitoring stations managed by the BoPRC and the PoT. All instruments were deployed on the same day, to ensure that all measurements encompass the same time period. Regular checks were carried out to ensure properly functioning instruments, and to remove any objects that may interfere with the measurements, such as algae. Further details regarding the field campaign and obtained data are provided in Chapter 2.
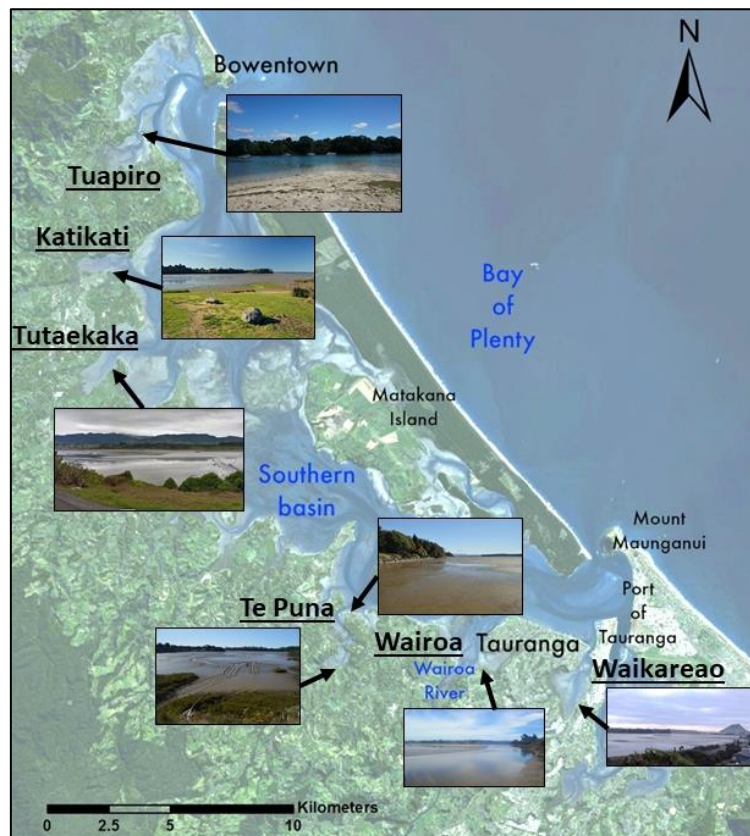
Figure 1.2: Overview of Tauranga Harbour, highlighting the six sub-basins (names underlined) that are the focus of this research.

The data obtained during the field campaign was used to calibrate and validate a numerical model of the whole estuary, which was developed using the Delft3D modelling software. Results from the numerical model are used in this thesis to answer the research questions, with a focus on the physical processes within -, and the connections between, the main estuary and six of the sub-basins in Tauranga Harbour (underlined in Figure 1.2). A detailed description of the numerical model and the six sub-basins is provided in Chapters 1 and 3.

1.7   Thesis outline

The main body of this thesis comprised three chapters which describe research investigating the links between hydrodynamics, morphology, geometry, sediment connectivity, and meteorological forcing in shallow estuaries and tidal basins. Each of the three chapters was intended as a stand-alone document for submission to an international, peer-reviewed journal.

- Chapter 2 focuses on the interactions between hydrodynamic processes, morphology, and geometry in microtidal basins, based on a numerical model of Tauranga Harbour. The depth-averaged model was developed in Delft3D, and validated based on field data collected in the estuary during an extensive field

campaign in 2015. This study was the first to link patterns of tidal velocity asymmetry, slack water asymmetry, and bed shear stress with geomorphological and geometric characteristics of shallow tidal basins. A version of this work was published in *Earth Surface Process and Landforms* in March 2019, with myself as a first author. Additionally, some of the findings from this study were published in a paper (again with myself as first author) for the *New Zealand Coastal Society Conference* in November 2017.

- Chapter 3 explores how meteorological forcing affects velocity asymmetry and sediment transport potential in the shallow tidal basins. Idealised numerical modelling was applied in Delft3D, based on realistic morphologies created to represent basins with varying planform shape and bathymetry. The study results highlight the complex relationship between tidal basin geometry, local hydrodynamics, and wind-induced currents, and emphasize the importance of using well-defined tidal and meteorological conditions in numerical modelling. A version of this work has been published in *Earth Surface Processes and Landforms* in September 2021, with myself as a first author.

- In Chapter 4, sediment transport pathways between different geomorphic regions in the Tauranga Harbour estuary are analysed. The sediment connectivity framework is applied to model results of sediment transport for different grainsizes, based on the estuary-scale numerical model. Additionally, detailed transport patterns inside the tidal sub-basins were resolved, and correlated with geomorphological and hydrodynamic characteristics of the shallow basins. This work will be submitted to *Geomorphology*.

In Chapter 5, the main findings of this thesis are summarised, along with suggestions of directions for future research.

Chapter 2

The Links Between Entrance Geometry, Hypsometry and Hydrodynamics in Shallow Tidally Dominated Basins

Intertidal flats in the northern basin of Tauranga Harbour

Contribution of Authors

Chapter 2 presents the article entitled "The links between entrance geometry, hypsometry and hydrodynamics in shallow tidally dominated basins", a version of which was published in *Earth Surface Processes and Landforms* in 2019. Data were collected for this study during a field campaign (Section 2.2.2) in Tauranga Harbour, New Zealand, by myself, Julia C. Mullarney, and Dean Sandwell primarily. I wrote MATLAB scripts to load, quality control, and analyse all the hydrodynamic data. I also developed a numerical model for Tauranga Harbour using Delft3D, with supervision from Christian Winter, Julia C. Mullarney, and Karin R. Bryan. I wrote MATLAB scripts to process and analyse the model data. I prepared all the figures for the article and wrote the initial and subsequent drafts of the manuscript. My co-authors, Julia C. Mullarney, Karin R. Bryan, and Christian Winter edited my drafts and provided valuable comments, direction, and editorial help responding to reviewers' comments.

2.1 Introduction

The geometry of tidal basin entrances modulates the hydrodynamics within basins. The presence of a constricted entrance, resulting from geological features such as a barrier beach, affects the shape of the tidal wave and associated hydrodynamics through the entrance channel (Zarzuelo et al., 2016) and within the basin itself (De Ruiter et al., 2017) in a process known as tidal choking (Kjerfve, 1986). The astronomical tide may become strongly distorted during its propagation into a basin, resulting in the development of time asymmetries in the rise and fall of the surface tide and associated time and amplitude asymmetries in the velocity field (Boon and Byrne, 1981). Inside enclosed hyposynchronous basins, friction exceeds the effects of tidal convergence, diminishing the tidal range and reducing tidal energy. Conversely, in hypersynchronous funnel shaped basins, effects of convergence exceed those of friction, resulting in a more energetic environment (Nichols and Biggs, 1985). This modification of local hydrodynamics as a result of entrance configuration influences sediment transport patterns and intertidal morphology within tidal basins. In order to develop robust stability relationships between basin geometry, hydrodynamic processes and related sediment transport potential, further research is necessary (e.g. Zhou et al., 2018). The links between basin entrance geometry, intertidal profile shapes and associated hydrodynamic processes are examined in the present study.

We apply hydrodynamic models of shallow microtidal basins with varying entrance constriction to study the geomorphic significance of entrance regimes. Processes driving potential geomorphic changes are studied by resolving the effects of entrance geometry on flood and ebb dominance and spatial gradients in bed shear stress within the sub-basins. We consider sediment deposition and erosion potential related to asymmetries in both peak tidal velocities and slack tide duration, and explore the link with equilibrium intertidal profile shapes. In this study we neglect effects of wind-generated currents and waves in order to isolate the effects on tidal processes. Our results are discussed for spring and neap tidal cycles, within both subtidal and intertidal sub-basin regions.

Tidal asymmetry influences rates of intertidal sediment import and export, in which flood-dominant regimes enhance sediment accumulation in a basin while ebb dominance promotes sediment removal (e.g. Pritchard et al., 2002; Bever and MacWilliams, 2013). Tidal distortion and asymmetry can be analysed by comparing dominant semi-diurnal tidal constituents (M_2) and quarter-diurnal overtides (M_4) (Friedrichs and Aubrey, 1988).

Such analyses suggest whether a system is mainly ebb- or flood-dominant, thus providing an indication of the morphodynamic status of the system. Detailed analysis of asymmetries in ebb- and flood-peak tidal velocities and slack tide durations can provide an indication of potential transport directions for larger and smaller sediment grainsizes, respectively. Within microtidal estuaries and basins, tidal forces are relatively strong as well as asymmetrical, and are capable of transporting and depositing substantial amounts of sediment (Green et al., 1997), especially during spring tidal conditions (Fagherazzi et al., 2007). Consequently, tidal asymmetry may result in sediment trapping in coastal areas and tidal basins (Castaing and Allen, 1981).

Intertidal bathymetry can be presented in terms of hypsometry, representing the total wetted surface area of a basin as a function of elevation (Friedrichs and Aubrey, 1996; Townend, 2008). Hypsometry can be considered for whole basins or for smaller sections of intertidal regions (e.g. Kirby, 2000; Wang et al., 2002; De Vet et al., 2017). Previous studies have shown that equilibrium hypsometric profiles with a convex shape, characterized by relatively elevated tidal flats, are generally found in tidally dominated, flood-dominant accretionary environments with sufficient external sediment supply (e.g. Roberts et al., 2000; Bearman et al., 2010; Friedrichs, 2011). Intertidal hypsometric profile shape can also be modulated by basin geometry. The presence of a constricted basin entrance, for example, may promote sedimentation and increase profile convexity by reducing tidal energy in the basin centre. Leuven et al. (2018) concluded that within larger-scale estuarine systems, tidal flats will be more developed when a constricted entrance is present. Conversely, wave-dominated environments are generally associated with intertidal erosion, resulting in progressively more concave hypsometric profiles with lower intertidal regions (Friedrichs and Aubrey, 1996; Zhou et al., 2015). These concave, high energy intertidal environments experience little seaward migration and may exhibit profile retreat.

The processes affecting infilling rates and associated changes in the morphological equilibrium profiles within estuarine systems and tidal basins have been addressed in a wide range of studies by means of numerical modelling. Idealized numerical models have been applied to whole estuaries (e.g. Townend, 2010; Hunt et al., 2015) and tidal embayments (e.g. Van Maanen et al., 2013) as well as to intertidal regions (e.g. Roberts et al., 2000; Mariotti and Fagherazzi, 2013) and tidal channels (e.g. Lanzoni and Seminara, 2002). Furthermore, a large number of previous studies have incorporated more complex hydrodynamic and morphological models of estuarine regions (e.g. Wang et al., 2002;

Bearman et al., 2010; Herrling and Winter, 2014; De Vet et al., 2017) that are based on available bathymetrical data and are calibrated to obtain a match between field observations and simulated variables. Corresponding modelling study results are often assumed to be valid for a divergent range of basin types, thereby disregarding the fact that these studies are invariably carried out in a very specific geomorphic setting. Funnel-shaped basins, such as well studied systems in the United Kingdom (e.g. Townend, 2005 Rees, 2006) and the Netherlands (e.g. Van Maren et al., 2015), are characterized by a large width-to-depth ratio. These drowned river valleys broaden and deepen seaward and have no barrier features or delta complexes at their entrances (Hume and Herdendorf, 1988). Contrastingly, enclosed estuaries and tidal basins (e.g. Van Maanen et al., 2013; Tay et al., 2013) are often much shallower and are separated from the open ocean by rocky headlands, sand spits or barrier islands. Recent work has highlighted the importance of defining landscape settings when studying estuarine systems and tidal basins (e.g. Zhou et al., 2017; Townend, 2012).

A fundamental link not explored by previous modelling studies of tidal basins is the relationship between entrance geometry, basin hypsometry and tidal asymmetry. Here, we use numerical modelling to investigate the impact of basin geometry on local hydrodynamic processes in six microtidal sub-basins of Tauranga Harbour, Bay of Plenty, New Zealand. We introduce a simple parameter to define levels of basin dilation and explore relationships between tidal velocity asymmetry, slack duration asymmetry, bed shear stresses and intertidal hypsometric profile shapes. Our results indicate that tidal energy variations within two divergent basin geometries have a substantial impact on spatial shear stress patterns and intertidal hypsometry.

2.2 Study Area and Numerical Model

2.2.1 Tauranga Harbour

Tauranga Harbour is a microtidal estuarine lagoon covering over 200 km^2, located on the east coast of the North Island of New Zealand (Figure 2.1a). Throughout the early Holocene, the harbour area represented an unprotected coastline with sediment sourced from offshore via longshore transport. This process led to the development of barrier islands, which restricted marine sediment input and led to the present-day sedimentary and hydrodynamic regime (MacPherson et al., 2017). The relatively shallow and well-mixed estuary (Tay et al., 2012) is now confined by a 24-km-long barrier island (Matakana Island, Figure 2.1b). Consequently, Tauranga Harbour can be classified as a

barrier-enclosed lagoon (category F) according to Hume et al. (2007). Intertidal flats make up approximately 65% of the estuary (Healy et al., 1996) and are exposed at low tide (mean level of the sea, MLOS -0.76 m), when the average water depth in the estuary is about 3 m (Tay et al., 2012). An area of tidal flats divides the estuary into a northern and a southern basin. Commercial development is mainly restricted to the southern basin (De Lange and Healy, 1990), which is the location of New Zealand's largest export port (the Port of Tauranga, PoT) (Foster, 1992). Tauranga Harbour is characterized by a semi-diurnal tide that ranges from 1.62 m at spring tide to 1.24 m at neap tide (Heath, 1985). The two harbour entrances are both constricted by a Holocene barrier tombolo, Bowentown in the north and Mount Maunganui in the south (Healy and Kirk, 1982).
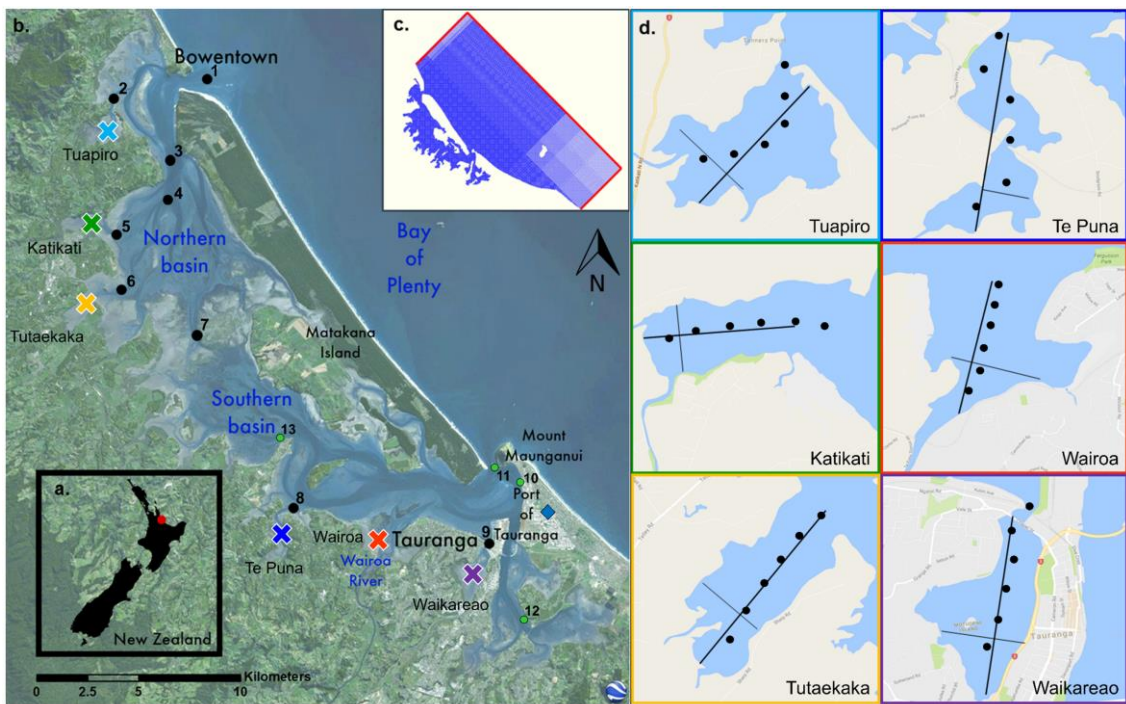
Figure 2.1: Tauranga Harbour overview, with location in New Zealand indicated by red dot (a). (b) Coloured crosses depict locations of six sub-basins with measurement locations (green and black dots) and Tauranga Airport meteorological station (blue diamond). Details of basins shown in (d) with corresponding box colours. Delft3D model grid shown in (c), including model boundaries in red.

The south-western side of the estuary is characterized by a number of sub-basins with relatively small tidal prisms that vary in shape, size and rate of entrance constriction (Figures 2.1b and 2.1d). The shallow microtidal basins are sheltered from the open ocean and are generally characterized by little freshwater input. Six of these tidal basins are the focus of our study. Tuapiro, located westward of the northern harbour mouth (Figure 2.1b, light blue), is a divergent sub-basin covering 2.5 km^2 featuring a constricted entrance. Katikati (Figure 2.1b, green) and Tutaekaka (Figure 2.1b, yellow), located closer to the

estuary centre, cover an area of 2.0 and 2.2 km^2, respectively, and both have unconstricted entrances. Te Puna, located in the southern basin of Tauranga Harbour, (Figure 2.1b, dark blue) is an elongated constricted basin covering about 1.5 km^2. Eastward of Te Puna, the approximately 3.8 km^2 slightly convergent Wairoa basin (Figure 2.1b, red) features an unconstricted entrance. Finally, the divergent Waikareao sub-basin (Figure 2.1b, purple), covers about 2.7 km^2 and has a constricted entrance. An overview of the morphologic and hydrologic characteristics of the six sub-basins can be found in Table 2.1.

The basins show differences in morphology that can be related to sediment depositional environments. Three of the basins, Tuapiro, Te Puna and Waikareao, experience relatively high sedimentation rates due to large sediment input, which promotes infilling and raises turbidity levels. Consequently, these basins are rather shallow, resulting in relatively small tidal prisms (Table 2.1). The other three basins, Katikati, Tutaekaka and Wairoa, are characterized by lower rates of sedimentation and larger tidal prisms. In general, sediments in Tauranga Harbour are predominantly sandy with an average mud percentage of 10 to 30%, comparable to sediment characteristics of other New Zealand estuaries. Te Puna basin (Figures 2.1b, and 2.1d, dark blue) was identified as one of the most depositional (> 6 mm/yr) sub-basins, based on a long-term modelling study that focused on the southern part of the estuary (Ellis et al., 2013). The same study predicted moderate depositional rates for Waikareao (Figures 2.1b and 2.1d, purple) (1 mm/yr) and virtually no deposition in the Wairoa sub-basin (Figures 2.1b and 2.1d, red). For the northern part of Tauranga Harbour, no such studies have been carried out. Scarce data are available from sediment plates supplied by the Bay of Plenty Regional Council (BoPRC) that measure sediment accumulation at a specific location, hinting at a depositional environment within the Tuapiro basin (Figures 2.1b and 2.1d, light blue). Sediment plates within the Tutaekaka sub-basin (Figures 2.1b and 2.1d, yellow) display very moderate deposition, whereas Katikati (Figures 2.1b and 2.1d, green) appears to undergo erosion. As the sediment plates have been deployed recently and the data spans no more than a few years, with only a few data points for each plate, long-term depositional trends are not available and reliable short-term trends cannot be deduced. Hence, strong conclusions regarding depositional rates within the sub-basins cannot be drawn from this data.

Table 2.1: Morphologic and hydrologic characteristics of the six sub-basins considered in our study

Sub-basin	Area at High Tide (km²)	Volume Below MHWS (x10⁶ m³)	Tidal Prism[a] (x10⁶ m³)	Entrance[b]			
				Constriction	Width (m)	Mean Depth (m)	Area (m²)
Tuapiro	2.5	7.1	1.5	Yes	160	1.7	270
Katikati	2.0	8.9	1.9	No	680	0.6	375
Tutaekaka	2.2	8.5	1.8	No	660	0.5	330
Te Puna	1.5	5.6	1.0	Yes	150	1.5	225
Wairoa	3.8	10.3	2.4	No	1080	0.4	430
Waikareao	2.7	7.9	1.3	Yes	130	2.1	265

[a] Tidal prism: volume between MHW and MLW
[b] Entrance characteristics for mean tidal conditions
Note: MHWS, mean high water springs.

2.2.2 Field Data

A month-long large-scale field deployment was undertaken from 21 October to 19 November 2015, in order to provide calibration data for the hydrodynamic model developed in this study (see next section). Since previous studies of the estuary and current estuary monitoring focus primarily on the southern basin, knowledge of hydrodynamic and sedimentary processes in the northern basin is limited. Consequently, the emphasis of the field deployment was on collecting data in the northern and central part of the estuary. Water levels and tidal current velocity data were obtained using co-located pressure and current meters (Figure 2.1b, black dots). Instrument settings are given in Table 2.2. Instrument locations were chosen in such a way that a dataset of hydrodynamics would be obtained for both relatively deep areas of the estuary, such as the main estuarine tidal channels, and shallower areas corresponding to sub-basin channels and tidal flat regions.

Measurements obtained during the field campaign were supplemented by data from four monitoring stations located in the southern basin (Figure 2.1b, green dots). Acoustic Doppler current profiler (ADCP) current velocity data for the southern harbour mouth and the tug berth tidal station were provided by the PoT, whereas water levels for Oruamatua and Omokoroa were supplied by the BoPRC. The quality of the data obtained during the 2015 field campaign was somewhat variable. Ulva blooms in Tauranga Harbour resulted in some of the instruments being covered by algae for at least part of their month-long deployment: this corrupted data has been discarded.

Table 2.2: Summary of instrumentation deployed during 2015 field campaign (locations are shown in Figure 2.1)

Location	Instrument	Make	Model	Cell size (m per m)	Sampling Interval (s)	Sampling Rate (Hz)	Sampling Duration (s)	Averaging duration (s)
1	ADCP	RDI	Sentinel	0.4 (8)	300	2	60	60
2	Current meter	Inter Ocean	S4A	-	120	2	60	5
3	Current meter	Inter Ocean	S4A	-	120	2	60	5
4	ADCP	Nortek	Aquadopp	0.2 (6)	300	2	60	60
5	ADP	Sontek	Argonaut-XR	0.5 (5)	300	1	120	120
6	Current meter	Inter Ocean	S4A	-	120	2	60	5
7	ADCP	Nortek	Aquadopp	0.2 (4)	300	2	60	60
8	ADV	Nortek	Vector	-	900	8	120	120
9	Current meter	Inter Ocean	S4A	-	120	2	60	5

Wind characteristics for Tauranga Harbour were determined based on climatic data obtained from Tauranga Airport meteorological station (Figure 2.1b). Figure 2.2a shows hourly wind speed, direction and frequency of occurrence during the field campaign in October and November of 2015. Westerly winds are clearly dominant, accompanied by infrequent northerly wind events. Mean wind speeds during the field campaign were 6 m/s, with occasional maximum wind speeds of about 12 m/s. These wind directions and speeds are generally consistent with the long-term wind characteristics within Tauranga Harbour (Figure 2.2b).
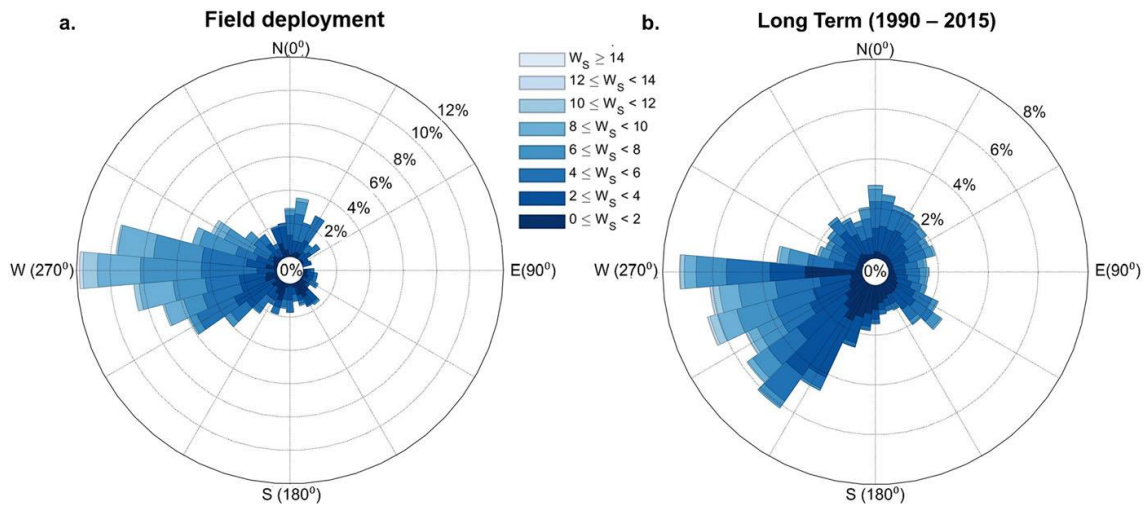
Figure 2.2: Wind characteristics for Tauranga Harbour (source: Tauranga Airport climate station) during field deployment (a) October/November 2015 and (b) during past 25 years. Wind speed, direction (from) and frequency of occurrence denoted by the shade, orientation and length of the bars, respectively. [Note difference in scale of maximum frequency of occurrence between (a) and (b).]

2.2.3 Numerical Model

The hydrodynamics within Tauranga Harbour were simulated by a two-dimensional, depth-integrated model using the Delft3D-FLOW hydrodynamic modelling system (Lesser et al., 2004). The model was divided into two sub-domains: an inner domain, covering the main estuary and the sub-basins with a grid resolution of 25 m by 25 m, and an outer offshore domain of roughly 20 km by 50 km with a gradually coarsening grid resolution in the offshore direction (Figure 2.1c).

Model bathymetry was generated by the interpolation of high-resolution light detection and ranging (LiDAR) (collected by the BoPRC and the PoT in 2014), which was first converted to MLOS datum, complemented by multibeam survey measurements and Land

Information New Zealand (LINZ) bathymetric data. For a few regions in the intertidal areas and sub-basins, data coverage was limited.

Tidal forcing at the open boundaries was based on 13 main tidal constituents, derived from the National Institute of Water and Atmospheric Research (NIWA) tidal model (NIWA, 2015) using the T_TIDE Matlab function (Pawlowicz et al., 2002). The resulting astronomic tidal amplitudes and phases were forced at the shore-parallel seaward boundary of the outer model domain (Figure 2.1c). Neumann boundaries, used to impose the alongshore water level gradient, were created for both shore-perpendicular seaward boundaries.

The model was run for a spring-neap tidal cycle between 25 October and 8 November 2015. The model time step was 0.1 minute. Freshwater input is generally small in comparison to tidal effects and was not included in the model. A spatially varying bottom roughness was used, with Manning coefficient values between 0.02 and 0.1 s/m$^{1/3}$ based on varying bathymetry elevations. Model calibration and validation indicated that water levels and current velocities are generally very well reproduced by the model throughout the estuary. Mean Brier Skill Score (BSS) values of 0.97 and 0.53 (both indicating an 'Excellent' performance rating according to Sutherland et al., 2004) were achieved for water levels and current speeds, respectively (see Appendix).

Following the calibration and validation runs, hydrodynamics within Tauranga Harbour were simulated in Delft3D over a tidal cycle for three different scenarios based on three representative tidal conditions: mean, spring, and neap tide. A hydrodynamic spin-up period of four days was discarded at the beginning of each scenario to exclude any initialization errors.

2.3 Results

2.3.1 Hypsometry

Intertidal hypsometric profiles for the six sub-basins depicted in Figures 2.1b and 2.1d were determined based on available bathymetric data. The resulting hypsometric curves (Figure 2.3) indicate the distribution of basin area above a given elevation for water depths between the average local entrance channel depth (~ 1–3m MLOS) and mean high water springs (MHWS) (0.86 + MLOS). Hypsometry curves were normalized by dividing each elevation (h) by the maximum elevation (H), and by dividing the area above each

elevation (*a*) by the total basin area (*A*) for each sub-basin. The hypsometric curve-fitting technique developed by Boon and Byrne (1981) was then applied:

$$\frac{a}{A} = \frac{G}{(r+G(1-r))} \tag{2.1}$$

with

$$G = \left(\frac{1-h}{H}\right)^{\gamma} \tag{2.2}$$

The parameter γ represents the area below the hypsometric curve (i.e. the volume of sediment in the basin) and provides an indication of profile convexity and basin maturity. The hypsometry exponent can also be linked to tidal distortion (Boon & Byrne, 1981), which aligns well with our study aims. Previous studies have shown that in-filled basins with convex-shaped hypsometric curves are characterized by γ-values around 2.0, whereas more concave-shaped basins with less developed intertidal regions are defined by γ-values ranging between 3.5 and 5 (Boon and Byrne, 1981; Van Maanen et al., 2013). A value of 0.02 was used for empirical parameter r, representing the curvature of the intertidal profile.
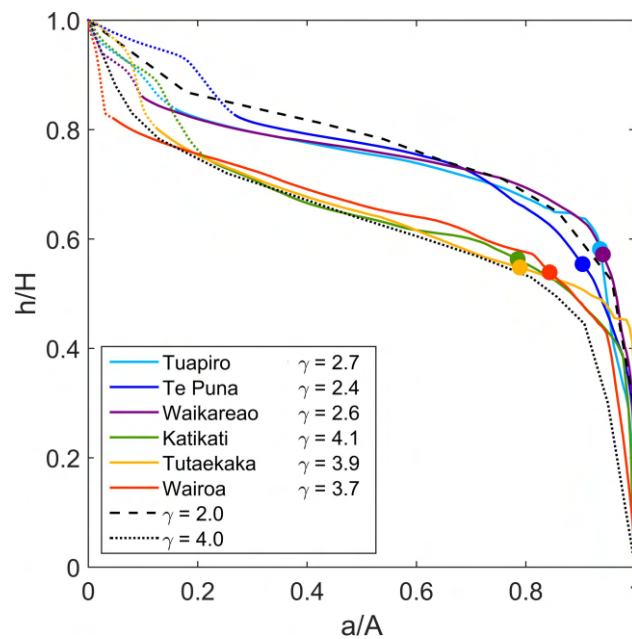
Figure 2.3: Hypsometric curves for six Tauranga Harbour sub-basins. Line colours match colours of basins in Figures 2.1b and 2.1d. X-Axis represents normalized area (*a/A*, where a is area and *A* is total basin area), y-axis shows normalized water depth [*h/H*, where *h* is water depth and *H* is maximum water depth (mean high water springs, MHWS)]. γ-values for each curve noted in legend. Coloured dots represent low water levels for basins. Black dashed and dotted lines show an infilled and less infilled idealized basin geometry, respectively (see Section 2.4). Note that coloured dotted lines represent data not corrected for intertidal vegetation presence.

Hypsometric profiles for the three constricted sub-basins, Tuapiro, Te Puna and Waikareao, were found to be characterized by relatively elevated intertidal flats and can be described as convex-shaped with γ-values ranging between 2.4 and 2.7 (Figure 2.3). Hypsometric curves for the unconstricted basins, Katikati, Tutaekaka and Wairoa, display a somewhat more concave shape with distinctly lower intertidal regions and γ-values around 4.0. The available bathymetric data were not corrected for the presence of intertidal vegetation (i.e. mangroves) in the upper reaches of the sub-basins, resulting in unnaturally sharp increases in some of the hypsometric curves (dotted lines in Figure 2.3).

2.3.2 Tidal Velocities and Bed Shear Stress

In order to highlight the effects of basin geometry on local hydrodynamics, modelled peak flood tidal velocities throughout two sub-basins were analysed for a representative mean tidal range of 1.4 m. Figures 2.4a and 2.4b show an example of flood current circulation patterns for a constricted (Tuapiro) and an unconstricted (Katikati) tidal basin, respectively. As anticipated, current speeds through a constricted entrance (arrows in Figure 2.4a) are typically large (~1.0 m/s). As the flow cross-section increases further into the basin, current velocities reduce by around 75%, with peak velocities around 0.25 m/s in the basin centre. Associated bed shear stresses (colours in Figure 2.4a) exhibit patterns comparable to the current velocity circulation. Unconstricted basin entrances (Figure 2.4b) are characterized by smaller depth-averaged velocities (~ 0.55 m/s) and shear stresses. Further landward velocities are still relatively large (~ 0.4 m/s), indicating limited velocity and shear stress reduction in unconstricted basin centres. Peak ebb-directed tidal currents (not shown) display patterns similar to flood currents, with fastest velocities and greatest shear stresses in the constricted entrance channel.

Bed shear stresses in the centre of both basins were averaged over representative transects (dashed lines in Figures 2.4a and 2.4b) that include subtidal (channel) and intertidal (flats) regions. In the resultant tidal stage diagrams (Figure 2.4c), magnitude and duration of shear stress (τ_{max}) during the flooding (positive τ_{max} values) and ebbing (negative τ_{max} values) tidal stages can be compared, highlighting tidal asymmetry characteristics. The tidal stage curves confirm the differences in shear stress values between the centre of a constricted (blue solid line, Figure 2.4c) and an unconstricted basin (red dashed line) as described earlier. Largest average shear stresses are shown for ebbing tides in the unconstricted basin (Katikati, dashed line). The constricted basin is characterized by smaller, flood-dominant shear stresses (Tuapiro, solid line).

24
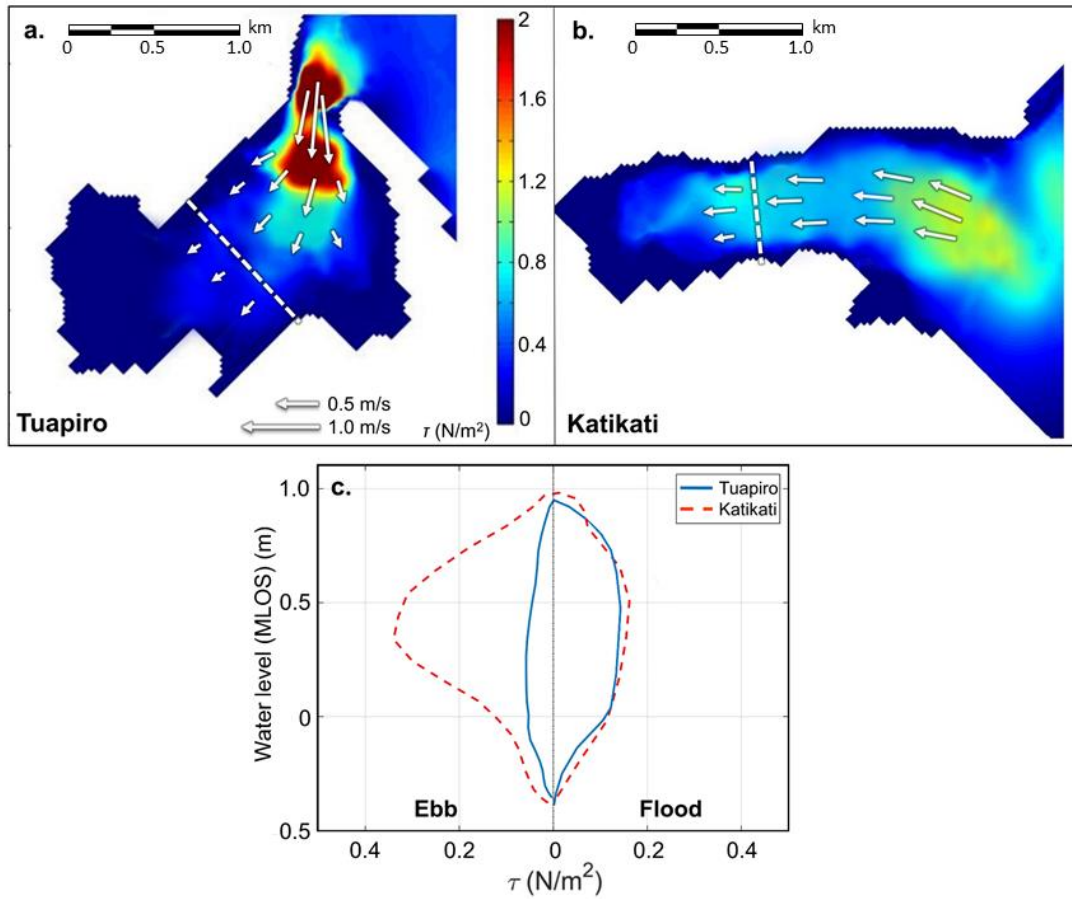
Figure 2.4: Model result examples for a constricted [Tuapiro (a)] and an unconstricted [Katikati (b)] sub-basin (locations in Figure 1b) showing depth-averaged peak flood-current velocity patterns [arrows in (a) and (b)] and associated maximum bed shear stress patterns [colours in (a) and (b)]. Tidal stage graphs (c) show shear stresses averaged over transects in basin centres [dashed lines in (a) and (b)].

Spatial bed shear stress patterns differ between subtidal and intertidal regions within a tidal basin. To further investigate these patterns, shear stress values were analysed for both subtidal (channels, Figures 2.5a and 2.5c) and intertidal (flats, Figures 2.5b and 2.5d) regions in six sections within each sub-basin (black dots in Figure 2.1d). Distances along each basin (from the entrance) were normalized by basin length. Results show maximum flood (Figures 2.5a and 2.5b) and ebb (Figures 2.5c and 2.5d) bed shear stresses. As expected, shear stresses in the relatively deep and constricted entrance channels (left side of Figures 2.5a and 2.5c, triangles) were found to be larger than shear stresses in unconstricted channels, matching the results shown in Figure 2.4. Further landward, shear stresses within subtidal regions (Figures 2.5a and 2.5c, towards the right) of constricted basins (triangles) reduce greatly, whereas shear stresses in unconstricted subtidal regions experience less reduction. In the basin centres (right side of Figures 2.5a and 2.5c), shear stresses within constricted channels are generally lower than in unconstricted basin channels, especially during ebbing tide (Figure 2.5c). Patterns for intertidal regions are

less clear near the basin entrances (left side of Figures 2.5b and 2.5d). Within the basin centres intertidal shear stress patterns for ebbing tides are comparable to the patterns found in subtidal regions, with larger shear stress values in unconstricted basins (right side of Figure 2.5d, circles). Flood-related shear stresses are slightly greater for constricted basins (right side of Figure 2.5c, triangles). In general, modelled shear stresses within unconstricted basins suggest weak ebb dominance, whereas constricted basins where found to be largely flood-dominant. As expected, increased flow velocities and shear stresses were found during spring tidal conditions (not shown), with spatial patterns comparable to mean tidal range results. Similar patterns were also observed for neap tidal conditions (also not shown); however, velocity and shear stress magnitudes were around 20 to 50% smaller than for mean tides.
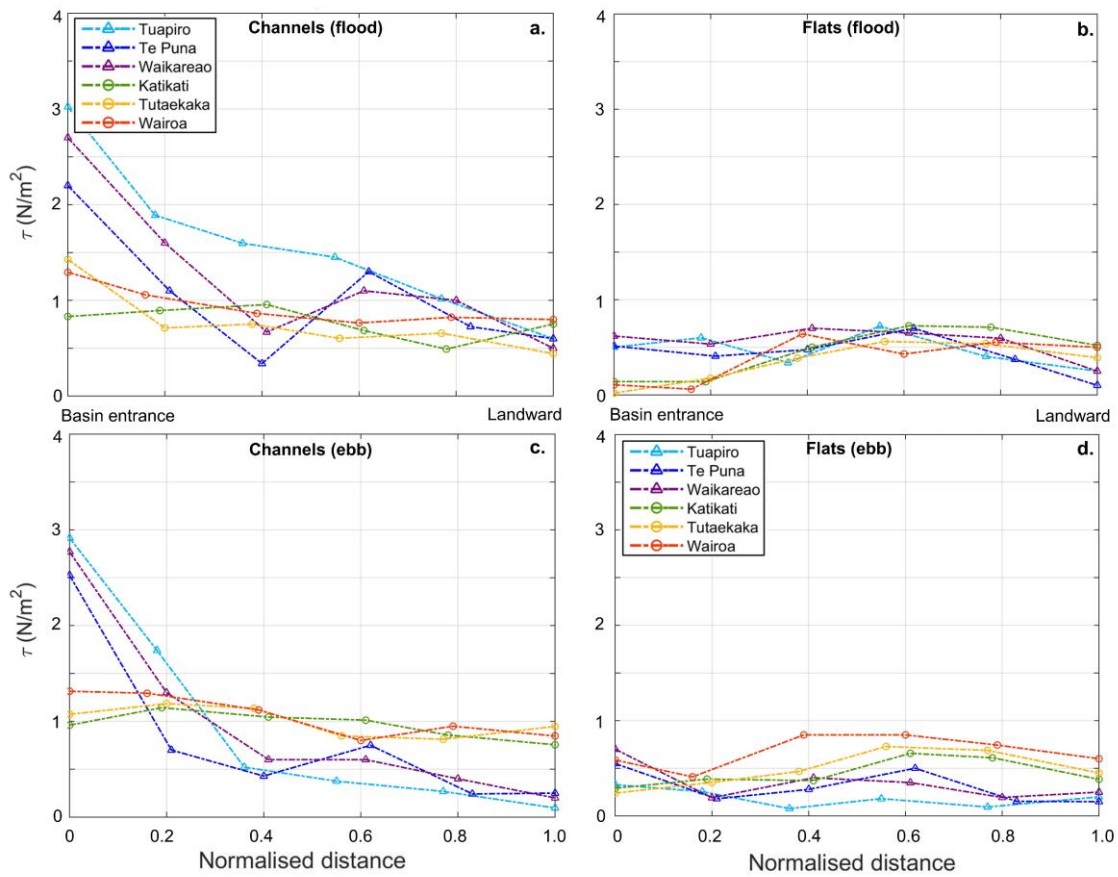
Figure 2.5: Maximum modelled flood (a, b) and ebb (c, d) bed shear stress patterns throughout the six sub-basins, from entrances (left side) to basin centres (right side), for both subtidal [channels (a, c)] and intertidal regions [flats (b, d)]. X-Axes represent normalized distance into a basin. Triangles and circles represent constricted and unconstricted basins, respectively.

26

2.3.3 Tidal Distortion and Asymmetry

Model results for water levels within the six sub-basins were analysed in order to determine changes in tidal distortion and asymmetry of the vertical tide. Tidal amplitude ratios (Figures 2.6a and 2.6b) and relative tidal phases (Figures 2.6c and 2.6d), based on dominant tidal constituent M_2 and most significant overtide M_4, were averaged at six sections within each basin for both subtidal (channels, Figures 2.6a and 2.6c) and intertidal (flats, Figures 2.6b and 2.6d) regions, similar to Figure 2.5. The amplitude ratios (M_4/M_2) provide a direct measure of non-linear tidal distortion (Friedrichs and Aubrey, 1988) throughout the basins. An undistorted tidal signal is characterized by M_4/M_2 ratios of zero. Tidal distortion values were normalized by the limited amount of distortion ($M_4/M_2 < 0.1$) already present within the main estuary, just outside of the sub-basins. Relative tidal phases ($2M_{2\theta} - M_{4\theta}$) indicate the state of the tidal system in terms of asymmetry, with flood dominance for $0° < 2M_{2\theta} - M_{4\theta} < 180°$ and ebb dominance for $180° < 2M_{2\theta} - M_{4\theta} < 360°$ (Friedrichs and Aubrey, 1988). Results illustrate that, in general, tidal distortion increases with distance from the entrance for all sub-basins (Figures 2.6a and 2.6b). Tidal signals within the entrance channels of the six basins are relatively undistorted (left side of Figure 2.6a). Constricted tidal channels (triangles) display weak ebb dominance whereas unconstricted channels (circles) are marginally flood-dominant (left side of Figure 2.6c). Distortion values are generally lowest within the deeper constricted entrance channels. Changes in tidal distortion for subtidal regions (channels) throughout the sub-basins (towards the right of Figure 2.6a) are most apparent in constricted basins, where M_4/M_2 ratios increase by roughly a factor of four (Figure 2.6a, triangles). Subtidal regions in the centre (landward side) of the constricted basins display flood dominance, whereas unconstricted subtidal basin centres are weakly ebb-dominant (right side of Figure 2.6c). Tidal distortion values are shown to be largest in constricted basin channels (right side of Figure 2.6a, triangles).

The pattern of tidal distortions within intertidal regions (flats) located near the basin entrances (left side of Figure 2.6b) indicate distortions generally slightly larger and flood-dominant for constricted basins (triangles). Further landward (towards the right of Figure 2.6b), a pattern emerges that is similar to the subtidal distortion patterns (Figure 2.6a); tidal distortion in basin centres is again largest for constricted basins. Relative tidal phases (Figure 2.6d) suggest flood dominance throughout intertidal areas of constricted basins (triangles) and ebb dominance for unconstricted intertidal regions (circles). Our results indicate that intertidal regions generally experience more tidal distortion than subtidal

27

regions and that distortion within intertidal regions is largest for constricted tidal basins (Figure 2.6b, triangles) independent of distance from the entrance. Relative tidal phase patterns (Figures 2.6c and 2.6d) suggest a flood-dominant environment within constricted basins, whereas unconstricted basins are notably more ebb-dominant. Distortions and tidal phase patterns for spring and neap tidal conditions (not shown) were found to be comparable to the patterns in Figure 2.6, with tidal distortions on average being slightly larger during spring tides.
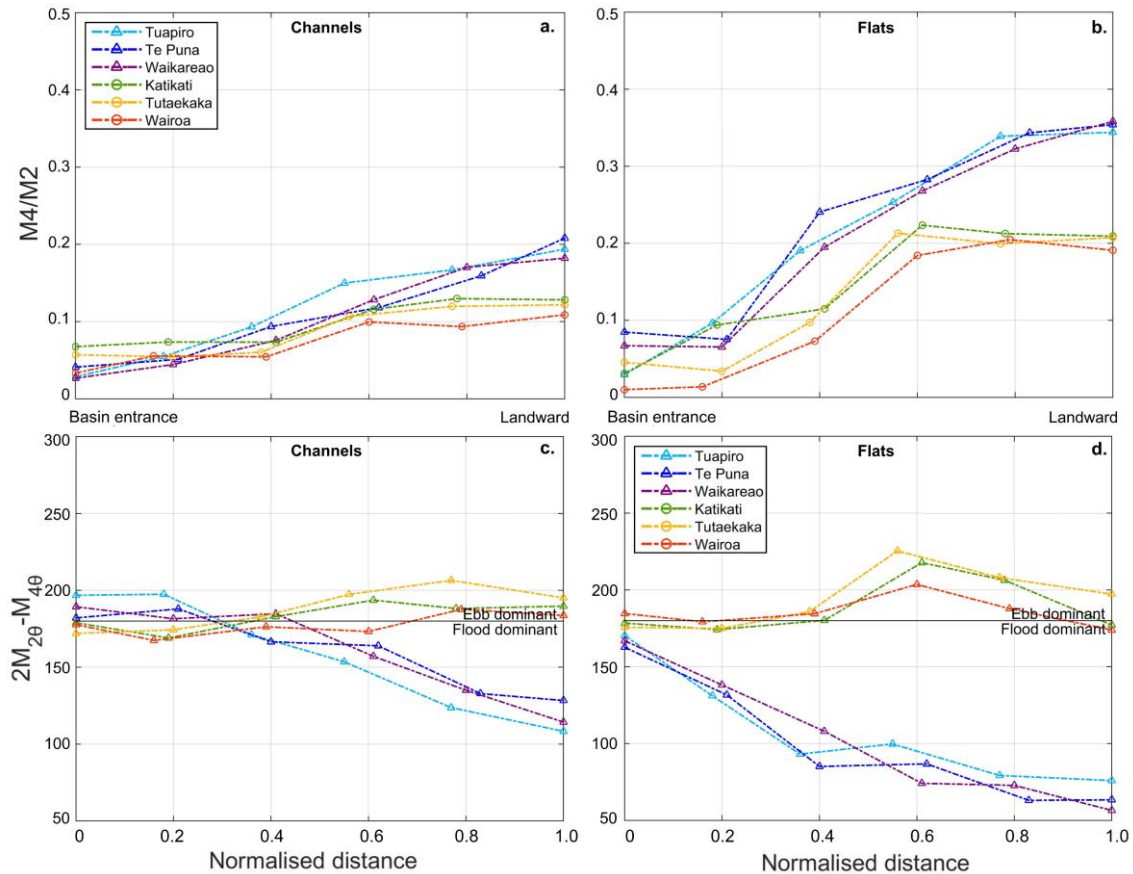
Figure 2.6: Modelled tidal amplitude ratios (a, b) and relative tidal phase patterns (c, d) throughout the six sub-basins, from entrances (left side) to basin centres (right side), for both subtidal [channels (a, c)] and intertidal regions [flats (b, d)]. X-Axes represent normalized distance into a basin. Triangles and circles represent constricted and unconstricted basins, respectively.

2.3.4 Tidal Velocity Asymmetry (TVA)

Horizontal tidal asymmetry patterns, based on modelled tidal velocities, were resolved as part of a further analysis of tidal dominance within the six sub-basins. TVA rates (Figures 2.7a and 2.7b) were calculated based on peak flood and ebb current velocity ratios (u_{fl_max}/u_{ebb_max}) for the six subtidal (Figure 2.7a) and intertidal (Figure 2.7b) locations within each basin, similar to Figures 2.5 and 2.6. These velocity ratios provide an

indication of the transport direction of mainly coarser sediment fractions (e.g. Friedrichs and Aubrey, 1988). An undistorted horizontal tidal signal is characterized by TVA ratios of one; flood and ebb dominance are defined by values greater, and smaller than one, respectively. Velocity asymmetry ratios were normalized by the asymmetry of the horizontal tide present within the main estuary, in a similar manner to the normalization of the vertical tidal signals in Figure 2.6.
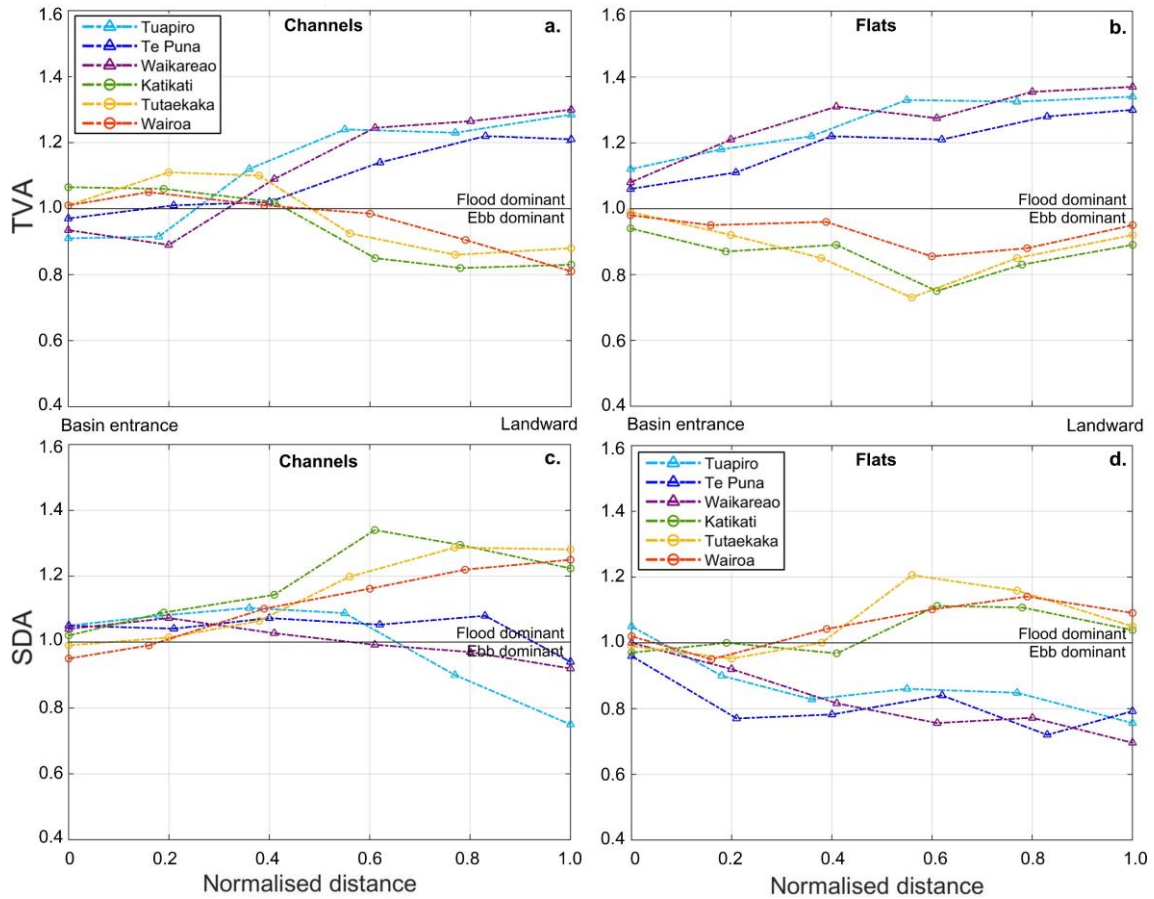
Figure 2.7: Modelled tidal velocity asymmetry [TVA (a, b)] and slack duration asymmetry [SDA (c, d)] throughout the six sub-basins, from entrances (left side) to basin centres (right side), for both subtidal [channels (a, c)] and intertidal regions [flats (b, d)]. X-Axes represent normalized distance into a basin. Triangles and circles represent constricted and unconstricted basins, respectively.

Within constricted basin channels (Figure 2.7a, triangles) peak flood velocities predominantly exceed peak ebb velocities, with the exception of the slightly ebb-dominant entrance channels. Unconstricted basin channel TVA (Figure 2.7a, circles) shifts from weak flood dominance (entrance) to weak ebb dominance (centre). Intertidal regions inside the constricted basins display increasing flood dominance towards the basin centres (Figure 2.7b, triangles), with greatest TVA ratios found inside the two highly divergent basins (Tuapiro and Waikareao). Moderate ebb dominance was found

for unconstricted basin intertidal regions (Figure 2.7b, circles), with asymmetry rates decreasing toward the inner basins (right side of Figure 2.7b).

The overall tidal asymmetry patterns found within the sub-basins (Figures 2.7a and 2.7b) is comparable with the tidal signals identified using the relative tidal phases (Figure 2.6) and hence confirm that the three constricted basins can be characterized as flood-dominant environments. The unconstricted basins are shown to be markedly more ebb-dominant based on both tidal phases (Figures 2.6c and 2.6d) and TVA (Figures 2.7a and 2.7b).

2.3.5 Slack Duration Asymmetry (SDA)

Movement of fine sediment fractions within subtidal and intertidal regions is affected by slack water duration (Dronkers, 2016). In order to quantify the duration of HWS (high water slack) and LWS (low water slack) in the six sub-basins, model results for current velocities (u) were analysed for the same locations used in Figures 2.7a and 2.7b, based on a critical entrainment velocity threshold (u_{cr}) of 0.15 m/s (very fine sand). SDA values (Figures 2.7c and 2.7d) were then calculated using ratios of slack water duration (t_{HWS}/t_{LWS}) for $u < u_{cr}$.

Results show that in the subtidal regions of all lower sub-basins (left part of Figure 2.7c) HWS duration generally exceeds LWS duration, with the exception of the Tutaekaka and Wairoa entrance channels (Figure 2.7c, far left red and yellow circles). Subtidal SDA becomes increasingly flood-directed towards the inner regions of the unconstricted basins (right side of Figure 2.7c, circles), whereas constricted basin centres display weak subtidal ebb dominance (right side of Figure 2.7c, triangles). In the lower unconstricted basins intertidal SDA is weakly ebb-directed, with a switch to weak flood dominance further landward (Figure 2.7d, circles). Intertidal regions throughout the constricted basins (Figure 2.7d, triangles) are notably more ebb-dominant with respect to slack duration.

Slack tide asymmetry patterns can theoretically also be derived from relative tidal phases (Figures 2.6c and 2.6d). A phase difference of $90° < 2M_{2\theta} - M_{4\theta} < 270°$ suggests slack flood dominance, whereas $-90° < 2M_{2\theta} - M_{4\theta} < 90°$ induces ebb-directed slack asymmetry (e.g. Van Maren and Winterwerp, 2012). Based on this tidal phase approach, the ebb-dominant SDA patterns found within intertidal regions of constricted basin centres (Figure 2.7d, triangles) correspond well with the tidal phases of $< 90°$ in these areas (Figure 2.6d, triangles). Similarly, the more flood-dominant SDA patterns in

unconstricted basin centres (Figures 2.7c and 2.7d, circles) coincide with flood-dominant tidal phases around 200° (Figure 2.6c and 2.6d, circles). Weak ebb-dominant SDA patterns shown in constricted basin centre channels (right side of Figure 2.7c, circles) and unconstricted basin lower intertidal flats (left side of Figure 2.7d, triangles) are not reflected in associated tidal phases (Figures 2.6c and 2.6d). Such a mismatch between relative tidal phase signals and SDA ratios has been found in previous studies (e.g. Vermeulen, 2003) and is most likely the result of harmonics such as M_6 affecting slack period asymmetry. These higher order tidal components are not included in the relative tidal phase analyses but do affect SDA ratios.

2.3.6 Basin Dilation Factor

The use of basin geometry characteristics to distinguish between different basin types can aid in the interpretation of tidal asymmetry and bed shear stress patterns. Boon and Byrne (1981) achieved such a differentiation by utilizing the ratio between basin mouth cross-sectional area (A_m) and maximum basin surface area (S_b). From Table 1.3, showing A_m/S_b ratios calculated for the six Tauranga Harbour sub-basins, it can be concluded that these ratios do not distinguish between the different types of basins included in our study.

Table 2.3: Ratio between basin mouth cross-sectional area (A_m) and basin surface area at high tide (S_b).

Sub-basin	BDF	A_m / S_b[a]
Tuapiro	6.05	0.11
Te Puna	4.35	0.19
Waikareao	7.15	0.15
Katikati	1.03	0.15
Tutaekaka	1.20	0.11
Wairoa	0.89	0.10

[a] Ratio between basin mouth cross-sectional area (A_m) and basin surface area at high tide (S_b)

Hence, to more clearly characterize the geometry of the sub-basins, a simple basin dilation factor (BDF) parameter was developed:

$$BDF = \frac{w_{est}}{w_{entr}}$$

(2.3)

where w_{entr} is the basin entrance width, indicating the rate of entrance constrictedness, and w_{est} is the average width of the landward half of the basin. Using this ratio, three specific tidal basin shapes can be distinguished: convergent basins (BDF < 1.0), straight prismatic basins (BDF ≈ 1.0) and divergent basins (BDF > 1.0). Consequently, a greater BDF (BDF > 1.0) refers to basins characterized by a narrow entrance and a divergent

width landwards from the basin mouth. A dilation factor was assigned to each of the six sub-basins (Table 1.3). Tuapiro and Waikareao are characterized by constricted entrances and a relatively wide basin centre, resulting in a large BDF (6.05 and 7.15, respectively). Te Puna, featuring an entrance of similar width to Tuapiro and Waikareao, has a narrower elongated shape, corresponding to a lower dilation factor (BDF = 4.35). Tutaekaka and Katikati are defined by an entrance almost as wide as the basin centres, which is reflected in their BDF (BDF $\approx$ 1.0). Wairoa has a variable geometry and a wide entrance (funnel-shaped), resulting in a BDF below 1.0. Since the three divergent basins cover a relatively large range of dilation factors (BDF > 1.0), semi-log plots were used to display the relationship between BDF and both velocity and slack water asymmetry (Figure 2.8).

Our results indicate that TVA averaged over the basin centre transects (examples in Figures 2.4a and 2.4b, dashed lines) is greatest and flood-directed for divergent basins with high BDF values (solid blue line and triangles in Figure 2.8a). Relatively straight and weakly convergent basins (BDF $\approx$ 1.0) are characterized by somewhat weaker, ebb-directed TVA (Figure 2.8a, circles). Similar patterns are shown for intertidal (flats) and subtidal (channels) regions separately (dashed and dash-dotted grey lines in Figure 2.8a, respectively), with largest (flood- directed) asymmetry values found for intertidal regions within basins with a high BDF (right side of Figure 2.8a).
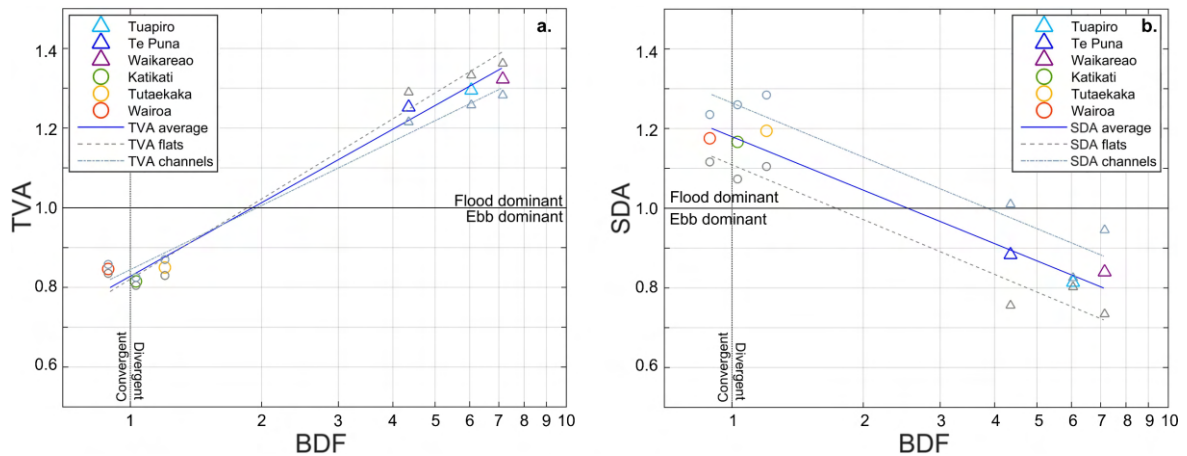
Figure 2.8: Tidal velocity asymmetry [TVA (a)] and slack duration asymmetry [SDA (b)] averaged over basin centre transects (solid blue lines), as a function of basin dilation factor (BDF: see main text). Asymmetries on flats (intertidal) and in channels (subtidal) shown by dashed and dash-dotted grey lines, respectively.

Averaged slack water asymmetry rates in basin centres (Figure 2.8b, solid blue line) demonstrate a pattern that is approximately opposite to the TVA distribution (Figure 2.8a). Here, divergent basins (Figure 2.8b, triangles) are characterized by an ebb-directed asymmetry whereas straight and weakly convergent basins (Figure 2.8b, circles) exhibit

weak flood dominance. Variations in average SDA rates between intertidal (flats) and subtidal (channels) regions (dashed and dash-dotted grey lines, Figure 2.8b) of basins with similar BDFs are shown to be relatively large compared to TVA variations (Figure 2.8a).

Maximum bed shear stresses (τ_{max}) averaged over the sub-basin transects were also related to BDFs. Figure 2.9 shows that shear stresses in divergent basins (triangles) are generally greatest for flooding tides (blue solid line). For increasingly unconstricted basins (BDF $\approx$ 1.0), shear stresses are largest during ebbing tide (Figure 2.9, circles and red dashed line). As expected, shear stress patterns roughly align with ebb- and flood dominance distributions found when analysing TVA (Figures 2.7a and 2.7b). The somewhat divergent shear stress patterns within the two subgroups (BDF $\approx$ 1.0 versus BDF > 1.0) indicate that other factors, such as basin depth, may also play a role here. Our results indicate that basin hypsometry (γ) and BDF are interconnected parameters (higher BDF is associated with a lower γ). Hence, replacing BDF with γ in Figure 2.8 or Figure 2.9 would result in similar patterns for tidal asymmetry or shear stress, respectively.
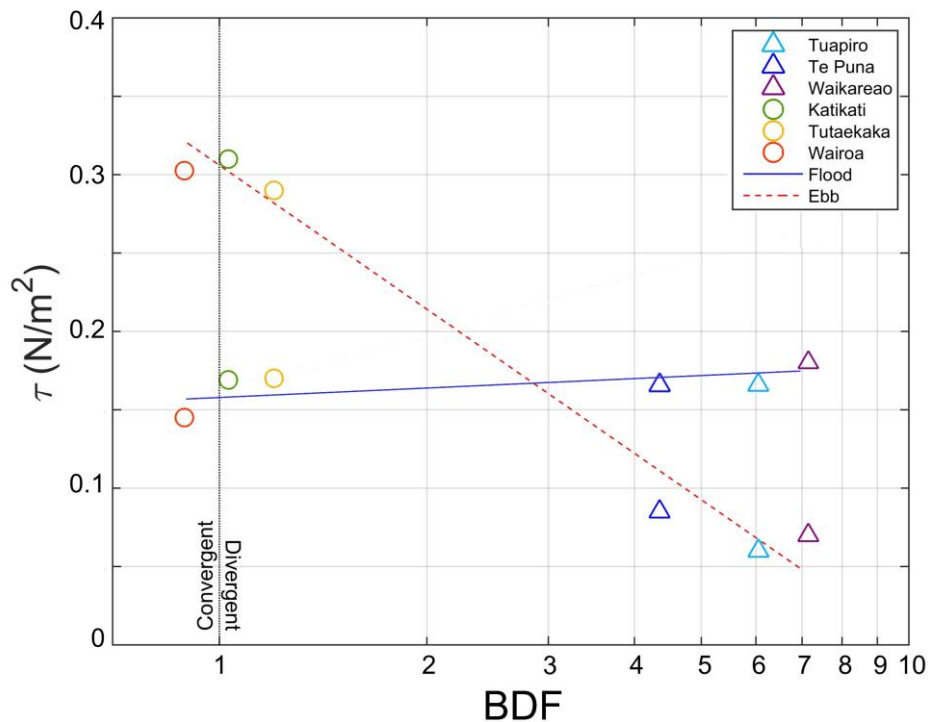
Figure 2.9: Maximum bed shear stresses, averaged over basin centre transects, as a function of basin dilation factor (BDF). Greater dilation factors (divergent basins) result in more flood-dominant shear stress patterns (blue solid line); more convergent basins (smaller BDF) show increased ebb dominance (dashed red line).

The BDF was developed as a simple and indicative parameter useful for identifying trends and general dynamics within our model results. Since we aim to explain tidal asymmetry and shear stress patterns within the centre and upper reaches of the sub-basins, the average width of the relevant upper half of the basins provides a reasonable characterization of the basin geometry. Moreover, sensitivity analysis indicates that when w_{est} is replaced by, for example, the maximum or average width of the upper basin, general tidal asymmetry and shear stress patterns do not change. The relative simplicity of the BDF makes it applicable to a wide range of tidal basin and estuarine systems similar to the sub-basins considered in our study.

2.4 Discussion

2.4.1 Tidal Distortion and Asymmetry

Tidal basin hydrodynamics influence sediment transport potential and intertidal morphological shapes within the basins. We show how varying geometry changes the tidal distortion and asymmetry patterns throughout shallow basins by comparing hydrodynamic model results for constricted and unconstricted geometries. In addition, spatial gradients in bed shear stress were found to be different between these basin types, and from this result we can infer that the associated sediment deposition and erosion potential within the basins will also vary. These results can be linked with the contrasting observed equilibrium hypsometric profile shapes.

Tidal basins defined by a geologically or otherwise constricted entrance and a large BDF (BDF > 1.0), are shown to be characterized by convex-shaped hypsometric profiles corresponding to γ-values of approximately 2.5 (Tuapiro, Te Puna and Waikareao). Model results demonstrate that these constricted basins are very similar with regards to vertical and horizontal tidal asymmetry distribution as well as slack tide duration and bed shear stress patterns, despite their differences in volume, orientation and depth. These infilled basins experience fast tidal flow through the narrow and relatively deep entrance channels, resulting in large associated shear stresses. The entrance channels exhibit weak ebb dominance, in agreement with prior studies (e.g. Moore et al., 2008). The relationship between water depth and rates of tidal distortion was previously explored by Friedrichs and Aubrey (1988) and Zhou et al. (2018). In the latter study, it was suggested that the relative water depth a/h [the ratio between offshore tidal (M_2) amplitude and mean water depth (channel depth)] almost entirely controls tidal distortion. Relatively deep channels, characterized by small a/h values and limited bottom friction, were found to exhibit

limited distortion. The weakly distorted tidal signals within the constricted entrance channels in our study confirm this relationship. Consequently, tidal distortion is somewhat stronger on the nearby shallower (larger a/h), weakly flood-dominant intertidal flats. Slack water asymmetry ratios in lower constricted basins indicate that subtidal areas are slightly flood-dominant, whereas intertidal regions are weakly ebb-dominant.

Further into the constricted basins the increased flow cross-sectional area results in a current velocity and shear stress reduction. Here, the shallower tidal channels become weakly flood-dominant. Tidal distortion further landward increases notably with decreasing depth (larger a/h). The large bottom friction significantly reduces M_2 amplitudes, whereas shallow water distortion increases M_4 amplitudes (Moore et al., 2008). The shallow upper divergent basins are shown to be highly flood-dominant for current velocities, in agreement with previous studies (e.g. Wang et al., 2002). Slack asymmetry results indicate ebb dominance within the shallow constricted basin centres, consistent with previous studies (Van Maren and Winterwerp, 2012; Dronkers, 2016).

Tidal basins with wider entrances are associated with smaller BDFs (BDF $\approx$ 1.0) and less convex hypsometric profiles. Our analysis shows that such relatively straight or weakly convergent basins are characterized by lower intertidal regions and hypsometric curves corresponding to γ-values around 4.0 (Katikati, Tutaekaka and Wairoa). Flow velocities and shear stresses are more evenly distributed throughout these less-infilled sub-basins. The relatively shallow (larger a/h) entrance channels experience current velocities and associated shear stresses smaller than in constricted sub-basins. Tidal distortions in the channels are slightly larger than in the deeper constricted channels and are flood-directed. Further into the basins, flow velocity and shear stress reductions are smaller than for constricted basins. Tidal distortion increases landward, with weakly ebb-dominant velocity patterns found in basin centres. The difference in distortion between the divergent and more convergent tidal basins is predominantly a consequence of the less developed and significantly lower tidal flats (relatively small a/h). These lower intertidal regions also affect slack tide duration, with tidal velocities changing slower around HWS compared to LWS (Dronkers, 2016). Consequently, slack asymmetry was found to be weakly flood-directed throughout the upper unconstricted basins. The more seaward sections of these basins display weak ebb dominance, especially for intertidal areas.

The tidal dominance within all basin types may be enhanced during spring tidal conditions and less prominent during neap tides (Zarzuelo et al., 2016). Previous studies have shown that, depending on tidal basin dimensions, ebb- and flood-dominant patterns for infilled and less-infilled environments may vary (e.g. Ridderinkhof et al., 2014).

In order to substantiate the patterns of tidal asymmetry patterns found for the divergent basin configurations in our study, exploratory idealized hydrodynamic modelling was carried out based on simplified tidal basin geometries. Two short, shallow ellipsoidal basins were designed based on the hypsometric parameters methodology used by Hunt et al. (2015). The resulting intertidal morphologies represent an infilled constricted basin ($\gamma \approx 2.0$) with a relatively deep tidal channel and a less-infilled unconstricted basin ($\gamma \approx 4.0$) with a shallower channel (Figure 2.3, dashed and dotted lines, respectively). Overall dimensions and intertidal profile shapes of the simplified basins (5.0 km × 2.5 km) are comparable to the tidal basin configurations included in our study (see hypsometric curves in Figure 2.3). Flows in both idealized basins were forced with a 1.0m amplitude M_2 tide imposed at the seaward boundary.

Figure 2.10 shows model results for TVA ratios averaged over a tidal cycle for the simplified basin geometries. The lower half of the constricted basin (Figure 2.10a, left side) is characterized by a mainly flood-dominant channel (TVA > 1.0) and weakly ebb-dominant intertidal flats (TVA < 1.0), with a switch to flood dominance on the shallower upper flats. In the basin centre (Figure 2.10a, towards the right), both the subtidal and intertidal are generally flood-dominant, supporting the overall flood-dominant patterns in tidal velocity found for the constricted basins in our study (Figures 2.7a, 2.7b and 2.8). The idealized unconstricted basin centre (Figure 2.10b) is characterized by a very weakly flood-dominant channel, slightly deviating from the weakly ebb-dominant channels found for the unconstricted basins in Tauranga (Figure 2.7a). This result may be due to the bathymetry simplifications in the idealized basin geometries. Intertidal regions of the simplified unconstricted basin (Figure 2.10b) mostly display ebb dominance, comparable to the intertidal ebb dominance found in the unconstricted Tauranga basins (Figures 2.7a, 2.7b and 2.8). Hence, it can be concluded that preliminary idealized modelling of tidal velocities within two relatively short and shallow tidal basin geometries confirms the overall horizontal tidal asymmetry signals found in our study for the constricted and unconstricted tidal basins. A full exploration of the links between idealized basin geometry and tidal velocity patterns is beyond the scope of our current study.
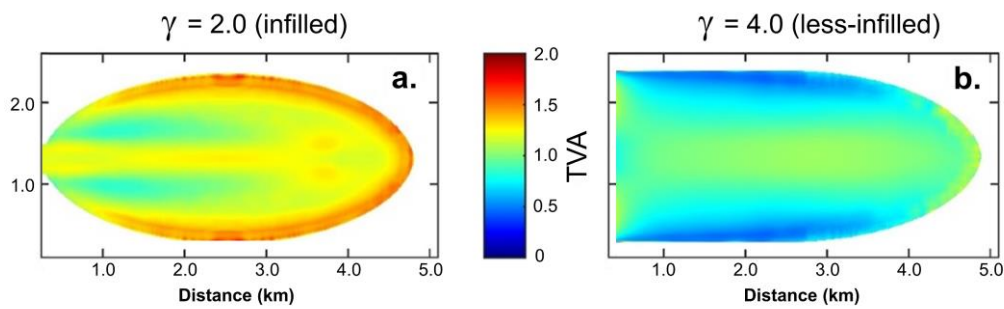
Figure 2.10: Tidal velocity asymmetry (TVA) patterns throughout an infilled (a) and less-infilled (b) idealized basin geometry (see black dashed and dotted lines respectively in Figure 2.3 for hypsometric curves). Flood dominance prevails in the centre of the infilled basin (a), whereas the less-infilled basin is characterized by ebb dominance (b).

2.4.2 Sediment Transport Potential

Conditions with strongly flood-dominant tidal velocities, as exhibited by the divergent sub-basins in our study (BDF > 1.0), imply potential net landward movement of sediment and an infilling environment. The high-energy constricted entrance channels remain relatively deep as sediment deposition is unlikely. During fair weather conditions, net sediment transport within such channels is often directed landwards (Green and Coco, 2007). The narrow entrance channels can significantly affect tidal asymmetry-related sediment transport within an associated basin, as shown in previous studies (e.g. Ridderinkhof et al., 2014). Increased cross-sections further into the basins result in a current-related shear stress reduction and a landward dispersion flux of suspended sediment. Reduced shear stresses in the basin centres create an environment suitable for sediment deposition, especially within the strongly flood-dominant intertidal areas. Comparable results have been found for larger-scale divergent estuarine environments, in which shear stress reduction and increased sedimentation rates positively affect sandbar dimensions (Leuven et al., 2018). Slack water asymmetry, mainly impacting fine sediments, is shown to vary throughout the constricted basins in our study. Flood dominance in the lower subtidal regions suggest landward transport of fines, whereas ebb dominance indicates seaward transport in intertidal regions. Previous studies have suggested however, that peak flow asymmetries may generally be more important than other asymmetries, for transporting sediment through intertidal regions (e.g. Van Maren and Winterwerp, 2012). Consequently, the constricted basins in our study can be described as overall sediment sinks. Related studies have shown that high basin sedimentation rates within estuaries and tidal basins promote convex-shaped hypsometric profile shapes with γ-values around 2.0 (e.g. Boon and Byrne, 1981), consistent with the convex hypsometry curves found for the constricted basins in our study. Increasingly convex hypsometric profiles further reduce slack high water duration and may eventually

favour both tidal velocity and slack duration-related ebb dominance (e.g. Dronkers, 1986, Stark et al., 2017). The weak ebb dominance found in the constricted entrance channels in our study is likely a result of the elevated tidal flats present in the basins and may signify a future switch towards ebb dominance (Le Hir et al., 2000). Such a change in sediment pathways decreases profile convexity and slows down seaward intertidal profile migration. However, previous studies have shown that shallow tidal basins tend to maintain flood dominance unless the tidal flat area becomes very extensive (e.g. Speer and Aubrey, 1985).

Overall, our results show weak tidal velocity ebb dominance within the unconstricted basins (BDF ≈ 1.0), indicating potential for seaward sediment movement. Ebb-directed slack asymmetry in lower intertidal regions may enhance seaward sediment transport. Weak flood-directed slack asymmetry indicates a potential for limited landward transport of fines in the basin centres. However, the ebb-directed tidal velocities likely dominate in these regions, promoting transport of sediment away from basin centres and supporting less convex-shaped hypsometric profiles with lower intertidal flats, consistent with the hypsometric curves found for the unconstricted basins in Tauranga Harbour. Such relatively high-energy intertidal regions experience little seaward migration and may exhibit profile retreat. Based on the earlier mentioned results, the unconstricted basins may be described as sediment sources.

Increased sediment supply results in a more depositional environment, increasing tidal flat width and reducing intertidal profile steepness (Hu et al., 2015). Such morphological changes would increase hypsometric profile convexity or decrease profile concavity within tidal basins and enhance seaward progradation. Abundant sediment supply can result in a convex-shaped hypsometric profile despite the presence of potentially erosive hydrodynamic processes. Sediment supply reduction promotes a more concave (or less convex) hypsometric profile shape, characterized by a slower seaward progradation or profile retreat (Maan et al., 2015).

2.4.3   Implications for Management

The morphological evolution of estuarine intertidal regions affects coastal ecosystem functioning, port and estuary navigability and coastal protection potential worldwide (Temmerman et al., 2013; Bouma et al., 2014). A relatively stable intertidal morphology (e.g. Mariotti and Fagherazzi, 2013), which returns to the same configuration following a perturbation (e.g. storms), promotes long-term ecosystem stability. Engineering works,

aimed at protecting the coastline or facilitating navigation, can drastically affect intertidal regions by displacing large amounts of sediments directly, through the works themselves, as well as indirectly by modifying sediment transport patterns (Maan et al., 2015). The functionality of intertidal regions in terms of ecology as well as coastal defence depends on cross-shore profile shapes. Elevated intertidal regions with convex-shaped hypsometric profiles are desirable in terms of their ability to offer coastal protection, decreasing flooding and coastal erosion potential (Kirby, 2000). Our results indicate that the promotion of a constricted basin geometry may increase sedimentation potential within shallow basin centres, theoretically resulting in higher intertidal areas. Alternatively, our study illustrates that the removal of an entrance constriction may result in a higher-energy tidal basin environment. The associated increased erosion potential may be preferred in shallow environments where navigability is of prime importance. However, more research is needed to validate our results and to determine the applicability of such a management approach for tidal basins systems with divergent geometries and sizes.

De Vet et al. (2017) showed that intertidal regions in the Eastern Scheldt estuary in the Netherlands experienced erosion after the construction of a storm barrier that constricts the estuary entrance. This result contradicts our own findings that indicate the promotion of sediment deposition within constricted basins. The intertidal erosion in the Scheldt was hypothesized to be a result of decreasing tidal range and velocities within the now constricted estuary, and a relative increase in importance of wind waves. Moreover, the Eastern Scheldt is a larger and deeper basin than the basins considered in our study. Consequently, tidal prisms are contrasting and fetch in the Scheldt is long enough to promote wind waves significantly larger than can be expected over the tidal basins of Tauranga Harbour. Studies, such as the aforementioned by De Vet et al. (2017) highlight the complicated nature of hydrodynamic and morphological response to changing geomorphic boundary conditions within specific geomorphic settings. Hence, the ability to predict tidal asymmetry conditions and morphological changes in distinct tide-dominated systems is useful when developing management strategies and may indicate areas which are more likely to demand focused management (Wang et al., 2002; Zhou et al., 2017).

Anthropogenically induced climate change and sea level rise may drastically affect estuarine intertidal regions. Projected changes in relative mean sea level could alter intertidal morphology, increase tidal inundation, and profoundly affect the fragile balance

sustaining many coastal ecosystems (e.g. Zhou et al., 2017; Hanslow et al., 2018). Changes in tidal range as a result of sea level rise will affect tidal flow velocities and associated shear stresses over intertidal regions, potentially altering intertidal profile shapes in both constricted and unconstricted estuarine systems and tidal basins (Hu et al., 2015; Liu et al., 2019).

2.4.4 Study Limitations

The results from the hydrodynamic model developed for Tauranga Harbour have allowed for the examination of how shallow tidal basin geometry influences tidal processes, shear stress patterns, and intertidal profile shapes within divergent basin configurations. However, processes related to morphological evolution within tidal basins are complex and comprise interactions driven by hydrodynamics as well as by sediment characteristics, meteorological conditions, local geology, freshwater input and biological processes. Our current model is a simplified depth-averaged representation of a natural estuarine system. In order to obtain a more detailed overview of tidal asymmetry patterns and sediment transport potential within shallow basins, a three-dimensional model representation of basin hydrodynamics should be considered that includes secondary circulation and density-driven flows as a result of temperature and salinity gradients. Additionally, simulating the transport of a mixture of sediment grain sizes through basins with a range of geometries would further enhance our understanding of morphological responses to changes in basin hydrodynamics. As shown in previous studies, basin size and geometry have a strong impact on the magnitude and direction of tidal asymmetry and sediment transport potential (e.g. Ridderinkhof et al., 2014). The results found in our study are mainly applicable to shallow small-scale tidal basin systems with little fresh water input.

An important aspect not considered in our study is the impact of vegetation on intertidal profile stability. The six sub-basins within Tauranga Harbour are all characterized by the presence of small mangrove trees in the upper intertidal areas. These vegetated regions represent a small but relatively stable part of the total intertidal area of tidal basins (Hunt et al., 2016). Mangroves have the ability to influence intertidal profile shapes by enhancing sedimentation and promoting hypsometric profile convexity (Van Santen et al., 2007; Bryan et al., 2017; Mullarney et al., 2017). Intertidal vegetation can also alter current velocities and directions and attenuate waves (Henderson et al. 2017; Horstman et al., 2018). Low-energy environments with high potential for sediment deposition, such

as the constricted basins in our study, may promote intertidal vegetation growth (Balke et al., 2014).

Wind-driven currents and waves have the potential to alter sediment deposition rates and transport pathways resulting from tidal processes (e.g. Hunt et al., 2015). Wind and waves effects may be limited within the relatively sheltered constricted basins, whereas unconstricted basins may be susceptible to erosion from morphologically significant waves originating seaward of the basin entrances. These wind-related processes will be explored in detail in future research.

2.5   Conclusions

The geometry of tidal basins modulates hydrodynamic processes, sediment transport potential and associated morphological changes within these basins. This study indicates that differences in tidal energy within two contrasting shallow sub-basin configurations have a substantial impact on spatial bed shear patterns and local hypsometric profile shapes. Sub-basins with a constricted geometry (large BDF) are shown to be characterized by a convex hypsometric curve and elevated intertidal regions; whereas unconstricted sub-basins (low BDF) display a less convex hypsometry with lower intertidal profiles. Numerical model results demonstrate that the tidal distortion within constricted basins is generally larger than in unconstricted basins. Distortion rates were found to be dependent on relative water depth, with largest tidal distortions encountered in the shallow upper intertidal regions of constricted basins. Constricted basins generally exhibit flood-dominant peak TVAs, promoting landward sediment transport, whereas unconstricted basins were found to be overall weakly ebb-dominant. Slack water duration asymmetries were partially ebb-dominant within constricted basins, suggesting potential for seaward transport of fine sediment, compared to a weakly flood-directed slack asymmetry in unconstricted basins. Modelled current velocities and associated bed shear stresses in the centres of the basins are shown to be largest for the unconstricted basins. Consequently, overall potential for sediment deposition within these comparatively high-energy environments can be assumed to be limited, resulting in limited hypsometric profile convexity and their possible role as sediment source. The larger potential for sediment deposition within the calmer mainly flood-dominant constricted basins, enhances hypsometric profile convexity and supports the function of the basins as a sediment sink. Our study highlights the need to define the limits of applicability of numerical modelling results obtained in estuaries and tidal basins with specific geomorphic settings. Further

work will investigate how wind-induced currents and waves modulate tidal asymmetry and sediment transport potential within specific geometric basin configurations.

Appendix A

The hydrodynamic model of Tauranga Harbour was calibrated and validated by comparing modelled water levels and tidal current magnitudes to field measurements for 13 locations throughout the estuary (Figure 2.1b, black and green dots). Hydrodynamics were simulated for a two-week period, including a spring-neap tidal cycle, between 25 October and 8 November 2015. A range of eddy viscosity values (ranging from 0.1 to 50) and Mannings bottom roughness coefficients (ranging from 0.15 to 0.40) were used to test the predictive capabilities of the model. The best calibration was achieved with a uniform eddy viscosity value of 10 m_2/s and a spatially varying bottom roughness (see text for details).
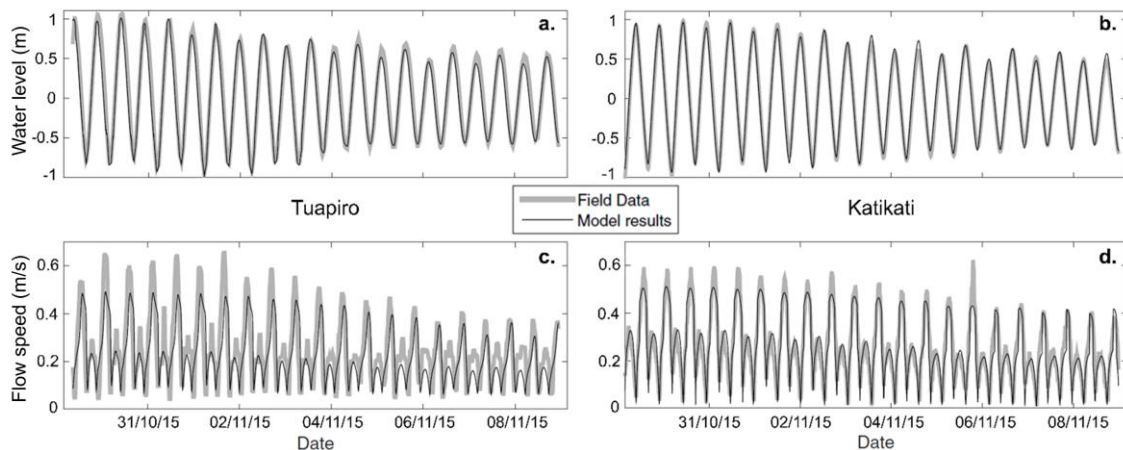
Figure 2.11: Comparison of field data (thick grey lines) and model output (thin black lines) time series of water levels (+MLOS) (a, b) and flow speeds(c, d) for the Tuapiro (a, c) and Katikati (b, d) sub-basins (see Figure 2.1 for locations).

The ability of the model to reproduce the hydrodynamics was verified by comparing model output to field measurements for a 12-day period representing the second half of the 2015 field campaign (examples shown in Figure 2.11). To quantify model prediction quality, three widely-used statistical measures of model skill were calculated for the 13 model calibration locations. Model accuracy was determined using the root mean square error (RMSE) and mean absolute error (MAE), and model skill was assessed with the Brier Skill Score (BSS) (Sutherland et al., 2004). Water levels were generally very well replicated by the model throughout the estuary, with performance ratings according to the BSS classification proposed by Sutherland et al. (2004) found to be 'Excellent' at all 13

locations (Table 2.4). Current velocity predictions were rated either 'Good' or 'Excellent', with the exception of two locations.

Table 2.4: Brier Skill Scores (BSSs) for water levels and current speeds at 13 model validation locations.

Location	Water level BSS	Current speed BSS
1	0.98	0.82
2	0.97	0.40
3	0.96	0.15
4	0.99	0.84
5	0.98	0.55
6	0.98	0.22
7	0.95	0.45
8	0.98	-
9	0.98	0.54
10	0.98	-
11	-	0.82
12	0.96	-
13	0.97	-

Colours indicate performance ratings of 'Excellent' (green), 'Good' (light green), 'Reasonable/Fair, (yellow) or 'Poor' (orange). Note that data was not always available for locations 8, 10, 11, 12 and 13. Locations are shown in Figure 2.1.

Modelled current speeds at station 3, located on the edge of the main channel of the northern basin (Figure 2.1b, southeast of Tuapiro) were classified as 'Poor'. This disparity between model output and measurements is most likely a result of highly variable bottom elevations in this area that cannot be represented with enough accuracy in the current model, along with the fact that tidal flows through a secondary channel westward of the main channel may have contributed to measured current speeds, resulting in an irregular current speed signal. Measured current speeds at station 6, located eastward of the entrance of the Tutaekaka sub-basin (Figure 2.1b, yellow cross), also show an irregular pattern that the model was not able to reproduce for part of the 12 days, resulting in a 'Reasonable/Fair' classification. Table 2.5 shows mean and standard deviation values for the model accuracy and skill measures, averaged over all 13 model validation locations.

Table 2.5: Mean and standard deviations of model accuracy (RMSE, MAE) and skill (BSS) values averaged over all model validation locations.

Parameter	Water level Mean	Std	Current speed Mean	Std
RMSE (m)	0.094	0.022	0.112	0.030
MAE (m)	0.070	0.014	0.101	0.034
BSS	0.973	0.012	0.532	0.257

Chapter 3

The Effects of Wind-Generated Currents on Velocity Asymmetry in Tidal Basins with Varying Geometries

Calm weather conditions in the northern basin of Tauranga Harbour

Contribution of Authors

Chapter 3 presents the article entitled "The effects of wind-generated currents on velocity asymmetry in tidal basins with varying geometries", a version of which was published in *Earth Surface Processes and Landforms* in 2021. I also developed several idealised models of tidal basins using Delft3D, with supervision from Julia C. Mullarney, and Karin R. Bryan. I wrote MATLAB scripts to process and analyse the model data. I prepared all the figures for the article and wrote the initial and subsequent drafts of the manuscript. Julia C. Mullarney, Karin R. Bryan, and Christian Winter provided valuable comments and discussions. Additionally, my co-authors, Julia C. Mullarney and Karin R. Bryan, edited my drafts, and provided editorial help responding to reviewers' comments.

3.1 Introduction

Tidal basins are ubiquitous features of coastal regions across the globe (Friedrichs and Aubrey 1988). Human interventions and climate change contribute to the vulnerability of these tidal systems, impacting tidal dynamics, sediment transport patterns and morphodynamic stability (e.g. de Swart and Zimmerman, 2009; Leuven et al., 2019). The size and geometry of a tidal basin regulate the shape of the tidal wave and the associated hydrodynamic processes within such a basin (e.g. Ridderink et al., 2014; Boelens et al., 2018). The astronomical tide may become strongly distorted inside a basin, resulting in asymmetries in the sea surface elevation (vertical tide) and the velocity field (horizontal tide) (Boon and Byrne, 1981). Vertical tidal distortion in relatively shallow, friction-dominated systems (Zhou et al., 2018) can be evaluated by comparing principal semi-diurnal tidal constituents (M_2) and quarter-diurnal overtides (M_4), to provide an indication of the morphodynamic status of a system (Friedrichs and Aubrey, 1988). Asymmetries in horizontal tidal velocities (TVA; the ratio between peak ebb and peak flood flow) and slack tide duration can provide insight into potential sediment transport directions for larger and smaller sediment grainsizes, respectively (e.g. Dronkers, 2016; De Ruiter et al., 2019). Previous research has shown that divergent (where the width increases landward) and infilled microtidal basins, characterised by a convex hypsometric profile, may experience flood-directed horizontal tidal asymmetry (in which the peak flood currents are stronger than the peak ebb currents). The shallow intertidal combined with the tendency for sediment to be retained or new sediment imported mean that these accretionary tidal systems can support vegetation and are desirable for their ability to offer coastal protection, decreasing potential for flooding and coastal erosion. Conversely, convergent and less infilled basins with concave profiles may display greater ebb-dominance and hence be preferable in coastal regions where navigability is of prime importance (e.g. De Ruiter et al., 2019; Meerman et al., 2019).

Tidal basin hydrodynamics and sediment transport potential can be further modulated by meteorological events. Previous studies have considered the effects of meteorological forcing within estuarine regions and tidal basins on, for example, entrance velocity profiles (Narvaez and Valle-Levinson 2008), subtidal water transport (Buijsman and Ridderinkhof, 2007), residual circulation (Herrling and Winter, 2015), bottom shear stress (Alekseenko and Roux, 2017) and sediment dynamics (Christiansen et al., 2006). Hunt et al. (2016) define meteorological conditions that contribute to 'morphological significant' wave events, meaning events that create waves which cause the critical bed shear stress

to be exceeded. Wind events can also have a direct impact on water level setup, and wind- and wave-driven flow in estuaries and tidal basins (De Vet et al., 2018). The shifting influence of these wind-related processes on subtidal and intertidal hydrodynamic processes is commonly reduced to three categories of forcing: stormy, windy (moderate), and calm conditions (Le Hir et al, 2000; Talke et al., 2008). Wind-induced shear stresses resulting from moderate to stormy conditions are generally considered to be capable of modulating the direction of flow and sediment transport in shallow subtidal and intertidal estuarine regions (e.g. Narvaez and Valle-Levinson, 2008; Green & Coco, 2014, de Vet et al., 2018).

Semi-enclosed tidal basins and estuaries characterised by shallow intertidal areas incised by deeper channels may experience local wind-generated currents superimposed on tidal current patterns. Such residual wind-induced currents can be characterised by downwind flows over shallow intertidal regions and upwind flows in deeper subtidal channels, as indicated by numerical modelling studies (e.g. Wong, 1994; Sanay and Valle-Levinson, 2005; Hunt et al, 2015), and observational evidence (e.g. Narvaez and Valle-Levinson, 2008, Juarez et al., 2019). These opposed wind-induced flow patterns can be attributed to a balance between wind- and bottom stress for intertidal regions, and currents associated with pressure gradients in deeper subtidal channels (Narvaez and Valle-Levinson, 2008; Alekseenko et al., 2013). Besides generating residual currents, wind forcing also has the potential to interact with tidal waves in shallow regions by causing velocity distortion patterns to change. Such wind-driven modifications of a tidal signal may be reflected by fluctuations in the asymmetry of horizontal flow velocities.

In order to accurately predict horizontal velocity asymmetry (VA) conditions and morphological changes in tidal basins, development of a thorough understanding of the stability relationships between basin geometry, hydrodynamics, and sediment transport potential is crucial. Meteorological forcing can play an important role in modulating these relationships (e.g. Bolle et al., 2010). However, the links between basin geometry, velocity asymmetry and wind-induced forcing have not yet been fully explored in previous modelling studies of shallow tidal systems. An earlier numerical modelling study, focused on a number of shallow microtidal basins of Tauranga Harbour, New Zealand, indicated that basin geometry (meaning planform shape) and intertidal hypsometry have a substantial impact on tidal asymmetry within the basins (De Ruiter et al., 2019). Here, we extend this previous work, by showing how hydrodynamics in short tidal basins with specific geometries are modulated by superimposed wind-driven

residual currents. We evaluate changes in horizontal velocity patterns, to investigate how wind-generated currents affect velocity distortion inside these shallow tidal basins.

3.2 Methods

3.2.1 Idealised Numerical Models

Two idealised hydrodynamic models of tidal basins were developed using the Delft3D-FLOW modelling software (Lesser et al, 2004), based on the hypsometric parameters methodology developed by Hunt et al. (2015) and adapted by De Ruiter et al. (2019). The simplified ellipsoidal basin geometries were inspired by the planform shape and hypsometric characteristics of the short, shallow tidal basins found in the microtidal lagoon of Tauranga Harbour, New Zealand, as described in a prior study by De Ruiter et al. (2019). This study, which focused on six microtidal basins, revealed that basins characterised by divergent geometries represent convex hypsometric profiles, described by hypsometry exponent (γ) values around 2.0 (Boon and Byrne, 1981). These divergent basins were found to be indicative of flood-dominant accretionary environments. Increasingly convergent basins were found to be more ebb-dominant, and were characterised by less convex hypsometric profiles ($\gamma \approx 4$), similar to the empirical relationship between hypsometry and planform estuary geometry found by Leuven et al. (2018).

The length and width of the full model domains used in our present study are 10 and 2.5 km, respectively, with a 10 m grid resolution (example shown in Figure 3.1a). The two idealised models were forced with a 1.0 m amplitude M_2 tidal signal imposed at the seaward model boundary, which is situated 5 km away from the basin entrances (dashed line in Figure 3.1a). Consequently, the 5 km long landward sections of the model domains (right side of example in Figure 3.1a) represent the tidal basin morphologies. These sub- and intertidal domains represent a divergent infilled basin (Figure 3.1b) with a constricted entrance and a relatively deep tidal channel (convex hypsometric profile, $\gamma \approx 2.0$; dashed line in Figure 3.1d), and a less-infilled unconstricted convergent basin (Figure 3.1c) with a shallower channel (concave hypsometric profile, $\gamma \approx 4.0$; dotted line in Figure 3.1d). A sensitivity analysis indicated that hydrodynamic results from cases in which the models were characterised by more than five vertical sigma layers were virtually identical to depth-averaged model results. Hence, to minimise computational time, five equal-depth sigma-layers were applied in the vertical. A spatially uniform bottom friction Manning coefficient of 0.02 s/m$^{1/3}$ was applied throughout both idealised models. The wind drag

coefficient (C_d) in Delft3D is assumed to be linearly dependent on wind speed, reflecting increasing roughness of the water surface with increasing wind speed (Smith and Banke, 1975). Three wind drag coefficients determine breakpoints in the piece-wise linear function of wind drag and wind speed. Default values for the three coefficients (0.00063, 0.00723, 0.00723) were used for the idealised models, resulting in a C_d of 0.0013 for wind speeds of 10 m/s (Deltares, 2014).
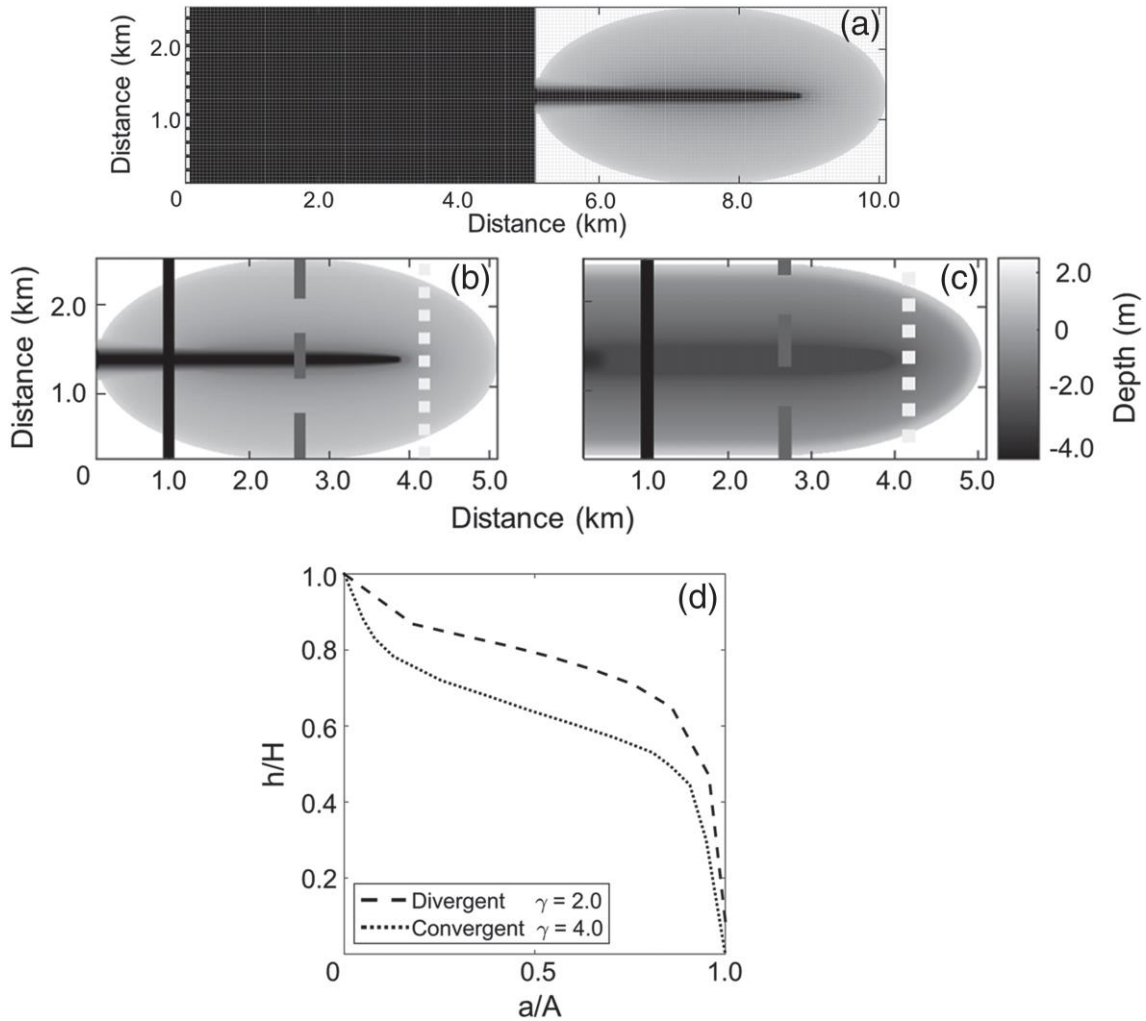
Figure 3.1: Example of model domain (a) and bathymetries for the idealized tidal basin models (b, c) with associated hypsometric curves (d). Tides were forced at the seaward boundary of the domains (dashed white line in a). The infilled divergent basin (b) is characterized by elevated intertidal regions and a deeper channel ($\gamma \approx 2.0$; dashed line in d), whereas the less infilled convergent basin (c) has a greater average water depth with a somewhat shallower channel ($\gamma \approx 4.0$; dotted line in d). Lines in (b) and (c) show locations of cross-sections through the lower (solid black lines), centre (dashed grey lines) and upper (dotted grey lines) sections of the basin.

3.2.2 Meteorological Characteristics

The frequency distribution of regional wind events for Tauranga Harbour was analysed using four years (2015-2018) of hourly climatic data obtained from the Tauranga Airport

meteorological station (red cross in Figure 3.2a). Figure 3.2b shows the probability of occurrence for specific six- and twelve-hour wind events. Observations were filtered to include only wind events for which hourly wind speeds and directions during the event deviate less than 2 m/s and 20° from the mean wind speed and direction, respectively. Autocorrelated wind events were excluded, assuming a minimum time of four hours between discrete events. Overall, mean wind speeds range between 1.5 to 12 m/s, with the most frequent wind events (darker blue markers) characterised by wind speeds smaller than 7 m/s. South-westerly to westerly (210-280°) offshore winds are dominant in Tauranga Harbour, illustrated by the large number of relatively frequent wind events (darker blue circles and triangles) found for these wind directions. The offshore winds are accompanied by less frequent (lighter blue markers) landward northerly to easterly (10-90°) and south-easterly winds (120-140°), with the former likely representing afternoon-to-evening sea breeze events. Notably, variation in wind characteristics for twelve-hour wind events (triangles) is greatest for landward winds (10-150°), whereas variations in six-hour wind event (circles) characteristics are more evenly distributed between landward and seaward wind conditions.
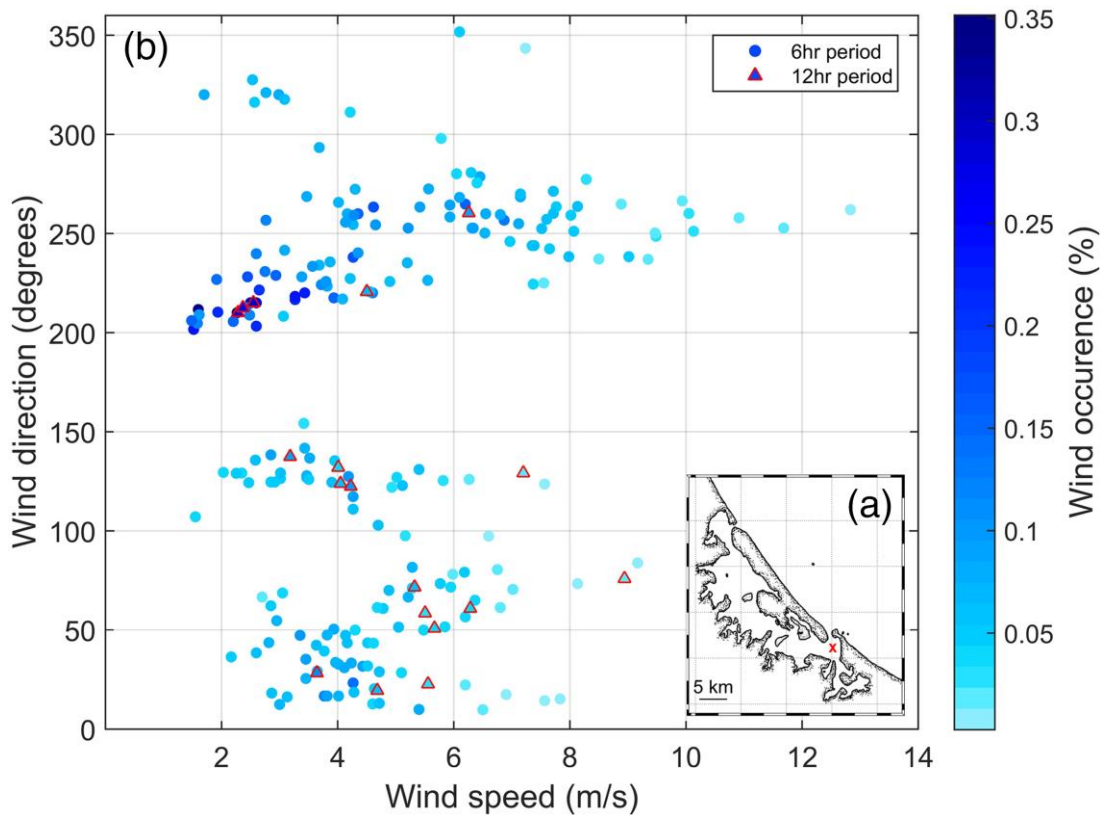
Figure 3.2: (a) Overview of wind conditions in Tauranga Harbour, with location of Tauranga Airport meteorological station indicated by a red cross. (b) Probability of occurrence (colours) for 6- and 12-h wind events (circles and triangles, respectively) plotted as a function of wind speed and direction for the Tauranga Harbour region, based on 4 years (2015–2018) of meteorological observations.

50

3.2.3 Model Runs

To evaluate the interaction between tidal forcing and wind-induced processes, a number of three-dimensional model runs were conducted. Model runs for both idealised basin geometries were forced by a range of wind speeds (2, 6, 12 m/s), wind directions (0º, 90º, 180º, 270º), and wind event durations (3, 6, 12 hours), to approximately encompass the range of conditions observed in the meteorological data of the Tauranga Harbour region (Figure 3.1b). The three wind event durations represent roughly a quarter, half, and full tidal cycle, respectively. An overview of the modelled wind parameters is shown in Table 3.1. For both basin geometries, each variable for wind speed, direction and event duration was used with all other combinations of these parameters (first three columns of Table 3.1). Additionally, for shorter wind events (3 and 6 hours), a wind event timing parameter (synchronised to early or late flooding and ebbing tide) was also included (Table 3.1, fourth column). Consequently, 84 model simulations were carried out for each basin. Each model scenario was run for one tidal cycle after a hydrodynamic spin-up period of two tidal cycles. We focus on an individual tide, to rule out the complexity induced by wind characteristics on longer timescales. Throughout the idealised experiments, basin morphology was fixed rather than coupled to a morphological model and updated. This approach allows for the control of the basin geometry and hypsometry as well as the meteorological forcing on hydrodynamics to be determined in a systematic way (Coco et al., 2013; Hunt et al., 2015).

Table 3.1: Wind parameters used in numerical model runs

Wind speed (m/s)	Wind direction (º)	Wind event duration (hr)	Wind event timing[a] (-)
2	0	3	FL_{start}
6	90	6	FL_{end}
12	180	12	EBB_{start}
	270		EBB_{end}

[a] Wind event timing refers to whether the wind forcing coincides with early (start) or late (end) flooding (FL) or ebbing (EBB) tide

3.3 Results

In order to assess the interaction between tidal processes and wind-generated currents in tidal basins with varying geometries, modelled current velocity patterns were analysed throughout the two idealised basins. Changes to the horizontal velocity asymmetry (VA)

were resolved based on the modelled peak flood- and ebb-directed current velocities ratios (u_{fl_max} / u_{ebb_max}) over a tidal cycle. Undistorted horizontal velocity patterns are characterized by VA ratios of one. We define velocity asymmetry ratios greater and smaller than one as flood- and ebb-dominant respectively, recognizing that these VA ratios represent not only asymmetries in tidal velocities (previously defined as TVA; e.g. De Ruiter et al., 2019), but also include the effects of wind-induced currents. The horizontal velocity asymmetry ratios provide an indication of potential sediment transport directions inside the tidal basins (e.g. Friedrichs and Aubrey, 1988). Figure 3.3 shows depth-averaged velocity asymmetry patterns throughout the idealised tidal basin geometries based on model results that include tidal forcing only (TVA). These results highlight the mainly flood-dominant velocity asymmetry exhibited by infilled, divergent basins (Figure 3.3a), as opposed to the more ebb-dominant asymmetry patterns found inside the less-infilled, convergent basin (Figure 3.3b).
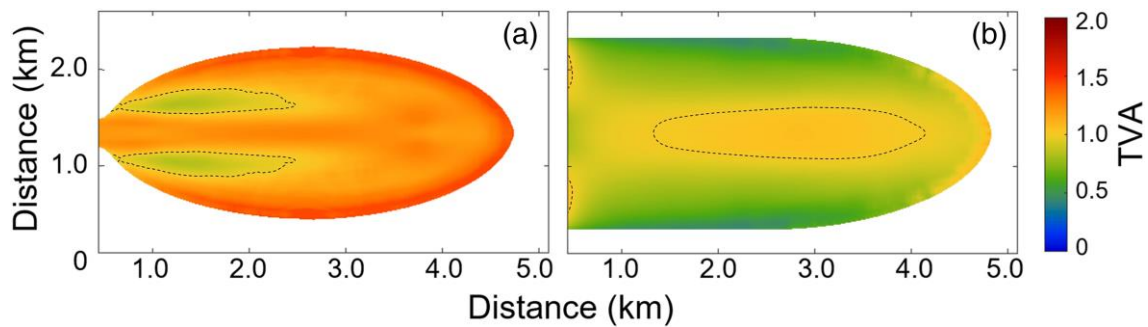
Figure 3.3: Modelled tidal velocity asymmetry patterns inside the idealized infilled divergent (a) and less infilled convergent (b) tidal basin geometries, calculated using the depth-averaged velocity with tidal forcing only, from de Ruiter et al. (2019). The dashed black lines represent TVA = 1. Flood dominance prevails in the centre of the divergent basin (TVA > 1), whereas the convergent basin is characterized by ebb dominance (TVA < 1).

3.3.1 Wind Direction

Figures 3.4 and 3.5 illustrate the combined effects of modelled tide- and wind-generated currents on velocity asymmetry patterns throughout the divergent (Figure 3.4) and convergent (Figure 3.5) basins. These depth-averaged VA results are based on modelled 6 m/s wind events occurring over the full duration of the tidal cycle (12.25 hours), including winds parallel to (along-channel; easterly and westerly winds) and perpendicular to (across-channel; northerly and southerly winds) the tidal channels. The results in Figure 3.4 indicate that for divergent basins tidal forcing combined with the across-channel northerly (Figure 3.4a) or southerly (Figure 3.4c) winds result in similar but opposite (mirrored) VA patterns. Both the largest (indicating flood dominance) and

the smallest (indicating ebb dominance) VA ratios occur on the side of the basin where the wind originates (upwind). When tides are combined with northerly winds, for example, largest VA ratios (VA ≈ 1.6, dark red area) occur in the upper intertidal region located northward of the tidal channel (Figure 3.4a). The smallest VA ratios (green area) for tides combined with northerly winds can be found in the lower northerly intertidal region (VA ≈ 0.7, green area). Inside convergent basins, maximum (red areas) and minimum (blue areas) VA ratios are mainly found in the upper basin regions for northerly (Figures 3.5a) and southerly (Figures 3.5c) winds. Flood dominance is promoted in upper northern (southern) regions of the basin by northerly (southerly) winds (red areas in Figures 3.5a and 3.5c), similar to the VA patterns in the divergent basin, described above.
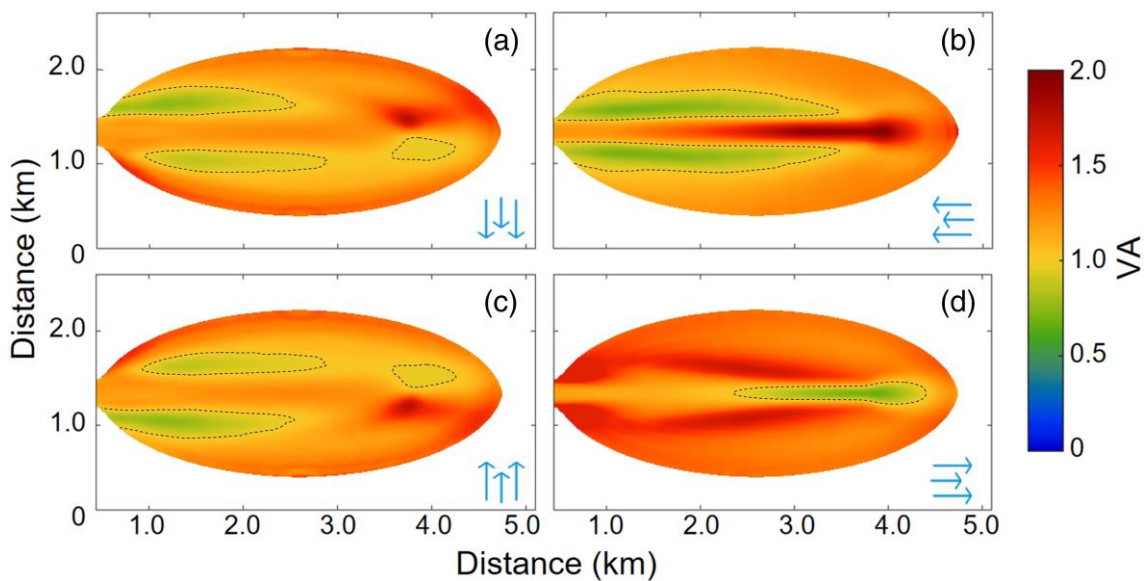
Figure 3.4: Modelled velocity asymmetry patterns inside the idealized divergent tidal basin, based on 12-h moderate (6 m/s) wind events from four different directions (indicated by blue arrows). The dashed black lines represent VA = 1. VA ratios greater than one indicate flood dominance; ratios smaller than one suggest ebb dominance.

Along-channel winds generate currents in shallow regions that are aligned with the wind direction, and modulate horizontal velocity signals, causing an increase in intertidal ebb dominance (landward winds; Figure 3.4b and 3.5b, green-blue areas) or flood dominance (seaward winds; Figure 3.4d and 3.5d, red areas) in both basins. The deeper subtidal channels experience wind-induced currents in the opposite direction to the channel-parallel winds, promoting subtidal VA ratios that contrast with intertidal VA patterns.
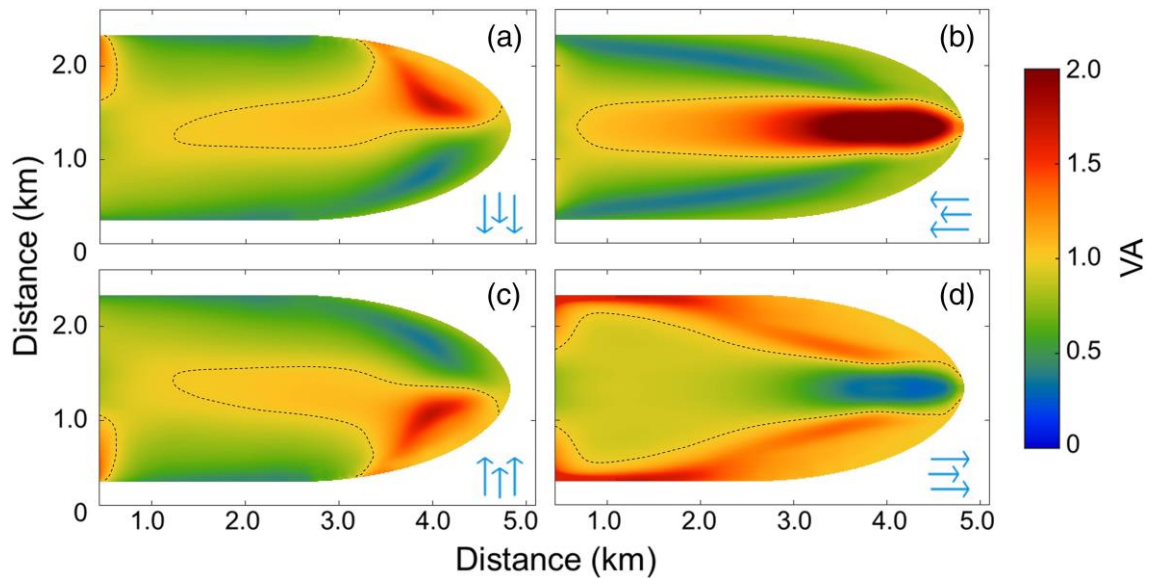
Figure 3.5: Modelled velocity asymmetry patterns inside the idealized convergent tidal basin, based on 12-h moderate (6 m/s) wind events from four different directions (indicated by blue arrows). The dashed black lines represent VA = 1.

In order to isolate the effects of wind forcing on velocity asymmetry, the differences between the modelled wind- and tide-modulated VA described above (Figures 3.4 and 3.5) and the VA for the tide-only case (Figure 3.3) were analysed. The resulting spatial VA patterns, indicating residual wind-induced VA changes ($VA_{tw} - VA_t$) over a tidal cycle, are shown for the divergent (Figure 3.6) and the convergent basin (Figure 3.7). Differences in velocity asymmetry of zero indicate no net wind effects; increasing wind-induced flood and ebb dominance are defined by values greater, and smaller than zero, respectively. The overall spatial distribution of flood- and ebb- dominant basin regions in Figures 3.6 and 3.7 is similar to the VA patterns in Figures 3.4 and 3.5. The results indicate that when the effects of wind forcing on velocity asymmetry are separated from the effects of tidal forcing, the greatest differences in VA (dark red and blue colours) for northerly (Figures 3.6a and 3.7a) and southerly (Figure 3.6c and 3.7c) winds are found in the upper regions of both basins. VA for these across-channel 6 m/s wind conditions ranges between 0.8 (1.2) on the upwind side, indicating increased flood dominance, and -0.7 (-1.1), increased ebb dominance, on the downwind side of the divergent (convergent) basin. Our results show that the strongest differences to the tide-only case are generated by across-channel winds in the convergent basin. Nonetheless, these VA differences are mainly constrained to the upper sections of the basin.
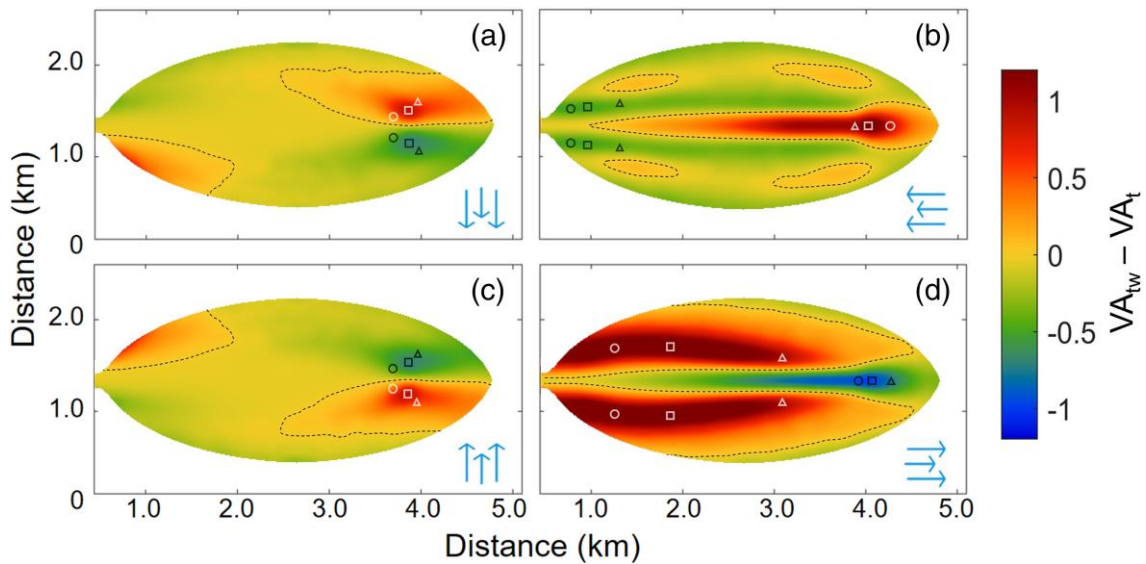
Figure 3.6: Differences in velocity asymmetry ($VA_{tw} - VA_t$) induced by winds (relative to tide-only) inside the idealized divergent tidal basin, based on 12-h moderate (6 m/s) wind events from four different directions (indicated by blue arrows). The dashed black lines represent $VA_{tw} - VA_t = 0$. Positive VA ratios indicate increased flood dominance; negative VA ratios suggest ebb dominance. Markers show locations of maximum flood (white markers) and ebb dominance (black markers) increase for light (2 m/s; triangles), moderate (6 m/s; squares) and strong (12 m/s) wind conditions

Downwind-directed currents generated by along-channel winds force VA differences throughout the intertidal regions of the divergent (convergent) basin that range between -0.6 (-1.2) for seaward winds (Figures 3.6b and 3.7b) and 1.1 (1.2) for landward winds (Figures 3.6d and 3.7d). The upwind-directed currents that develop in the deeper subtidal regions (tidal channels) are illustrated by VA ranging between 1.1 (1.35) for seaward winds and -1.05 (-1.3) in the case of landward winds. The largest increases in velocity asymmetry occur in the subtidal regions (tidal channels) for 6 m/s winds, indicated by the square white markers (maximum VA increase). The largest VA decreases are generally found in the upper sections of both basins (black markers towards the right in Figures 3.6b, 3.6d, 3.7b and 3.7d). Along-channel winds generate the most significant VA differences in the convergent basin.

3.3.2 Wind Speed

The velocity asymmetry patterns found in model results for the divergent and convergent tidal basins described above are based on moderate wind speeds of 6 m/s for 12-hour wind events. Figure 3.8 illustrates how wind speed influences depth-averaged VA inside the tidal basins. Patterns of velocity asymmetry difference inside the divergent basin are shown for three wind speeds: 2 m/s, 6 m/s, and 12 m/s. These wind speeds represent light, moderate and strong landward (along-channel) wind conditions, respectively, based on

the meteorological data analysed for Tauranga Harbour (see Figure 3.1). The results indicate that greater (smaller) wind speeds typically promote more (less) extreme VA inside a basin, without substantially changing overall velocity asymmetry patterns.
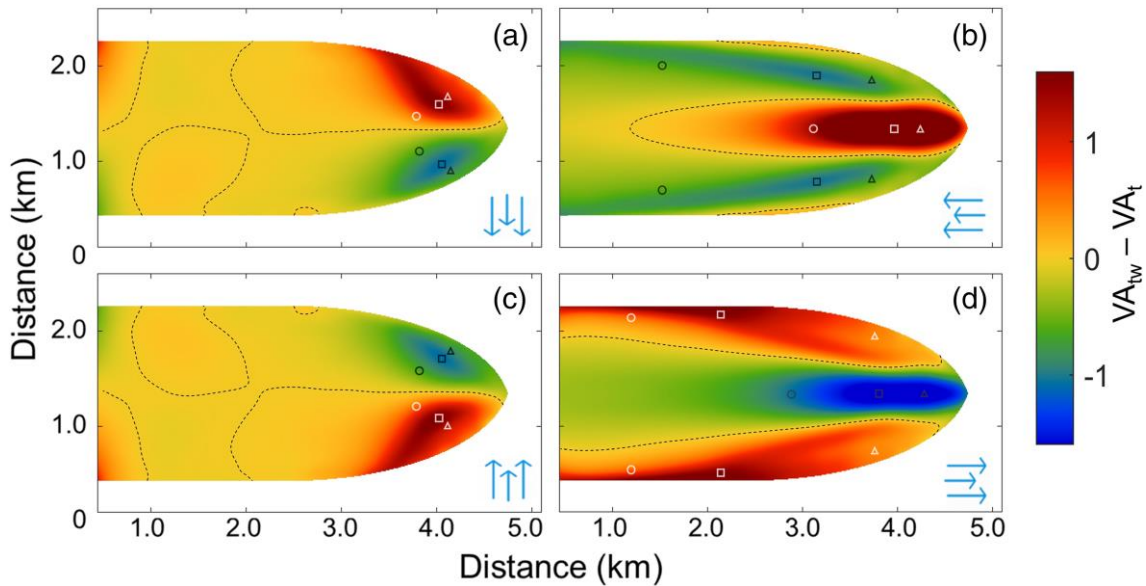
Figure 3.7: Differences in velocity asymmetry ($VA_{tw} - VA_t$) induced by winds inside the idealized convergent tidal basin, based on 12-h moderate (6 m/s) wind events from four different directions (indicated by blue arrows). The dashed black lines represent $VA_{tw} - VA_t = 0$. Markers show locations of maximum flood (white markers) and ebb dominance (black markers) increase for light (2 m/s; triangles), moderate (6 m/s; squares) and strong (12 m/s) wind conditions.

Exact locations of the maximum changes in velocity asymmetry vary depending on wind speed and basin shape, as indicated by the markers in Figures 3.6 and 3.7. For across-channel northerly (Figures 3.6a and 3.7a) and southerly winds (Figures 3.6c and 3.7c), wind speed only marginally affects the spatial distribution of maximum VA change in both basins. Locations of maximum VA change for along-channel winds are more closely correlated to wind intensity (markers in Figures 3.6b, 3.6d, 3.7b, and 3.7d), especially in the convergent basin (Figures 3.7b and 3.7d). The flood-directed currents induced by channel-parallel seaward winds in the subtidal channels (Figures 3.6b and 3.7b, dark red areas) result in a maximum VA increase (VA > 1.0) in the upper part of the basin for all modelled wind speeds (white markers). VA maxima occur slightly further upstream for stronger wind speeds (circles), with wind-induced VA representing a 50 to 90% increase compared to the tide-only case. Locations of greatest VA reduction (green to blue areas) resulting from seaward-directed currents, are located in the lower intertidal regions of the divergent basin on both sides of the tidal channel (Figure 3.6b, black markers). In the convergent basin (Figure 3.7b) the spatial distribution of VA minima for is more dependent on the strength of the seaward winds. Channel-parallel landward winds (270°), promote maximum VA increase (increased flood dominance) in the shallow intertidal

regions of both basins (Figure 3.6d and 3.7d, dark red areas). Strong landward winds (circles) push the locations of maximum change in VA, representing a 40 to 60% increase compared to tide-only conditions, further towards the basin entrance (VA > 1.0). Landward winds produce maximum VA reductions in the upper regions of the deeper tidal channel (Figure 3.6d and 3.7d), with the locations of maximum change again being modulated by wind intensity (black markers).
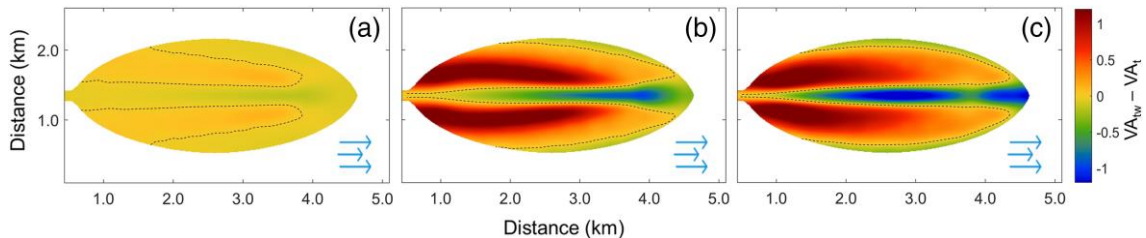
Figure 3.8: Example of the changes in velocity asymmetry ($VA_{tw} - VA_t$) for different wind speeds inside the divergent basin, based on 12-h along-channel (landward) wind events with speeds of (a) 2, (b) 6 and (c) 12 m/s. In general, stronger wind speeds promote more extreme VA ratios without substantially changing the overall patterns of velocity asymmetry

The difference in spatial VA distributions within the two basin geometries is not only modulated by wind intensity, but also linked to the depth-dependence of velocity asymmetry. The shallowest sections of the intertidal regions in the less-infilled convergent basin are located further away from the middle of the basin (the tidal channel), when compared to the more abundant shallow sections of the infilled divergent basin. Hence, the associated locations of maximum VA change are likewise found more in the upper reaches of the convergent basin.

In general, our results indicate that wind speed variation does not substantially change basin-scale velocity asymmetry patterns for all four modelled wind directions in both the divergent and convergent basins, as shown by the example in Figure 3.8 (see above). Consequently, in order to focus on the effects of wind event duration and phasing on VA patterns, subsequent model results are discussed for moderate wind speeds of 6 m/s only.

3.3.3 Wind Event Duration

The effects of varying wind event duration on depth-averaged VA patterns in both idealised basins were analysed for the parallel across-basin transects shown in Figure 3.1b and 3.1c, representing the lower (solid black lines), centre (dashed grey lines) and upper (dotted grey lines) basin regions. The basins were forced by moderate 6 m/s across- and along-channel wind events with durations of 3, 6 and 12 hours, representing roughly a quarter, half and full tidal cycle, respectively. Figure 3.9 shows examples wind- and tide-

modulated VA results for wind events centred on flooding tide in the lower (Figures 3.9a and 3.9d), centre (Figures 3.9b and 3.9e), and upper (Figures 3.9c and 3.9f) regions of the divergent (Figures 3.9a-c) and convergent (Figures 3.9d-f) tidal basins. Consequently, the shortest wind event (3 hours, dotted grey lines) covers mid-flood tide conditions, the 6-hour event (dashed grey lines) incorporates a full flooding tide and the 12-hour wind forcing (solid black lines) encompasses a full tidal cycle. The modelled VA patterns indicate that moderate wind speeds occurring over 3 hours during flooding tide (grey dotted lines in Figure 3.9) can affect velocity asymmetry patterns within both basin configurations, when compared to tide-only conditions (dashed-dotted red lines). VA changes are especially apparent within central and upper basins (Figures 3.9b,c and 3.9e,f) and are generally most substantial for channel-parallel winds, as also described in previous sections. A doubling of wind event duration (from 3 to 6 hours) produces an approximately proportional increase in VA changes within all basin regions, indicating that an increase in wind event duration can result in substantially more extreme VA in tidal basins. Similar results were found for 3- and 6-hour wind events modelled throughout both basin geometries during ebbing tide conditions, though overall VA changes were somewhat less substantial (not shown).

VA model results for 12-hour wind events (solid black lines in Figure 3.9), do not consistently follow the above relationship between wind event duration and VA. Since these wind events cover a whole tidal cycle, both flooding as well as ebbing tidal processes are modulated within a single event. Consequently, the resulting VA patterns can deviate from the VA patterns associated with wind events that only affect one tidal stage (3- and 6-hour events). For example, VA patterns for along-channel winds in the lower convergent basin (right panels of Figure 3.9d) show an overall increase in flood dominance (greater VA) from the 3-hour (dotted lines) to the 6-hour event (dashed lines). However, VA model results for the 12-hour wind event do not show a further increase in flood dominance; the basin generally becomes more ebb-dominant (VA < 1.0), with the exception of the higher intertidal regions for westerly winds (black lines in lower right panel of Figure 3.9d). These results suggest that in addition to wind event duration, the timing of wind forcing, relative to the tidal phase may also affect VA within tidal basins.
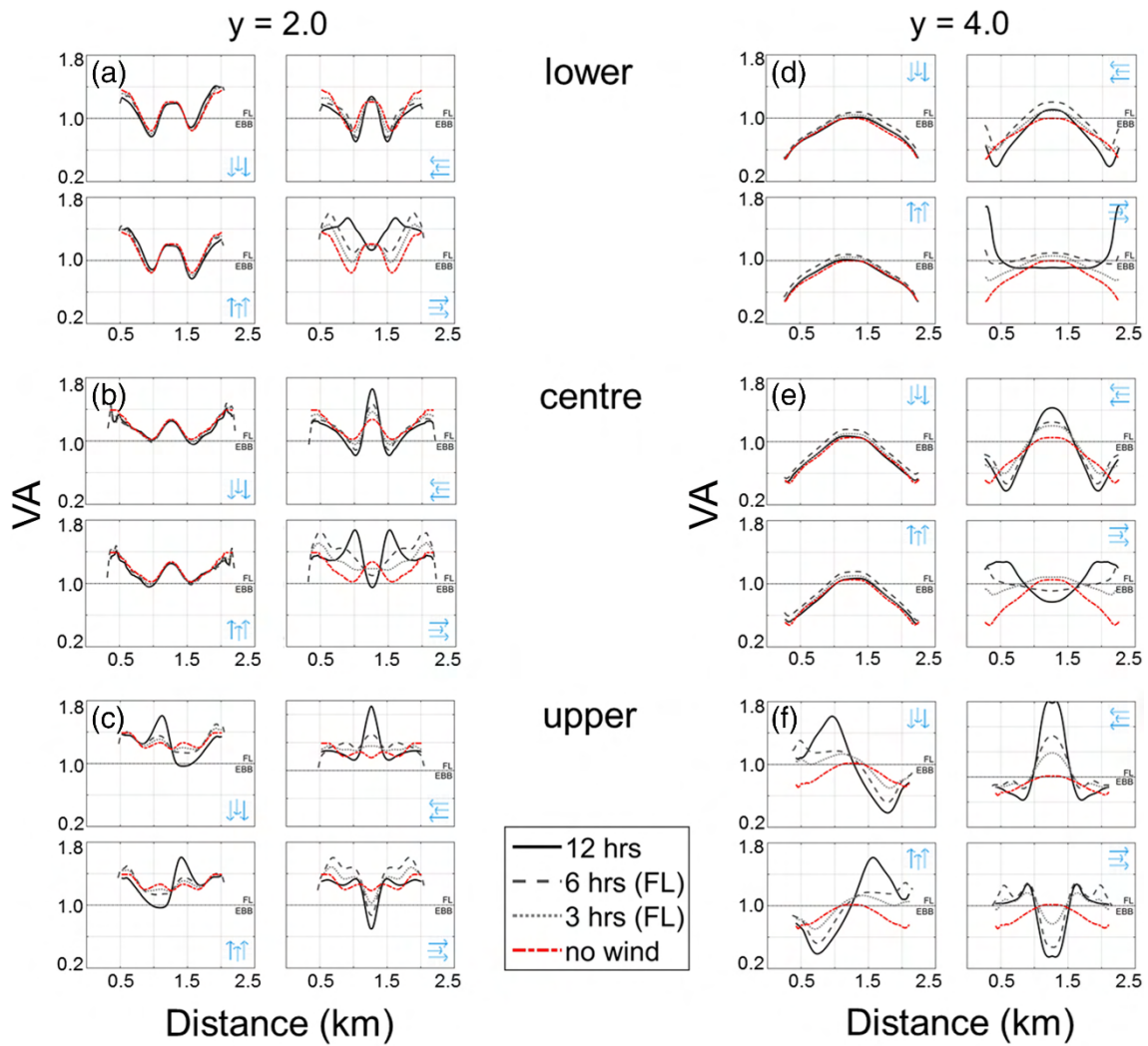
Figure 3.9: The effect of duration. Modelled velocity asymmetry for the cross-sections through the lower (a, d), centre (b, e) and upper (c, f) sections of the divergent (a–c) and convergent (d–f) idealized basins. Results are shown for moderate (6 m/s) wind events with three different durations: 12 h (solid black lines), 6 h (dashed grey lines) and 3 h (dotted grey lines). The latter two wind events coincide with a full and half (mid) flooding tide event, respectively. Dashed-dotted red lines show tide-only VA results as a reference. Each of the four subpanels reflects a different wind direction

3.3.4   Wind Event Phase

The effects of wind event phasing on depth-averaged VA patterns was further explored by analysing model results based on 3-hour moderate wind forcing with varying starting times relative to low tide. Relevant model outcomes are presented for lower (Figures 3.10a and 3.10d), centre (Figures 3.10b and 3.10e), and upper (Figures 3.10c and 3.10f) regions of the divergent (Figures 3.10a-c) and convergent (Figures 3.10d-f) idealised basins, similar to Figure 3.9. Two of the scenarios coincide with flooding tide conditions, with the first event commencing during early flood (first three hours, solid black lines) and the additional event covering late flooding tide (last three hours, grey dashed lines).

59
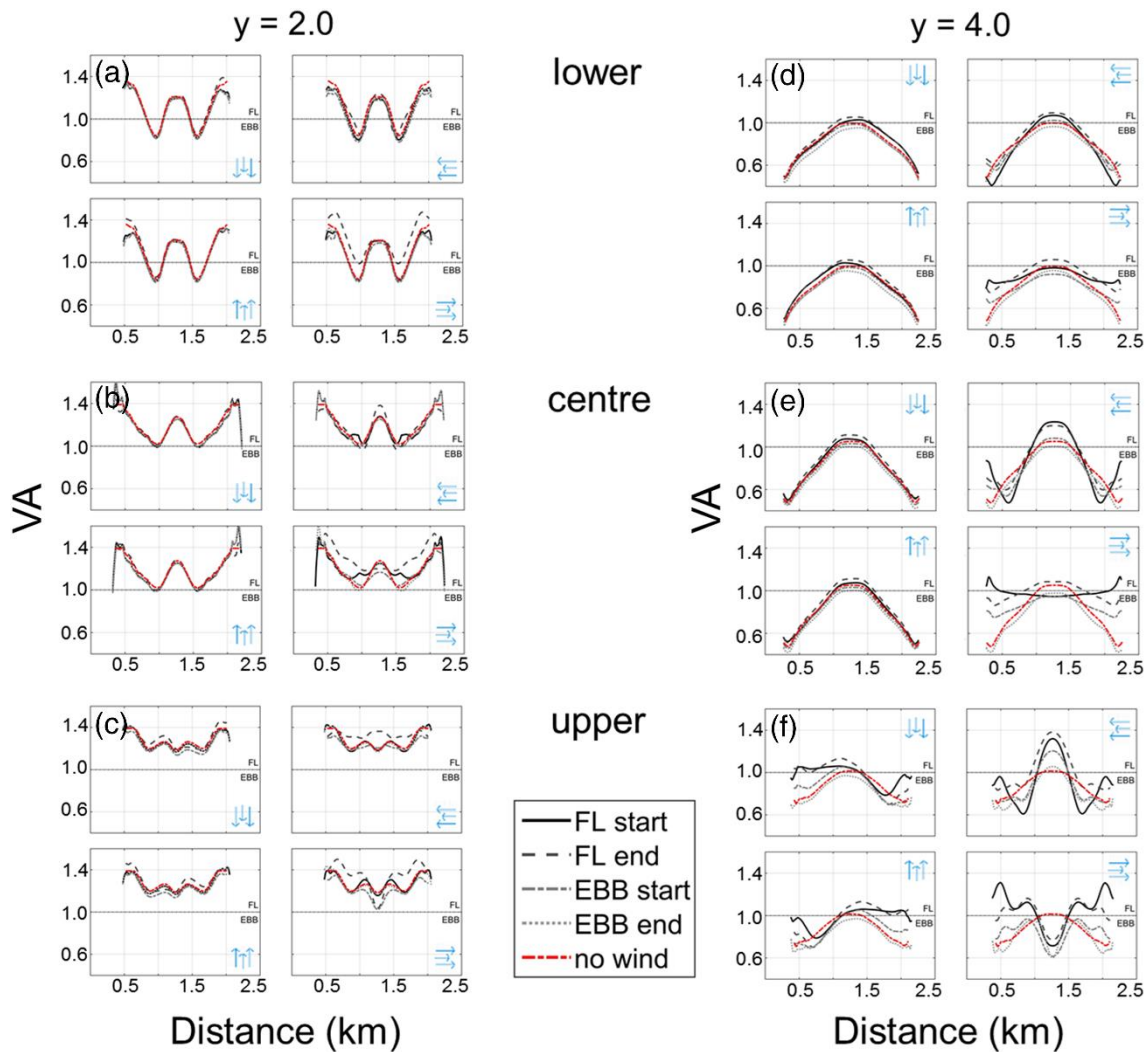
Figure 3.10: The effect of timing (phase). Modelled velocity asymmetry for the cross-sections through the lower (a, d), centre (b, e) and upper (c, f) sections of the divergent (a–c) and convergent (d–f) idealized basins. Results are shown for 3-h moderate (6 m/s) wind events with varying phasing. Wind events coincide with early flooding tide (solid black lines), later flooding tide (dashed grey lines), early ebbing tide (dashed-dotted grey lines) and late ebbing tide (dotted grey lines). Dashed-dotted red lines show tide-only VA results as a reference

The remaining two wind events coincide with early (grey dashed-dotted lines) and late (grey dotted lines) ebbing tide. The results suggest that the changes in VA from tide-only conditions (red dashed lines) in the lower regions of both basins (Figures 3.10a and 3.10d) are primarily affected by wind events coinciding with late flooding tide (grey dashed lines). Similar results are observed for central basin regions (Figures 3.10b and 3.10d), with wind forcing starting during lower flooding tide (solid black lines) and early ebbing tide (grey dashed-dotted lines) also resulting in noteworthy VA changes, especially for along-channel winds (Figure 3.10b and 3.10d, right panels). Velocity asymmetry patterns in upper convergent basin regions (Figure 3.10f) experience the greatest effects of short event (3 hour) wind forcing. The overall velocity asymmetry signals shown in Figure 3.10

imply that wind events coinciding with flooding tide produce the most substantial VA changes within both tidal basin geometries.

3.4 Discussion

Wind events can have a strong impact on hydrodynamics in shallow and short tidal basins. Locally generated wind-induced currents can alter both the magnitude and the direction of horizontal velocity asymmetry in such basins (e.g. Duran-Matute et al., 2014). We show that the resulting patterns of velocity asymmetry are not the sum of the velocities caused by tide-only forcing and those caused by wind-only forcing, but depend on a number of wind- and basin-related interactions. Our model results indicate that wind direction is the driver of the largest changes in VA, with smaller contributions from changes in wind speed, and basin geometry and hypsometry. Previous studies have indicated that hydrodynamics can be modulated by wind-generated currents in both intertidal (e.g. de Vet et al., 2018) and subtidal (e.g. Herrling and Winter, 2015) regions. Our study illustrates that wind forcing is capable of fully reversing the direction of horizontal velocity asymmetry signals in both intertidal and subtidal domains of shallow tidal basins.

3.4.1 Effects of Wind Forcing on Velocity Components

Wind forcing has the potential to modulate maximum, residual, and tidal flow components of current velocity and velocity asymmetry. Evaluating variations in these velocity components separately can be challenging, as their responses to changes in external forcing can be interlinked. However, an analysis of velocity signals inside the basins for a number of different wind conditions (not shown) indicates that the overall effects of wind forcing on tidal velocity components, specifically M_2 and M_4 velocities (U_{m2} and U_{m4}), are relatively small. Moderate to strong 12-hour winds were found to mainly influence tide-averaged maximum and residual flow velocities in the centre of the basins, with additional localised small changes in Um2 of maximum ~15%. The wind-induced U_{m2} variations likely occur because the wind duration (12 hours) is comparable to the M_2 tidal period (~12.4 hours). Overtide velocities (U_{m4}) are not affected by 12-hour wind forcing. Similarly, wind events with a duration of 6 hours induce relatively small U_{m4} changes (maximum ~25%) in both basins, because the wind duration is similar to the M_4 period (~6.2 hours). Shorter wind events (< 6 hours) were found to affect only residual and maximum flow velocities, with negligible changes in tidal harmonic characteristics. Moderate to strong channel-parallel winds induce M_2 and M_4 amplitude changes in both basins of less than 1 cm. Additionally, wind-setup is limited inside the basins, with water

level differences between basin entrances and upper reaches of the basins rarely exceeding 6 cm. Consequently, the VA changes found inside the shallow tidal basins in our study result primarily from wind-induced changes in tide-averaged maximum and residual components of current velocity, with only small changes to the tidal components of velocity asymmetry.
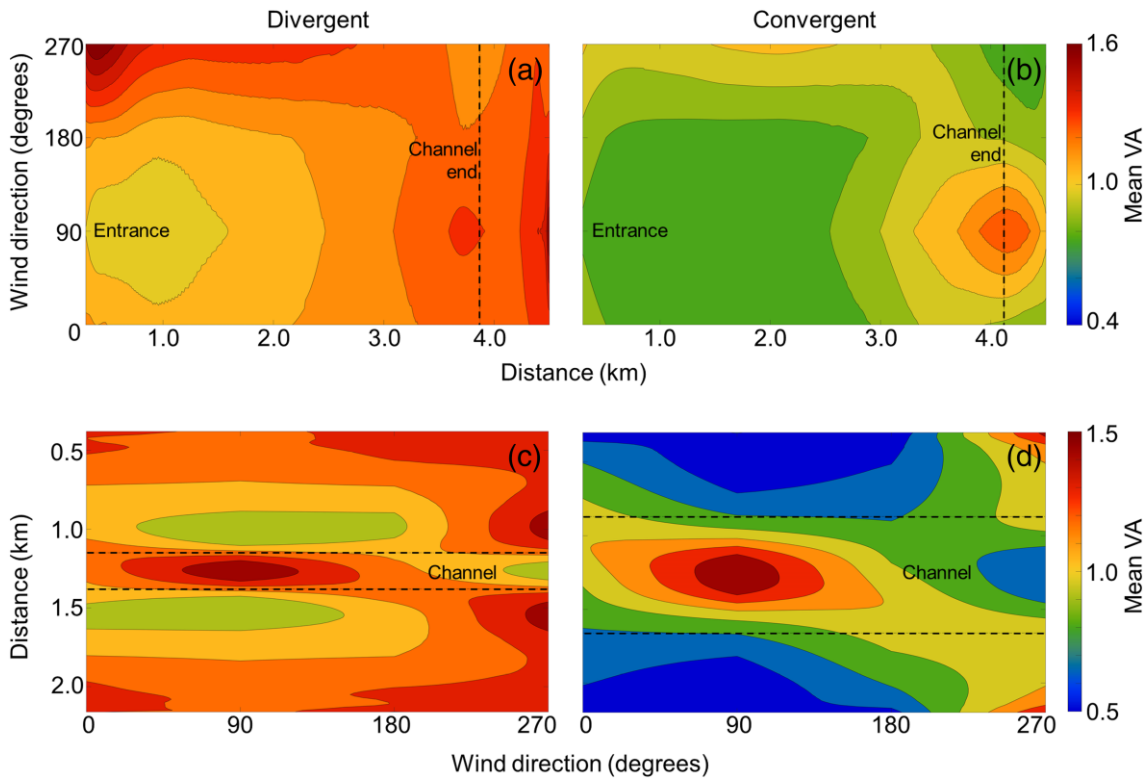
Figure 3.11: Contour plots of mean velocity asymmetry for cases with tides and wind forcing combined, averaged over cross-sections perpendicular to (Y-direction: A, b) and parallel with (X-direction: C, d) inside the divergent (a, c) and convergent (b, d) basins based on moderate (6 m/s) winds from four different directions. Dotted lines indicate the upper (a, b) and cross-basin (c, d) limits of the tidal channels.

In order to summarize the influence of wind forcing on horizontal velocity patterns in shallow coastal systems with specific morphological characteristics, the zero moments for velocity asymmetry in X and Y directions were determined throughout both idealised basins. This analysis focuses on wind direction in particular, the main driver of VA change in shallow tidal basins. The zero moments are extracted from mean VA for cross-sections taken parallel with (X-direction) and perpendicular to (Y-direction) the tidal channel. The mean VA results for tides and wind forcing combined (similar to Figures 3.4 and 3.5) are summarized in Figure 3.11 for 12-hour moderate (6 m/s) wind events, highlighting the overall pattern of greater flood dominance (mean VA > 1.0; orange to red colours) inside the divergent basin (Figures 3.11a and 3.11c), compared to the more ebb-dominant (mean VA < 1.0; green to blue colours) convergent basin (Figures 3.11b and 3.11d).

62

The velocity asymmetry patterns, based on VA averaged over cross-sections perpendicular to the channel (Y-direction), illustrate how mean VA varies throughout the basins, from the basin entrance (left-hand side of Figures 3.11a and 3.11b) to the upper basin (right-hand side of Figures 3.11a and 3.11b). These VA patterns confirm that tidal forcing combined with along-channel winds (90º and 270º, on y-axes of figures) cause greatest VA variation in both basins. The upper regions of the basins (right-hand side of Figures 3.11a and 3.11b) are shown to be overall more flood-dominant than the lower basins for all wind directions, except for landward winds (270º). When the asymmetry patterns for wind forcing only are considered ($VA_{tw} - VA_t$), similar to the results shown in Figures 3.6 and 3.7, the results illustrate that wind forcing produces a divergent basin that is overall slightly more ebb-dominant (negative VA in Figure 3.12a). Patterns of velocity asymmetry in the convergent basin (Figure 3.12b) are comparable to the divergent basin, albeit with a generally greater variation in absolute VA.
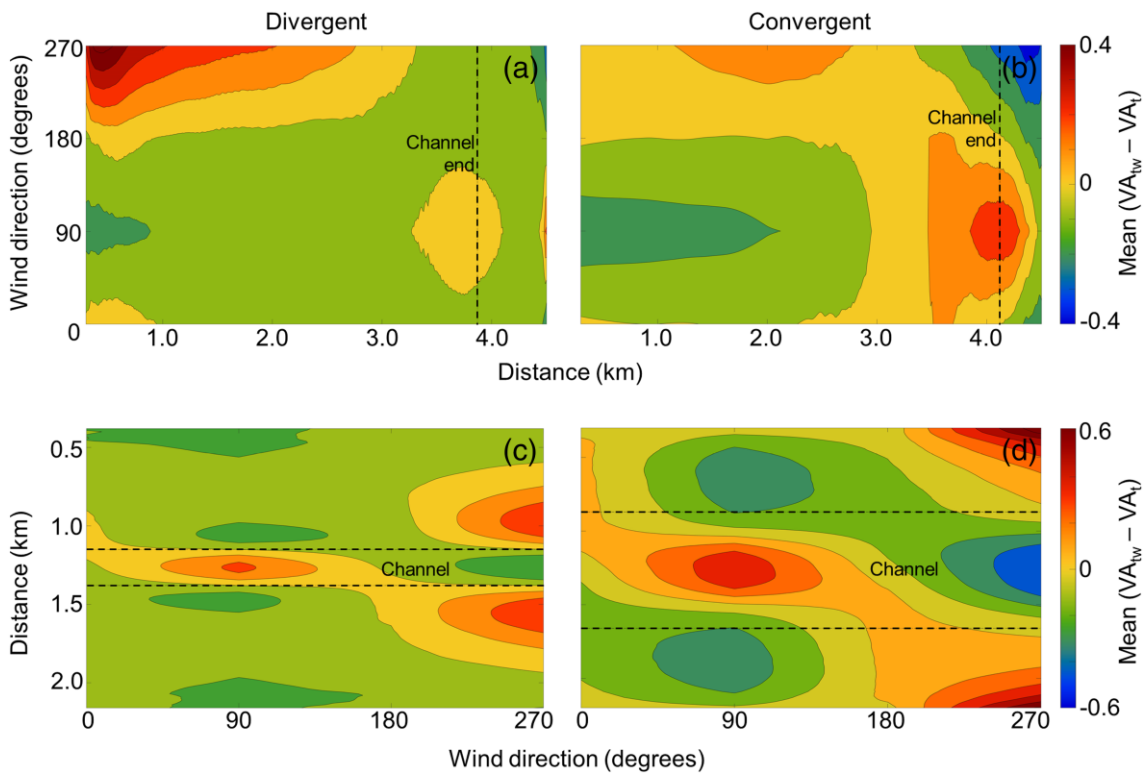
Figure 3.12: Contour plots of mean differences in velocity asymmetry ($VA_{tw} - VA_t$) for wind forcing only, averaged over cross-sections perpendicular to (Y-direction: A, b) and parallel with (X-direction: C, d) inside the divergent (a, c) and convergent (b, d) basins based on moderate (6 m/s) winds from four different directions. Dotted lines indicate the upper (a, b) and cross-basin (c, d) limits of the tidal channels. Yellow colours (VA ≈ 0) represent areas of no significant mean wind effects.

Velocity asymmetry averaged over cross-sections parallel to the channel (X-direction), summarizes how mean VA varies between shallower (intertidal) and deeper (subtidal) sections inside both basins. Flood dominance is prevalent in the subtidal channel of both

basins (area between dotted lines in Figures 3.11c, d and 3.12c, d), except for landward winds (270º). The transition zones between subtidal and intertidal regions (directly north and south of the channels) are more ebb-dominant, whereas the more elevated shallow intertidal regions (around 0.5 and 2.0 km on y-axis for the divergent basin in Figures 3.11c and 3.12c) may again become less ebb dominant. As the intertidal regions of the convergent basin (Figures 3.11d and 3.12d) are less-well defined than the divergent intertidal regions, average water depths in these sections of the convergent basin are comparable to the water depths in the transition zones of the divergent basin (green areas north and south of the channel Figure 3.11c). Consequently, the spatial distribution of positive (flood dominance) and negative (ebb dominance) VA with depth in Figure 3.12d (convergent basin) is essentially the same as in Figure 3.12c (divergent basin), albeit more exaggerated in the Y-direction. This across-basin amplification of the VA patterns is a result of the across-basin hypsometric differences in the shape of the intertidal profile between both basins, and highlights the dependency of velocity asymmetry on local basin depth.

Our study results show that wind-induced variations in velocity asymmetry are largest for channel-parallel winds in the idealised convergent basin. The less-infilled bathymetry of this basin is submerged for longer periods than the infilled divergent basin, and wind can therefore affect hydrodynamics over a longer period. These results are consistent with patterns of wind-induced residual velocities deduced from model results for both idealised basins in our study. The relationship between wind speed and residual velocity (not shown) was found to be roughly linear in the shallow intertidal regions as well as in the deeper tidal channels of the basins, with wind-induced increase of residual velocities slightly greater in the convergent basin. Field measurements of current velocities by Narvaez and Valle-Levinson (2008) suggest that during channel-parallel seaward winds, the transverse flow patterns found in our model results may occur only during periods of strong winds. Flow circulation patterns as a result of seaward wind forcing are especially dependant on geometry as, in these conditions, the intensity of upwind-directed currents in the tidal channel is modulated by the width of the downwind-situated basin entrance. Analysis of the first moments (variance) of velocity asymmetry in X and Y directions throughout both basins (not shown), suggests that variance in VA is greatest in basin sections where wind-induced VA changes are most extreme.

Wind-induced circulation can affect hydrodynamics in other aquatic environments similarly, such as in enclosed basins and lakes, often generating strong nearshore currents

that can develop soon after the application of wind shear on a lake surface. Observations of such downwind-directed currents in shallow lake regions were shown for an idealized long narrow lake by Csanady (1973) whose study indicated that the wind-generated surface currents may be accompanied by a weak return flow, depending on the local lake depth. Hung and Li (2019) showed that circulation patterns and velocity magnitude in the interior of Lake Pontchartrain are also dominated by local winds. However, remote wind effects were shown to be responsible for the inflow or outflow through inlets, controlling the magnitude of the current velocity in regions close to an open boundary. Spatially varying wind forcing may also produce large-scale cyclonic gyres in lakes, as shown by Laval et al. (2005). They found that the horizontal distribution of wind fields in the Lake Maracaibo region drives a mean, cyclonic, surface-layer circulation, affecting the mixing between the surface layer and the bottom layer of the lake.

3.4.2 Implications for Sediment Transport

Wind-generated currents and associated shear stresses can substantially affect peak and residual flow patterns and velocity distortion in shallow tidal basins, as indicated by our results, and may consequently be an important amplifier of sediment transport rates. In order to assess the potential effectiveness of velocity asymmetry as a predictor of sediment transport potential inside tidal basins, tide-averaged rates of sediment transport (S) inside the basins were calculated for a number of wind conditions using the Engelund-Hansen (1967) method. This relatively simple method is commonly used to calculate fluvial and coastal sediment transport rates on the basis of a single median grainsize (e.g. Gerritsen et al., 2003). A grainsize of 150 μm was assumed for this exploratory sediment transport analysis, representing the approximate mean grainsize inside Tauranga Harbour. An example of the comparison between velocity asymmetry and tide-averaged sediment transport for moderate channel-parallel winds is shown in Figure 3.13. Results of the analysis indicate that in the centre of the divergent and convergent basin, where the average basin depth exceeds ~0.3 m, largest sediment transport rates induced by wind forcing generally occur near or within regions of greatest VA change, as also shown in Figure 3.13. This apparent link between VA and sediment transport suggests that velocity asymmetry may be an effective indicator of wind-induced sediment transport in basin sections where water depth is sufficient. The correlation between sediment transport rates and VA near the basin entrances, and, more prominently, in the shallower upper sections of the divergent basin is less straightforward. Sediment transport in these upper intertidal regions is limited due to decreasing water depths and associated slower flow speeds.

Wind-induced VA changes, however, are less affected by the shallow water depth in in the upper basin sections (see for example the right side of Figure 3.6d and 3.7d), suggesting that even though absolute current velocities are small in these regions, the relative differences between ebb- and flood-directed velocities can remain large. Consequently, rates of VA change may not adequately reflect sediment transport potential in the shallowest parts of intertidal basin regions. Our sediment transport analysis is exploratory; a comprehensive sediment transport modelling study may resolve the links between wind-induced transport potential and VA in the shallow regions of tidal basins in more detail. Such an extensive analysis is beyond the scope of our current study.
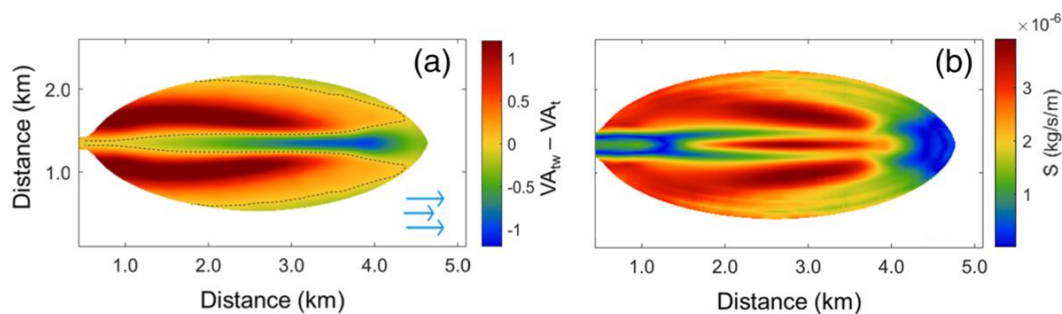
Figure 3.13: Comparison between velocity asymmetry (a; same as Figure 3.8b) and tide-averaged sediment transport (b) inside the divergent basin, for winds speeds of 6 m/s and wind duration of 12 hours.

As our study shows, the impact of individual meteorological events on hydrodynamics and associated sediment transport potential within specific tidal basin geometries depends on the characteristics of these events. Previous studies have indicated that there can be major differences in the direction of net sediment transport between calm and windy weather (e.g. Dyer et al, 1999, Lettmann et al, 2009). Christiansen et al. (2006) found that asymmetries in horizontal flow velocity caused by winds of 4-12 m/s dominated sediment fluxes on a tidal flat in the Wadden Sea. Turbidity plumes resulting from high-intensity wind events in the western arm of Lake Superior were shown by McKinney et al. (2019) to potentially represent a significant cross-shelf transport mechanism for sediments and nutrients. Our model results suggest that changes in the rate of sediment transport in shallow basins as a result of wind-generated currents may be most substantial for along-channel moderate to strong winds (6 to 12 m/s). Consequently, wind-induced sediment transport in shallow tidal basins will primarily take place during more energetic meteorological events, as also observed in studies of similar intertidal and subtidal regions (e.g., Green et al., 1997; Van der Werf et al., 2015). We show that wind speed can modulate the location of maximum velocity asymmetry change inside a basin, which

may coincide with a region of substantial sediment transport potential, provided local water depths are sufficient.

Strong wind events are likely fundamental for the morphological evolution of the tidal basin classes included in our study. Therefore, local wind climate characteristics can provide insight into the long-term morphological evolution of a shallow tidal basin. Wind events with speeds and durations capable of altering flow directions and velocity asymmetry signals are fairly common for the Tauranga Harbour region (see Figure 3.1b). Hence, it is likely that wind-induced currents modulate velocity asymmetry patterns and associated morphological changes in the six shallow tidal basins that form the motivation for our study (see also De Ruiter et al., 2019). As these six basins vary in orientation relative to prevailing wind directions, specific wind events are expected to result in different velocity asymmetry and sediment transport potential changes inside the individual basins. In general, sediment flux patterns leading to either infilling or erosion in shallow tidal basins are likely to depend on a combination of tidal range, strength and seasonality of the local wind climate, and the orientation of the basin morphology relative to the prevailing wind direction.

In addition to inducing wind-driven currents, wind events can also generate wave-driven flow. Wave-related bottom erosion can modulate hydrodynamics, sediment dynamics and morphological changes of subtidal and intertidal flat surfaces in regions where fetch is sufficiently large (e.g. D'Alpaos et al., 2013; Hunt et al., 2016). Previous studies have indicated that, contrary to wind-induced currents, wind waves do not significantly affect horizontal velocity changes (e.g. De Vet, 2018). Instead, waves mainly affect slack tide duration asymmetry (SDA), by modifying the duration for which the bed shear stress is below the critical shear stress in shallow intertidal areas at high tide slack water (e.g. Zhou et al., 2015). Given the relatively small dimensions of the tidal basins considered in our research, fetch in these basins is likely not sufficient to generate wind waves large enough to substantially affect circulation and sediment transport potential inside the basins (e.g. Hunt et al., 2015). Consequently, we have excluded the effects of waves on tidal basin hydrodynamics in this study.

3.4.3 Model Limitations

The results from the two idealised tidal basin models have enabled us to highlight the influence of wind-generated currents on velocity asymmetry patterns. With the assumption of a fixed basin morphology, as used in our experiments, the focus is on the

hydrodynamics rather than on whether realistic morphologies are being produced by the assumptions used in the morphological models (Coco et al., 2013). The modelled downwind flows over the intertidal flats and upwind flows in the channels are in line with fundamental principles of wind-driven flow in closed or partially closed basins, which state that, in shallow water, the dominant force balance is between surface wind stresses and bottom friction (Alekseenko et al., 2013). In the shallow areas adjacent to the tidal channel, the acceleration from wind forcing increases the current velocities in the same direction as the wind, raising the water level downwind and forming a pressure gradient. This pressure gradient returns water against the wind down the channel resulting in a flow that opposes the wind (e.g. Hunt et al., 2015). The transverse flow patterns found in our model results illustrate good agreement with observational evidence of wind-driven flow in previous studies (e.g. Juarez et al., 2019). Exploratory model runs with increased vertical model resolution (ten sigma layers) produced wind-induced velocity asymmetry and residual current patterns that are virtually identical to the results described in our study, signifying that vertical model resolution does not impact hydrodynamics in the idealised basins. Across-channel winds may produce temporary flow patterns that are relatively two-dimensional, especially in upper intertidal regions of the divergent basin, potentially complicating the interpretation of local velocity asymmetry directions. However, these flow patterns were found to not substantially alter velocity asymmetry signals over a tidal cycle. Velocity asymmetry at the entrance of the basins was assumed to be negligible, hence excluding the potential effects of external asymmetrical tidal signals (Ridderinkhof et al., 2014) on velocity asymmetry inside the basins.

Our current models represent simplified interpretations of two divergent shallow tidal basin systems with parameters derived from depth-averaged values. In order to isolate the effects of wind events on basin hydrodynamics, detailed sediment transport processes and associated morphological changes as a result of the combination of tide and wind forcing have been excluded. Additionally, as also shown in our previous work, basin geometry and hypsometry can have a strong impact on the magnitude and direction of basin velocity asymmetry and sediment transport potential (De Ruiter et al., 2019). In shallow tidal basins turbulent mixing by wind forcing penetrates to the bottom, causing a unidirectional flow and minimum stress differential (Weisberg & Zheng, 2006). In deeper tide-dominated systems, bidirectional exchange flows and an increased stress differential may develop, with downwind-directed surface currents and upwind-directed near-bottom currents (e.g. Wong and Valle-Levinson, 2002; Ponte et al., 2012; Alekseenko and Roux,

2019). Since the area of deep water may be less than the area of shallow water, such deeper return currents can concentrate over a narrower cross-section, potentially resulting in flow speeds that are greater at depth than at the surface (Weisberg & Zheng, 2006). Evidence of near-bottom return currents was found in the bottom sigma layer of the tidal channel sections in our idealized basins for strong wind conditions (> 10 m/s); however, owing to the limited depth of the channels, these return flow velocities are very small and consequently peak ebb and flood velocity ratios are not affected (VA). The shallowness of the tidal basin geometries considered in our studies allows for the prevalence of flows produced by wind stress. A comparison of depth-averaged and near-bed-only velocity asymmetry inside the idealised basins (not shown) revealed similar overall VA signals, with VA being somewhat more extreme for near-bed flows, especially during strong wind conditions. Velocity asymmetry patterns in deeper, larger tidal basins may be less affected by meteorological forcing. In our current study we have not explored the morphological parameter space to be able to speculate on the basin depth and length criterion beyond which our results may no longer apply. Additionally, the inclusion of detailed sediment transport processes in the idealised model simulations is beyond the scope of this study. Consequently, simulating wind-modulated hydrodynamics and sediment transport patterns in tidal basins with a larger range of geometries and hypsometries would further enhance our understanding of the links between tidal basin size and shape, rates of basin infilling and the effects of meteorological forcing.

3.4.4 Future Meteorological Changes

Our model results clearly demonstrate that the intensity, direction, duration and relative phasing of wind events determine whether horizontal velocity patterns inside shallow tidal basins are substantially affected by wind. Similar results have been found in studies of other shallow intertidal regions (e.g. Talke and Stacey, 2008). During strong wind conditions, tidally induced currents can be small compared to wind-induced flows (Li, 2013), especially in shallow areas encompassing tidal channels aligned with the main wind direction. Previous studies have shown that wind events are often likely to occur over only a portion of the tide (e.g. Talke and Stacey, 2009). Our results indicate that the timing of a wind event with respect to the stage of the tide can have strong effects on associated changes in hydrodynamics, especially for wind events with a shorter duration (3 to 6 hours). The meteorological forcing considered in our modelling study is a simplified representation of natural wind events. Wind events included in our models are instantaneously activated and stopped. Sensitivity analysis shows that velocity

asymmetry patterns obtained from these simulations are nearly identical to model results based on gradually increasing and decreasing wind forcing. We also assume that wind speed and duration do not substantially change within one modelled event. Even though such relatively stable local wind events can be fairly common, as shown by our analysis of the Tauranga Harbour wind climate (see Figure 3.1b), more variable wind events may be more realistic in other regions.

Depending on the location, local wind event parameters can vary on both small (e.g. tidal cycles) and larger (e.g. spring-neap cycles or seasonal) timescales. As such, accurately predicting future wind characteristics may prove challenging, especially considering the uncertain effects of anthropogenically induced climate change. Long-term changes in local wind climate could disrupt hydrodynamic processes and associated morphological stability within tidal basins. These long-term effects of wind-climate may lead to a net increase or decrease of intertidal area extent, depending on local wind direction and basin geometry, morphology, and orientation. Such morphological changes may lead to variations in velocity asymmetry patterns and a change of the fetch within a tidal basin, affecting potential sediment transport directions. A dynamic equilibrium may be reached, based on the dominant wind direction. Consequently, the long-term effects of wind climate are complicated by feedback mechanisms. As the future pathways of tidal basin morphological evolution depend on a combination of relatively easily predicted tidal forcing and more uncertain meteorological conditions, it is crucial to be able to adequately define meteorological forcing mechanisms when studying shallow tidal basins or similar intertidal and subtidal coastal systems.

3.5 Conclusions

Meteorological processes can modulate hydrodynamics and associated sediment transport in coastal regions. Our study indicates that wind-driven currents are critical drivers of velocity asymmetry change in shallow tidal basins. Wind forcing was found to mainly influence peak- and residual flow velocities, with a minimal impact on tidal harmonics. The impact of wind forcing on horizontal velocity asymmetry depends on wind attributes, tidal basin geometry, local water depth and the characteristics of the underlying tide-induced currents. Model results demonstrate that in shallow intertidal basin regions, wind-generated currents aligned with the wind direction modulate velocity patterns, resulting in an associated downwind-directed increase in velocity asymmetry. Deeper subtidal channels are characterised by currents opposing the wind direction, promoting velocity patterns that can contrast with the intertidal velocity asymmetry. This

depth-dependent modulation of velocity asymmetry is most evident for wind directions parallel to the main axes of the tidal channel. An increase in wind speed promotes more extreme velocity asymmetry ratios, especially in a convergent less-infilled basin, without substantially changing the larger-scale velocity asymmetry patterns. Additionally, we show that timing and duration of a wind event affects resulting velocity patterns. Wind events coinciding with flooding tide cause the most noteworthy differences between peak flood- and ebb dominance, especially for wind events lasting six hours or less. Our study highlights that hydrodynamic and sediment transport processes in shallow tidal basins are controlled by both tidal forcing and wind event driven mechanisms. The influence of wind over a tidal cycle can produce the velocity asymmetries necessary for sediment transport at relatively short timescales. Consequently, the ability to predict future pathways of morphological change in tidal basins relies on meteorological conditions as well as well-defined local tidal regimes as well as meteorological conditions.

Chapter 4

Relationships between Sediment Connectivity and Hypsometry in a Shallow Estuary

View of the northern part of Tauranga Harbour, near Bowentown

Contribution of Authors

Chapter 4 presents the article entitled "Relationships between sediment connectivity and hypsometry in a shallow estuary", which will be submitted to *Geomorphology* for review. I modified the numerical model for Tauranga Harbour using Delft3D and wrote MATLAB scripts to process and analyse the model data. I prepared all the figures for the article and wrote the initial and subsequent drafts of the manuscript. Julia C. Mullarney, Karin R. Bryan, and Christian Winter provided valuable comments and discussions. Additionally, my co-author Julia C. Mullarney edited the draft of the article.

4.1 Introduction

Estuaries and tidal basins are dynamic geomorphic systems that serve as a junction between land and sea, providing the main path for terrestrial sediments to enter the ocean (Yu et al., 2021). These coastal environments are shaped by non-linear interactions between tidal forces, meteorological conditions, and morphological changes. Sediment transport pathways in estuaries are often dynamic, and can be further influenced by anthropogenic controls and climate change related processes (e.g. Bishop et al., 2017). For example, rising sea levels are causing a trifecta of impacts throughout estuarine regions, leading to increasingly frequent flooding, coastal erosion and the potential for more frequent and permanent inundation. Human interventions such as protective structures, basin adaptations, or dredging activities can also affect estuarine sediment transport patterns by altering transport pathways (e.g. Elias et al., 2013; Luijendijk et al., 2017; Wang et al., 2018). Variations in sediment transport patterns can have a profound effect on the morphological evolution of estuarine sub- and intertidal regions, which may lead to potential for further coastal flooding and erosion. Additionally, disruptions in sediment transport pathways may result in ecological degradation and socioeconomic issues (Roelvink, 2015). Efficient management of sediments in estuaries and tidal basins under specific environmental conditions is vital for sustainable protection against flooding, erosion, and ecosystem disturbance. Consequently, developing an improved understanding of the complexities of estuarine sediment pathways is critical.

Connectivity can be used as a general framework for representing the strength of connections and flows between the different parts of a coastal system (Pearson et al., 2020). This framework may be considered as being part of the concept of sediment routing. Sediment routing systems (SRS) link the fate of sediments from their formation to their final source, based on denudation of sediment sources, sediment transport, and deposition (e.g. Allen, 2017). The connectivity framework has been adopted within ecological and physical oceanography studies for analysis of marine reserve design (e.g. Rossi et al., 2014), larval dispersal (e.g. White et al., 2019) and microplastic dispersion (van Sebille et al., 2019). Connectivity Recent studies have shown that connectivity can also be a useful framework for analysing both the flow directions and geomorphic coupling between neighbouring sub-regions, as well as the system-wide sediment transport pathways and connections in coastal environments (e.g. Pearson et al., 2020; Hiatt et al., 2021; and Yu et al., 2021). Structural connectivity refers to the spatial anatomy of a coastal system, by describing how units within the system are spatially

arranged relative to one another. Functional connectivity (sometimes referred to as dynamic connectivity, e.g. Hiatt et al., 2021) relates to the dynamic fluxes that exist within a coastal system, describing how much material passes through and between different regions, and highlighting dominant transport pathways (Pearson et al., 2020). Consequently, connectivity is not synonymous with patterns of sediment deposition and erosion. Numerical models can provide a convenient way of exploring sediment connectivity, as they can be used to calculate sediment concentrations and transport rates at every point within a coastal system (Wohl at al, 2019). This data can be used to assess the fate of sediments as they move between the different morphological units. The large and potentially complex dataset of sediment transport patterns produced by numerical models can be reduced to a relatively simple form, by applying the graph theory (Newman, 2003; Phillips et al., 2015), and developing connectivity matrices. Additional connectivity metrics can be calculated from these matrices, which can provide useful insights into the present state of the system. System-level connectivity metrics, such as the link density, describe the overall amount of connectivity within a given coastal region (Phillips et al., 2015). On a smaller scale, two cells inside a coastal system are functionally connected if there is a flux between them. Sediment exchange between adjacent cells is most common, but remote spatial connections may also exist (Pearson et al., 2020). In general, larger amounts of sediment exchange between specific cells suggest a close link in terms of topology of the coastal system, irrespective of actual distance between the two regions. The sum of all transport in and out of a given cell is defined as the cell strength. If in-strength is greater (smaller) than out-strength, a cell may be characterised as a sink (source). Connectivity patterns attributed to a specific sediment grainsize may be modulated (in a non-linear manner) by the grainsize mobility threshold and the energy available to transport the sediment in shallow tidal systems. However, the links between hydrodynamic energy, grainsize characteristics, and sediment connectivity have not yet been fully explored in previous modelling studies of shallow tidal systems.

In order to develop a thorough understanding of sediment transport patterns, the location of sediment sources and sinks, and the morphological changes within an estuarine system, sediment connectivity should be considered alongside other physical processes that shape these environments. In this study, we use graph theory to explore the functional sediment connectivity of a shallow estuary (Tauranga Harbour) and its associated sub-basins. Graph theory can provide a strong mathematical framework for analysing geomorphic systems and quantifying sediment connectivity patterns. This method is based on

techniques developed within network science, where a complex system is conceptualized as a series of nodes and links between nodes, referred to as a "graph" (Newman, 2003; Phillips et al., 2015). Since the application of graph theory and connectivity metrics to estuarine sediment dynamics is a relatively novel approach, the links between sediment connectivity and for example flow velocity asymmetry, meteorological forcing, and the effects of local sub- and intertidal geometry, remain relatively unexplored. Two prior numerical modelling studies carried out for Tauranga Harbour highlight the complex links between estuarine and tidal basin geometry and morphology, velocity asymmetry, and meteorological forcing (De Ruiter et al., 2019; De Ruiter et al., 2021). In these studies, hypsometric curves were determined for the microtidal sub-basins in Tauranga Harbour. Hypsometry exponents (γ) were used to describe the shape of the basin intertidal profiles, with convex hypsometric profiles ($\gamma \approx 2$) corresponding to infilled environments and more concave profiles ($\gamma \approx 4$) corresponding to less infilling. Basin dilation factors (BDF), developed in the aforementioned studies, served as a useful metric to clearly characterise the geometry of the sub-basins, with greater (smaller) BDF values indicating a more divergent (convergent) basin (de Ruiter et al., 2019). The results of these studies indicate that basin geometry and intertidal hypsometry, combined with wind forcing, modulate velocity asymmetry within tidal sub-basins. Shallow divergent basins (width increases landward) were found to generally be accretionary environments (convex hypsometry), whereas convergent basins were shown to be markedly less infilled.

Here, we extend these previous works, by analysing sediment connectivity and transport patterns between different geomorphic regions within Tauranga Harbour estuary, with a focus on the microtidal sub-basins. We resolve connectivity metrics for different grainsize classes within the estuary, and determine which estuary regions can be described as sediment sources and sinks. Our study indicates that sediment connectivity can be an effective framework for exploring the present and future interplay between hydrodynamics, sediment transport pathways, and morphology and geometry in shallow, tidally-dominated estuarine systems.

4.2 Study Area and Methods

Tauranga Harbour estuary is a shallow barrier-enclosed estuary located on the east coast of New Zealand's North Island (Figure 4.1a). The estuary consists of a northern and a southern basin, separated by an extensive area of tidal flats (Figure 4.1b). Semi-diurnal tides modulate hydrodynamics in the estuary, ranging from 1.62m at spring tide to 1.24m

at neap tide conditions (Heath, 1985). Previous sediment modelling studies have focused on general sediment transport patterns in the southern part of the estuary only (e.g. Ellis et al., 2013), but exclude a detailed analysis of sediment connectivity. For the northern part of the estuary, no extensive sediment transport information is available, except for scarce and short-term (~2015-2021) sediment accumulation data from sediment plates, supplied by the Bay of Plenty Regional Council (BoPRC). Based on recent data from BoPRC sediment plates, the average grainsize of sediments in Tauranga Harbour is roughly 125-200 μm, corresponding to fine sand. A number of small microtidal basins with varying geometry (planform shape) and intertidal hypsometry are located on the south-western side of the main estuary, sheltered from the open ocean. These basins range from flood-dominant divergent and infilled environments, to convergent, ebb-dominant and less-infilled areas. The divergent basins (BDF > 4) are characterised by convex-shaped hypsometric profiles ($\gamma \approx 2$), whereas the convergent basin (BDF $\approx$ 1) profiles are more concave ($\gamma \approx 4$).

In order to apply the concept of sediment connectivity in Tauranga Harbour, twenty geomorphic cells ($n = 20$) were defined within the estuary, broadly separated into sub-basins and areas with different morphological characteristics (noting the divisions in particular within the main basins are somewhat subjective). Consequently, the estuary is divided into tidal channel regions, intertidal flats, and sub-basins (Figure 4.1b).

To analyse sediment connectivity patterns inside Tauranga Harbour, we applied numerical modelling using Delft3D-FLOW (Lesser et al., 2004). The Delft3D sediment transport module has been widely used for simulating sediment transport in coastal systems (e.g. De Elias et al., 2006; Herrling & Winter, 2014). An existing two-dimensional, depth-integrated Delft3D model of Tauranga Harbour, developed and validated by de Ruiter et. al (2019), was used as a basis for our study. This model is comprised of two domains; one covering the main estuary and its sub-basins (grid resolution 25 m by 25 m), the other representing an offshore region north-eastward of the main estuary (grid resolution coarsening in offshore direction). Tidal forcing in the existing model was simplified to conserve computational time, by applying an M_2 astronomic tidal signal imposed at the shore-parallel seaward boundary of the outer model domain (Figure 3.1c). Neumann boundaries, representing water level gradients, were applied at both shore-perpendicular seaward boundaries. representing very fine to medium sand. The model is based on a spatially varying bottom roughness, with Manning coefficient values between 0.02 and 0.1 s/m$^{1/3}$ based on varying bathymetry elevations.
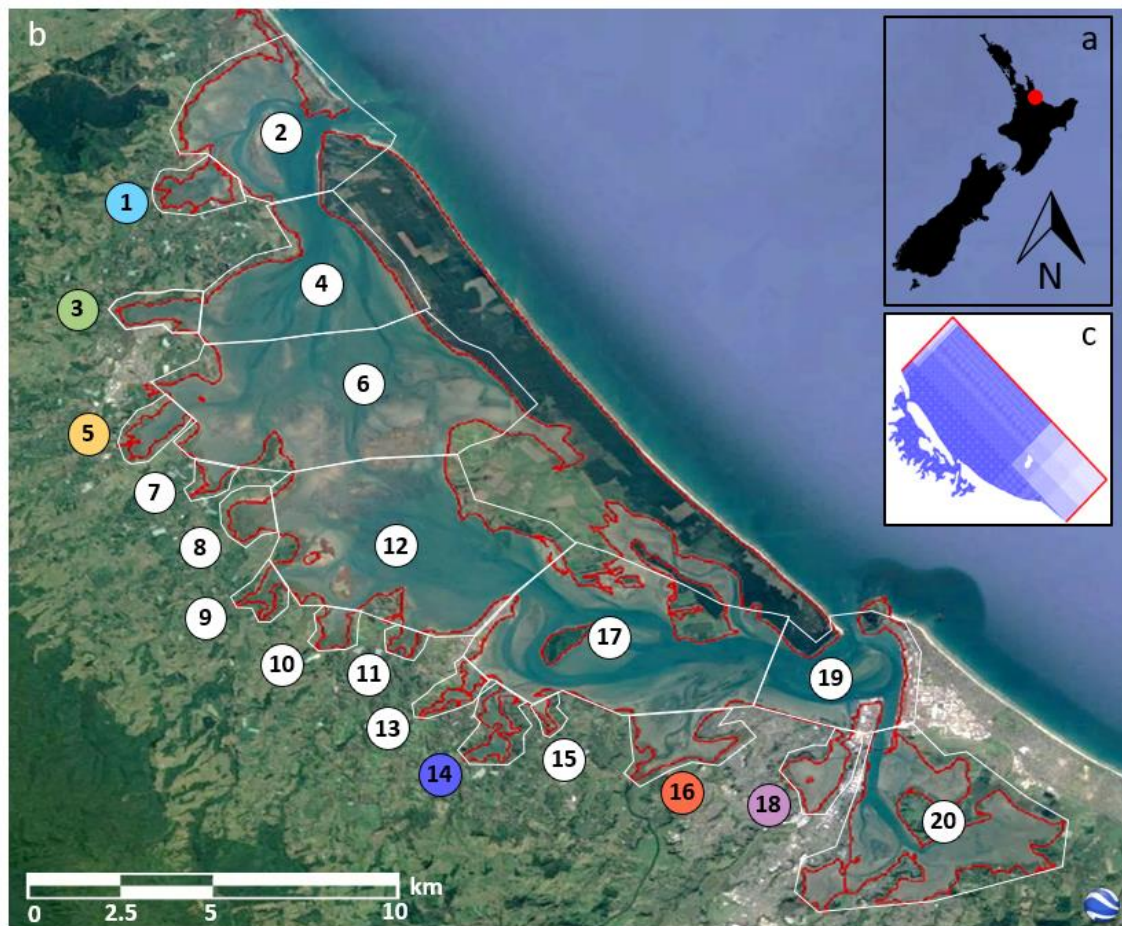
Figure 4.1: Overview of Tauranga Harbour, with location in New Zealand depicted by red dot (a). Twenty geomorphic cells were defined within the estuary (indicated by numbers in b). Coloured numbers represent the six convergent and divergent sub-basins which we focus on during the analysis (see Section 4.4). The Delft3D model grid is shown in (c), with model boundaries in red.

In order to explore sediment connectivity patterns for varying grainsizes, five non-cohesive sediment classes were chosen (50, 125, 200, 275, and 350 μm), with a specified density of 2,650 kg/m^3, and 1,650 kg/m^3 dry bed density. These sediment classes represent very fine to medium sand. The Van Rijn (1993) sediment transport formulation for bedload and suspended load was used in the model simulations (Deltares, 2014). To limit computational loads, initial model simulations were carried out for each of the five grainsize classes separately, using the existing bathymetry of Tauranga Harbour (de Ruiter et al., 2019). The aim of these five simulations was to update the morphology and redistribute the sediments in order to develop a dynamic equilibrium bathymetry for each grainsize. To reduce computational loads further, morphological evolution in the simulations was accelerated using the Delft3D Morphological Acceleration Factor, or MORFAC (Roelvink, 2006; Lesser et al., 2004). A MORFAC value of 100 was applied to simulate morphological changes, with model results suggesting that 25 model days (~5000 tidal cycles) were sufficient to reach an equilibrium bathymetry for all five

grainsize classes. An initial sediment layer thickness of 5 m was found to be sufficient to account for the morphological changes simulated during the five initial model simulations. An overview of the main model parameters is given in Table 4.1.

Table 4.1: Overview of model parameters

Parameter	Value
Grid size	25 x 25 m[a]
Time step	0.1 min
Simulation time	25 days[b] / 5 days[c]
Bed layer thickness	5 m[b] / 2 m[c]
Grainsize (non-cohesive)	50, 125, 200, 275, 350 μm
Reference density for hindered settling	1,600 kg/m^3
Specific density	2,650 kg/m^3
Dry bed density	1,650 kg/m^3
MORFAC	100

[a] Grid size for the main estuary; grid resolution coarsens in offshore direction
[b] Values represent the five initial model simulations
[c] Values represent the ten connectivity model simulations

Owing to the large model domain and the inclusion of sediment transport, the duration of the model simulations, implemented using the NeSI (New Zealand eScience Infrastructure) high performance computing system, was substantial. Consequently, the simulations were conducted in increments of 5 model days, with each final 5-day model bathymetry and associated hydrodynamic state being used as initial conditions for the following 5-day simulation. As such, each full model simulations took roughly two months. Figure 4.2 shows the initial model bathymetry (Figure 4.2a) alongside an example of the resulting bathymetry for the finest sediment grainsize used in the simulations (50 μm; Figure 4.2b). The figure highlights that the most significant morphological changes (> 1 m erosion) occurred in the main tidal channels of the northern and southern basins (dark blue areas). Morphological changes in the intertidal regions of the main estuary and in the smaller sub-basins are relatively small (< 0.5 m, yellow and orange areas). As expected, morphological changes (rates of erosion and sedimentation) increase with decreasing grainsize.
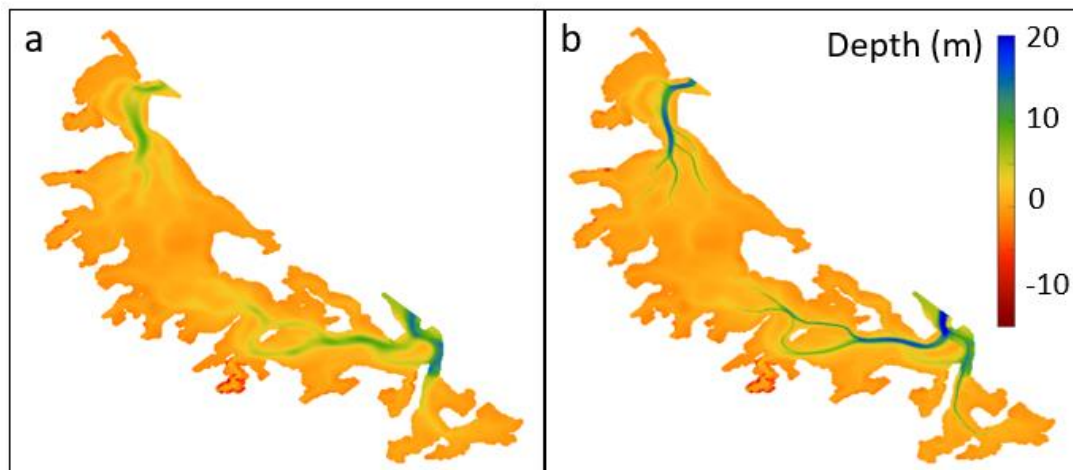
Figure 4.2: Original model bathymetry for Tauranga Harbour (a), shown alongside an example of the bathymetry (b) generated by the initial model simulation with the finest modelled grainsize (50 μm). This equilibrium bathymetry was subsequently used as the starting bathymetry for the connectivity simulations.

In order to explore the spatial variability in sediment connectivity for the different grainsize classes, an additional set of ten model runs was carried out. A hydrodynamic spin-up period of five tidal cycles was discarded at the beginning of the simulation. Each of these simulations, representing sediment transport in dynamic equilibrium conditions spanning four tidal cycles (excluding model spin-up time), was based on a distinct base grainsize (50, 125, 200, 275, or 350 μm). Within the simulations (see Table 4.1 for details), each of the twenty geomorphic cells in Tauranga Harbour was assigned a grainsize value that was very slightly different from the grainsize in the other cells. As an example, for a model run with a base grainsize of 200 μm, the first geomorphic cell was assigned a grainsize of 200.01 μm, the second cell was assigned 200.02 μm, etc. By applying this methodology, we were able to track the sediment originating in each geomorphic cell clearly, whilst preserving an overall grainsize of 200 μm.

Five of the ten model simulations were conducted using the updated equilibrium bathymetries generated during the five initial model runs as described earlier, with the relevant grainsize class used as input (Table 4.1). In order to analyse whether bathymetry changes affect sediment connectivity patterns, the method of geomorphic cell grainsize variation was also applied to five model runs utilising the original Tauranga Harbour bathymetry as a basis (Table 4.1). An initial sediment layer thickness of 2 m was set for all ten model simulations.

Table 4.2: Overview of the connectivity model runs.

Run number	Bathymetry	Grainsize (μm)
1-5	Equilibrium[a]	50, 125, 200, 275, 350
6-10	Original	50, 125, 200, 275, 350

[a] Each grainsize class is characterised by a unique equilibrium bathymetry (five in total)

4.3 Results

In order to assess sediment connectivity between the different geomorphic regions in Tauranga Harbour, modelled sediment concentrations were analysed throughout the estuary. The sediment exchange between each geomorphic cell was deduced from the model results produced by the ten simulations described above. The slight difference in grainsize between all geomorphic cells in each model run allowed us to determine the source of all sediments entering and exiting a specific cell. Sediment mass loads for each model grid cell (M_{tide_gc}; kg) were determined from the model results for each sediment fraction using:

$$M_{gc} = \int_0^T C(t)V(t)dt \qquad (4.1)$$

where C is the sediment concentration (kg/m^3), and V is the grid cell volume (m^3). Figure 4.3 shows an example of the dispersion of sediment originating in Tuapiro basin (cell 1), illustrated by the sediment mass loads, showing grid cells through which sediment passed for the five grainsize classes (Figures 4.3a to 4.3e).
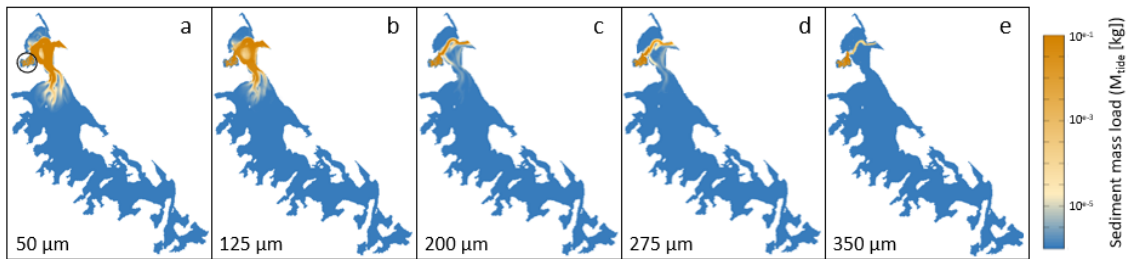
Figure 4.3: Dispersion of sediments (based on sediment mass load [kg]) originating in Tuapiro basin (cell 1; black circle in a) over a tidal cycle, shown for the five grainsize classes (a to e).

To obtain mass loads over a tidal cycle for each of the 20 geomorphic cells (see Figure 4.1), M_{gc} values were summed for all grid cells inside each geomorphic cell (n):

$$M_{tide}(n) = \sum M_{gc}(n) \qquad (4.2)$$

For the model results discussed in the sections below, we focus on sediment mass and transport calculated from the five model simulations with the updated model bathymetries. Since these updated bathymetries represent an approximate, dynamic morphological equilibrium for each grainsize class, it can be assumed that erosion, sedimentation, and overall sediment transport rates for these model simulations are relatively limited. Consequently, the absolute values of the sediment mass and transport over a tidal cycle are small, especially for bed load sediments.

4.3.1 Sediment Connectivity and Cell Strength

When the modelled sediment mass data (M_{tide}) from all geomorphic cells in the estuary are combined, a connectivity matrix can be obtained. Each matrix in Figure 4.4 illustrates the connectivity between the different geomorphic cells for a specific grainsize class, from finest (50 μm; Figure 4.3a) to coarsest sediments (50 μm; Figure 4.3e). Shaded squares inside the matrices indicate the existence of pathways from a given source cell (y-axis) to a given receptor cell (x-axis). The contribution from a source cell to every other possible receptor cell in the system constitutes one row of a matrix. Darker colours represent stronger connectivity between a pair of given cells. The main diagonal of a matrix represents self-self connections, highlighting sediment that stays in the geomorphic cell, as well as sediments that are mobilized and recirculate or return to the cell (Pearson et al., 2020). From our model results, it is impossible to distinguish between these different sediment types, hence the diagonals in the matrices are empty (Figure 4.3). To focus on the most important sediment transport pathways, a minimum sediment mass threshold of 1 x 10^{-5} kg per geomorphic cell was applied. Modelled values of bed load sediment mass over a tidal cycle (M_{tide_bed}) were found to be smaller than this threshold for all grainsize classes. In addition to the development of the connectivity matrices, the role of individual geomorphic cells was analysed in more detail by calculating the sum of the absolute sediment mass for each geomorphic cell (n) as a source ($\sum M_{tide\_out}(n)$; sum of relevant row in a matrix) and the sediment mass for each cell as a receptor ($\sum M_{tide\_in}(n)$; sum of relevant column in matrix). These sediment mass sums represent the total sediment pathways out of (export) and into (import) each geomorphic cell, respectively.

$$\sum M_{tide}(n) = \sum M_{tide\_in}(n) + \sum M_{tide\_out}(n) \qquad\qquad (4.3)$$

The calculated sediment mass $\sum M_{tide}$ reflects the strength of each individual geomorphic cell, and was analysed for the middle grainsize class (200 μm; Figure 4.5a). The spatial distribution of this cell strength throughout the estuary is displayed in Figure 4.5b.

The maximum number of possible geomorphic cell connections, excluding the self-self links, can be described by:

$$m_{max} = (n^2 - n) \tag{4.4}$$

where m represents the amount of connections (i.e. some sediment above the minimum threshold is transferred between cells) and n is the number of cells (20) defined in the estuary. The estuary-level connectivity for each grainsize class can be described by the link density (D; Pearson et al., 2020):

$$D = m \, / \, m_{max} \, x \, 100 \tag{4.5}$$

Consequently, a fully connected estuary would be characterised by $D = 100\%$. The modelled link densities (D) for Tauranga Harbour range from 17% for the coarsest sediment class (350 μm; Figure 4.4e) to 57% for the finest sediments (50 μm; Figure 4.4a). Thus, fine sediments (< 125 μm) unsurprisingly result in greater connectivity throughout the estuary. For coarser sediments (275 and 350 μm; Figures 4.4d and 4.4e) the dominant pathways are primarily confined to the deeper regions of the estuary, where the main tidal channels are located (e.g. cells 2, 4, 6, 12, 17, and 19 in Figure 4.1). As expected, these subtidal environments are also characterised by the overall largest connectivity and greatest cell strength (red and orange circles in Figure 4.5). Sediment mass loads peak in the tidal channels where hydrodynamic energy is greatest, close to the main estuary entrances (~1.0 kg; large dark red circles in Figure 4.5b). Further up-estuary, tidal energy is somewhat reduced, resulting in a decrease in sediment mass and cell strength (~0.07 kg) illustrated by the orange circles in the centre of the main estuary (Figure 4.5b).
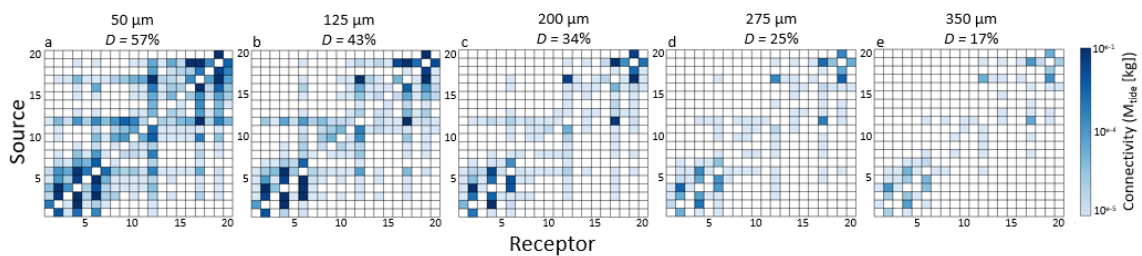
Figure 4.4: Connectivity matrices for the five grainsize classes, shown from finest (a; 50 μm) to coarsest (e; 350 μm) sediments. Coloured squares inside the matrices represent the connectivity (based on sediment mass load; M_{tide}) between a geomorphic source cell (y-axis) and a receptor cell (x-axis). Darker colours indicate stronger connectivity between cells. Link density values (D) shown above the matrices describe the system-level connectivity for each grainsize.

For the smaller sub-basins, the cell strength results based on the middle grain size class highlight that basins located relatively close to the main northern and southern estuary

entrances are characterised by greater sediment mass loads (~0.01 kg), reflected by the lighter green circles (Figure 4.5; e.g. cell 1, Tuapiro; and cell 18, Waikareao). Sub-basins located further away from the main estuary entrances encounter reduced hydrodynamic energy, resulting in decreasing sediment loads and reduced cell strength (dark green and blue circles in Figure 4.5). Basins with smallest strength are located near the centre of the estuary (< 0.0001 kg), most notably within the western part of the southern estuarine basin (Figure 4.5; e.g. cell 13, Mangawhai; and cell 15, Waikaraka), where sediment exchange is limited to the adjacent small basins. The connectivity matrices reveal that sediment exchange between the northern and southern basin of the estuary is relatively common for finer sediments (< 200 μm; Figure 4.4a to 4.4c). This exchange is most substantial between the cells that represent the main tidal channels in both basins, especially those cells that are located towards the centre of the estuary (cells 4, 6, 12, and 17). However, the shallower sub-basins in the upper regions of the estuary can also contribute to the large-scale exchange between the northern and southern basin, highlighted by the connectivity between cells 3, 5, and 7 (northern basin), and cells 8, 9, and 10 (southern basin) for the smallest grainsize classes (50 and 125 μm; Figures 4.4a and 4.4b).
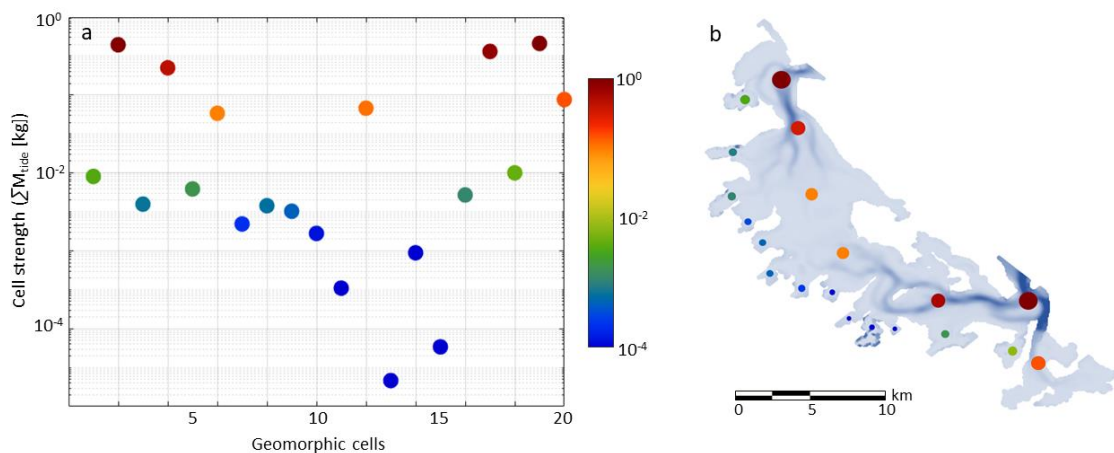
Figure 4.5: The sum of the absolute sediment mass loads (ΣM_{tide}) for a tidal cycle (y-axis), highlighting the geomorphic cell strength (a). Cell strength represents the total sediment import and export for each geomorphic cell (x-axis). The spatial distribution of the cell strength variation (b) illustrates greatest strength in the large tidal channels.

A number of the mainly ebb-dominant, convergent sub-basins located on the landward side of the main estuary are characterised by a relatively large amount of sediment export to other cells, especially for grainsizes of 200 μm and smaller. These sub-basins include Katikati, Tuataekaka, and Wairoa (cells 3, 5, and 16, respectively). When focusing on the 125 μm grainsize class, for example, Katikati (cell 3) contributes sediment to more than half of the total amount of geomorphic cells in the estuary (12 out of 20 coloured cells in row 3 of the matrix in Figure 4.4b). However, sediment pathways into Katikati from other

sources are rather limited (6 out of 20 coloured cells in column 3 of Figure 4.4b). The connectivity patterns for the other convergent sub-basins are relatively comparable, with an overall greater amount of sediment export than import. The main divergent sub-basins in the estuary, which include Tuapiro, Te Puna, and Waikareao (cells 1, 14, and 18, respectively), display different connectivity patterns when compared to the convergent basins. Te Puna, for example, contributes sediment (125 μm) to only a few other cells (3 coloured cells in row 14 of Figure 4.4b, excluding itself), whereas the basin imports sediments from 7 basins (coloured cells in column 14 of Figure 4.4b, excluding itself). The overall connectivity patterns for the flood-dominant, divergent basins inferred from the matrices (Figure 4.4) suggest that inside these environments, sediment import is dominant.

4.3.2 Sub-Basin Sediment Import and Export

Sediment transport can be modulated by the geometry of the basins. To analyse the patterns of sediment import and export for the shallow divergent and convergent sub-basins in more detail, sediment transport through the entrances of the sub-basins over a tidal cycle (S_{tide}) was determined from the model results for all sediment classes, as:

$$S_{tide} = \int_0^x \int_0^T C(t)U(t)dtdx \tag{4.6}$$

where C is the sediment concentration (kg/m^3), and U is the current velocity perpendicular to the across-entrance transect (m/s). Transport ratios (Figure 4.6a) were calculated for six sub-basins (three divergent, and three convergent basins; Figure 4.6b), based on the ratios of sediment import and export over a tidal cycle (S_{in} / S_{out}) through cross-sections of the basin entrance channels. Net sediment import or export is characterised by ratios greater, or smaller than one, respectively. The transport ratios indicate whether a basin may be a sediment source (net export) or a sink (net import). The patterns of import and export may be related to the basin intertidal profile shape as well as the basin planform shape (geometry). Sub- and intertidal profile shape is described by the hypsometry (γ; Figure 4.6a), where values of $\gamma \approx 2$ indicate convex-shaped hypsometric profiles, and greater values ($\gamma > 3$) suggest more concave-shaped profiles. Basin dilation factors (BDF; Figure 4.6a) characterise the geometry of the sub-basins, using the basin entrance width (w_{entr}) and the average width of the landward half of the basin (w_{est}):

$$BDF = \frac{w_{est}}{w_{entr}} \tag{4.7}$$

Convergent and divergent basins are characterised by BDF values smaller and greater than 1.0, respectively. The transport ratio results, displayed for the five modelled grainsize classes (Figure 4.6a; x-axis), highlight that the divergent basins (Figure 4.6a; blue and purple lines with triangles) are generally characterised by transport ratios greater than one, suggesting net sediment import. The import for these mainly flood-dominant basins become stronger (greater ratios) with increasing sediment grainsize (towards the right of the Figure 4.5a). Te Puna basin is shown to have strongest import signals (dark blue triangles) based on the transport ratios. The convergent basins (green, yellow, and red lines with circles) are defined by transport ratios smaller than one, indicating net sediment export. Wairoa basin (red circles) is found to be the most exporting environment overall. The transport ratios are shown to increase for basins with more convex hypsometric profiles ($\gamma \approx 2$), and divergent geometries (BDF > 5). However, the dependence of sediment transport ratios on basin hypsometry and geometry is not linear.
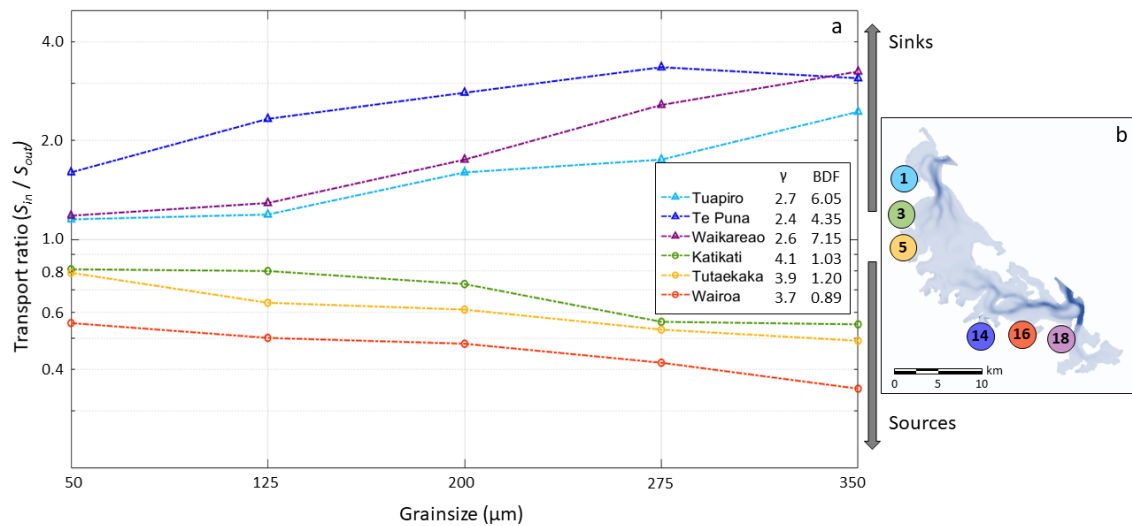
Figure 4.6: Modelled sediment transport ratios (S_{in} / S_{out}; y-axis) through cross-sections of the sub-basin entrance channels. Transport ratios (y-axis) greater than one indicate net sediment import; ratios smaller than one suggest net export. Transport ratios are modulated by sediment grainsize (x-axis). Hypsometry exponents (γ) and basin dilation factors (BDF) are listed for the divergent (triangles) and convergent (circles) sub-basins (de Ruiter et al., 2019).

4.3.3 Within Sub-Basin Sediment Transport Patterns

In order to explore how sediment transport patterns are modulated by basin characteristics and sediment grainsize further inside the sub-basins, sediment transport integrated over a tidal cycle (S_{tide}; see 4.6) was analysed for cross-sections taken perpendicular to the basin channels at roughly one-third of the total distance into the basins (see cross-section example for Waikareao in Figure 4.7g). Since hydrodynamic energy further inside these

basins is low, transport rates are also small (Figure 4.7). Positive transport values deduced from the model results indicate flood-directed transport (into the basins), whereas negative values reflect transport in the ebb-direction (out of the basins). The results, illustrated for the five grainsize classes, highlight that inside the three divergent, more infilled basins, currents and associated sediment transport are mainly flood-directed (positive values), and concentrated in the relatively deep tidal channels (areas within the dotted lines in Figures 4.7a to 4.7c; note the different y-axis scales). Greatest transport in the subtidal channels for a tidal cycle occurs for the smallest grainsizes, as expected (50 and 125 μm; blue and purple lines). In the elevated intertidal regions of the basins (outside of the dotted lines in Figures 4.7a to 4.7c), sediment transport rates are substantially smaller. For the finest grainsizes (50 and 125 μm), the values of the intertidal transport are roughly 50% of the transport in the divergent channels. In the increasingly shallow upper parts of the intertidal regions (towards the left and right in Figures 4.7a to 4.7c), the transport direction can change from flood- to ebb-directed (negative values). With increasing grainsize, the differences between channel and intertidal transport become greater. Intertidal sediment transport in the divergent basins for grainsizes greater than 275 μm are minimal (yellow and red lines in Figure 4.7a to 4.7c).
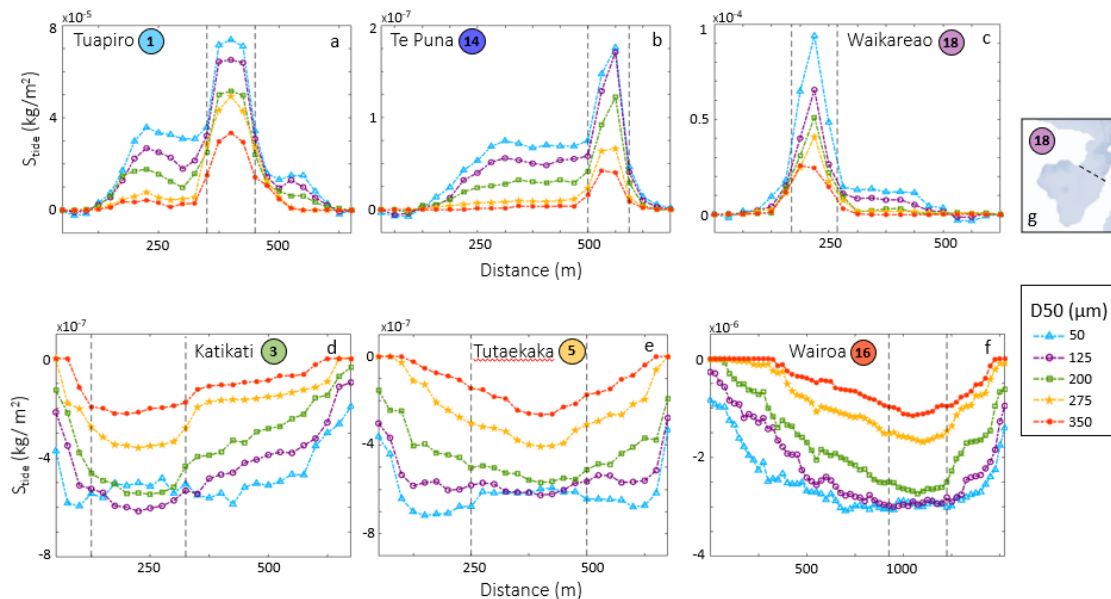
Figure 4.7: Sediment transport (y-axis) integrated over a tidal cycle (S_{tide}) through channel-perpendicular cross-sections in the lower sub-basins (see Waikareao example in g), shown for the five grainsize classes (coloured lines). Positive values indicate flood-directed transport (into the basins), whereas negative values reflect ebb-directed transport (out of the basins). Inside the flood-dominant divergent basins (a, b, and c) transport is mainly focused in the subtidal channels (areas within dotted lines). In the ebb-dominant convergent basins (d, e, and f), transport is more evenly distributed between subtidal channels and flats. Note the different y-axis scales.

Sediment transport patterns in the convergent, less-infilled basins differ from the divergent basin transport patterns and are mainly ebb-directed (negative values). In general, transport rates are again greatest for the finest grainsize classes, and peak in the subtidal channels (areas within the dotted lines in Figures 4.7d to 4.7f). However, because elevation differences between the channels and intertidal regions are less pronounced in divergent basins, contrasts between intertidal and subtidal transport are also smaller. Sediment transport for grainsizes up to 200 μm is substantial in the channels as well as in the somewhat shallower regions outside of the channels (blue, purple, and green lines in Figures 4.7d to 4.7f). For very fine sediments (50 μm), transport values within the channels can be less ebb-directed (smaller negative values) than transport values outside of the channels (Figure 4.7d and 4.7e).

In general, sediment transport rates are most substantial for the sub-basins that are nearest to the northern and southern entrances of the main estuary (e.g. Tuapiro, and Waikareao; max. ~1^{e-4} kg/m^2), with smallest transport values occurring in the Te Puna basin (max. ~2^{e-7} kg/m^2).

4.4 Discussion

Sediment transport pathways between different parts of a coastal system are modulated by a non-linear interplay of hydrodynamic processes and morphological feedbacks. We show that sediment connectivity is a useful framework for analysing connections between a large number of geomorphic regions in a shallow estuarine system with associated small sub-basins. By applying the connectivity framework (Bracken et al., 2015; Pearson et al., 2020), we resolve the system-scale sediment pathways as well as the smaller-scale links between sub-basins. Our study illustrates that sediment connectivity can reveal details of transport pathways that were hitherto unknown. For example, it was previously assumed that connectivity between the northern and southern basin of Tauranga Harbour was negligible (e.g. Tay et al., 2013). In contrast, our model results reveal that sediment exchange between the two basins may be relatively common for finer sediments (Figure 4.8).

Sediment grainsize characteristics have a significant impact on levels of connectivity throughout the estuary, as highlighted by the conceptual model shown in Figure 4.8. Our results confirm that finer sediments (< 200 μm; fine sands and silts) are associated with greater overall sediment connectivity, as they are mobilized in both relatively deep (channels) and shallower (flats) regions of the estuary. These fine sediments are

transported over great distances, functionally connecting geomorphic cells throughout the estuary in both the northern and the southern basins. Deposition of finest sediments will be limited to low-energy tidal flat regions, both along the sides and in the upper reaches of the main estuary, as well as in the shallow sections of the sub-basins, as expected in a shallow tidally-dominated estuary (Dalrymple et al., 1992). Transport and deposition of coarse sandy sediments are primarily focused in more energetic regions of the main estuary, such as the deeper tidal channels (Figure 4.8). Sediment connectivity of these coarser sediments is generally restricted to cells that are located in relatively close proximity to each other. Coarsest sediment may be expected in the deep tidal channel sections located in the lower parts of the northern and southern basin of the estuary. The general sediment distribution described here for Tauranga Harbour is relatively common for shallow, relatively sheltered, and tidally-dominated estuary systems (e.g. Woodroffe et al., 1989; Dalrymple et al., 1992). Since fluvial input and wave energy are relatively limited in the estuary, a clear tripartite facies distribution, consisting of coarse sediments at the estuary mouth and head, and fines in the central basin, cannot be distinguished.

Our research also substantiates the findings of our earlier studies (de Ruiter et al., 2019; De Ruiter et al., 2021), by confirming that shallow, divergent basins in Tauranga Harbour mainly act as sediment sinks. These basins were previously found to be primarily flood-dominant, which leads to the infilling environment and convex-shaped hypsometric profile that is characteristic of a sediment sink. The sediment import in these basins becomes relatively stronger with increasing sediment grainsize (Figure 4.5a). This grainsize-dependent change in transport ratios is most likely a result of the weaker ebb-directed currents in the basins no longer being able to transport the larger grains when grainsize increases, whereas the flood-directed currents still are strong enough for coarser sediment to be transported. Hence, flood-directed sediment transport (import) can become relatively stronger for larger grainsizes. The convergent basins are more ebb-dominant, leading to overall less-infilled environments that may be classified as sediment sources. Within these basins, sediment transport over a tidal cycle for fine sediments can be smaller in the channels than outside of the channels (Figure 4.7d and 4.7e). This apparent decrease in sediment transport - a sum of positive flood-directed transport and negative ebb-directed transport - is a result of a relatively greater increase in flood fine sediment transport, when compared to ebb transport, and illustrates once again how sediment grainsize can modulate the basin transport pathways. Our results highlight that the relationships between sediment import and export, and basin hypsometry and geometry

is not linear. This non-linearity suggest that other factors also affect sediment pathways in shallow basins.

Figure 4.8: Conceptual model of the main sediment transport pathways in Tauranga Harbour, based on our sediment connectivity analysis. The arrows indicate the range of sediment grainsizes (colour) transported between the different estuary regions, and the relative strength of the connections (arrow size). Note that the different arrow ends may show transport of different sizes. The six divergent and convergent sub-basins are also highlighted in the figure (blue icons). Transport of coarse sediments (>300 μm) is mainly confined to the deep tidal channels, whereas sub-basins and upper estuary regions are characterised by transport of mainly finer sediment fractions (<200 μm).

Based on our findings, specific connectivity patterns may exist for combinations of different basin geometries. Such patterns were further explored by adopting the connectivity (sediment mass loads; M_{tide}, based on Figure 4.4) between different source-receptor basin combinations for the six divergent and convergent sub-basins (geomorphic cells 1, 14, 18, and geomorphic cells 3, 5, 16, respectively). Connectivity was determined

for all grainsize classes separately, with each connectivity value for a source-receptor combination corresponding to one specific cell of a connectivity matrix (Figure 4.4). The connectivity (M_{tide}) for each source (i) – receptor (j) basin combination was normalised by the mean of the summed sediment loads ($\sum M_{tide}$; Figure 4.5) for the two relevant basins:

$$S_n = M_{tide\_ij} / ((\sum M_{tide\_i} + \sum M_{tide\_j})*0.5) \qquad\qquad (4.9)$$

where S_n is the normalised sediment load (indicating connectivity), M_{tide_ij} represents the connectivity between basins i (source) and j (receptor), and $\sum M_{tide\_i}$ and $\sum M_{tide\_j}$ are the summed sediment loads for each basin. Since the six convergent and divergent basins are distributed throughout the estuary (coloured circles in Figure 4.1), some of the basin combinations result in a connectivity of zero. The remaining normalized sediment loads were analysed and averaged for each grainsize class. The results show that, as expected, the normalised mass loads (and thus the connectivity) generally decrease with increasing grainsize (Figure 4.8, towards the right). When a convergent, less-infilled basin represents the sediment source, and a divergent, infilled basin is the receptor (red line in Figure 4.8; C → D), connectivity is shown to be the greatest overall. The relatively strong connectivity for this C → D combination confirms that this combination represents the 'natural' state of the flood-dominant divergent and ebb-dominant convergent basins within Tauranga Harbour, as suggested by our findings (divergent basins are sinks, convergent basins are sources). Connectivity between ebb-dominant convergent basin combinations is shown to also be fairly strong (black line in Figure 4.8; C → C). When flood-dominant divergent basins are taken as sediment sources (blue and purple lines in Figure 4.8; D → D and D → C), mass loads and connectivity are substantially smaller and decrease rapidly with increasing grainsize. For coarser grainsizes (> 200 μm), no links exist at all between divergent sources and divergent or convergent receptors.

Our results thus clearly illustrate the links between sediment connectivity, basin hypsometry and geometry, basin function (source or sink), and sediment grainsize. It has to be noted that these connectivity-related patterns are also modulated by the morphology of the adjacent main estuary, and hence by the location of the sub-basins within the larger estuarine system. Future changes in sea level may have an impact on sediment connectivity and transport processes in shallow estuarine systems. The magnitude of these impacts depends on a range of local factors, including sediment supply, modifications of tidal processes, and geological constraints (i.e. Robins et al., 2010; Fagherazzi et al., 2012). An increase in water depth induced by sea level rise leads to greater flood

dominance and transgression of the system, resulting in the potential drowning of shallow intertidal regions (e.g. Dalrymple et al, 1992; Kirwan and Temmerman, 2009).
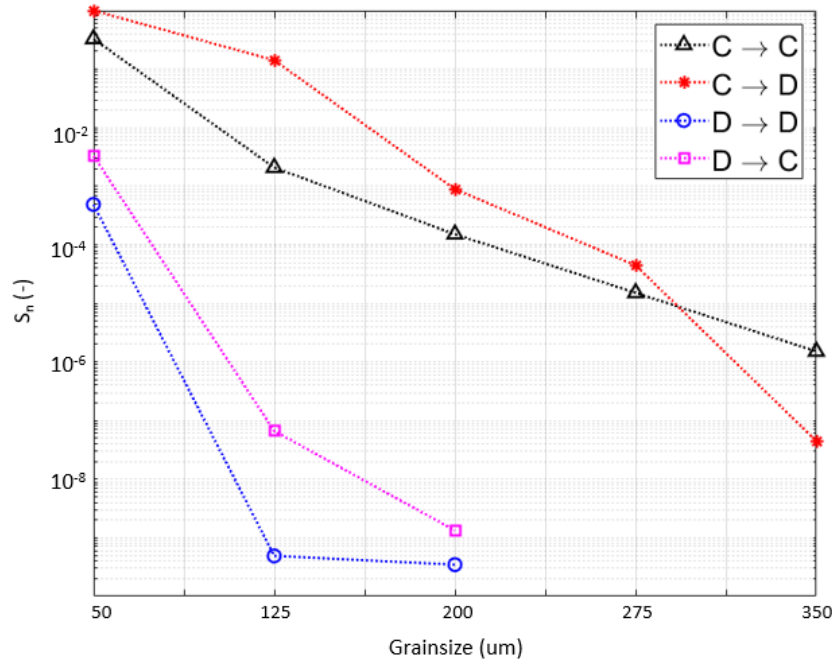
Figure 4.9: Normalized sediment loads (S_n; y-axis) between different combinations of divergent (D) and convergent (C) sub-basins, reflecting rates of connectivity. The legend indicates the direction of transport from sources (left of arrows) to sinks (right of arrows) in the combinations (coloured lines). Data shows that connectivity is generally greatest when convergent basins (C) are sources and divergent basins (D) are sinks (red line). Sediment loads are shown to be modulated by sediment grainsize (x-axis).

In situations where sediment supply increases in tandem with accommodation space, the estuary can adjust to maintain its overall form without any significant changes to hydrodynamics and intertidal hypsometric profiles. Sediment connectivity patterns may change, as increased amounts of primarily fine and medium sediments will be transported into the upper estuary, gradually moving the whole system landward (Townend and Pethick, 2002; Liu et al., 2019). If external sediment supply is greater than the increase in tidal range, further imports of sediment may result in accretion in line with sea level rise, potentially expanding intertidal regions and increasing convexity of hypsometric profile (e.g. Kirwan et al., 2010). Conversely, if sediment supply is limited relative to sea level rise, changes in sediment connectivity and hypsometry will occur due to erosion of intertidal flats. Convex-shaped profiles may increasingly evolve into more concave profiles, further increasing average water depths, even in sheltered divergent basins. Previous studies have shown that estuarine responses to sea level rise are modulated by complex feedback loops and the interaction of multiple spatial and temporal scales (e.g. Townend, 2004; Liu et al., 2019). Consequently, detailed modelling studies are essential

when examining the effects on sea level rise on hydrodynamics, hypsometry, and sediment connectivity in estuarine systems with specific geometric and morphological characteristics.

4.4.1 Study Limitations

The results from our modelling study have allowed us to explore system-scale sediment connectivity patterns inside a shallow estuary. Additionally, we were able to determine links between smaller-scale sub-basin connectivity patterns and specific basin characteristics such as geometry and hypsometry. However, processes related to sediment connectivity within estuarine systems are non-linear, and driven by interactions between range of different processes related to hydrodynamics, local morphology, sediment characteristics, and meteorological conditions. Our current depth-averaged hydrodynamic model is a simplified representation of a natural estuary. A three-dimensional model representation of an estuary could provide an opportunity to explore both the system-scale and small-scale sediment connectivity patterns in greater detail. The inclusion of processes such as wind and wave forcing, as well as freshwater input could further improve our understanding of sediment connectivity patterns. Short period, locally generated waves have been shown to be morphologically significant hydrodynamic processes in relatively exposed estuarine systems (e.g. Hunt et al., 2015). Consequently, wave forcing may be able to substantially affect sediment connectivity in mainly convergent estuarine basins.

Our research indicates that sediment grainsize has a substantial impact on sediment pathways and rates of connectivity. Due to computational limitations, we explore the effects of the five grainsize classes on connectivity separately in our study. Simulating the transport of a mixture of sediment grain sizes throughout an estuary would enhance knowledge of the links between sediment distribution, connectivity pathways, and associated sub- and intertidal morphological changes.

The application of graph theory to coastal sediment connectivity also has its limitations. Identifying appropriate scales for connectivity analyses, both spatial and temporal, can be challenging, as noted in previous studies (e.g. Bracken et al., 2015; Keesstra et al., 2018; Wohl et al., 2019). Defining a limited number of nodes or cells within a dynamic coastal system requires simplifications and potential loss of information (Moilanen, 2011). Consequently, the initial schematization of a network of geomorphic cells is a step that requires scrutiny, in order to ensure that connections and patterns within a system are not

oversimplified. The sensitivity of sediment pathways in estuaries and small tidal basins to different choices of spatial cell distribution depends on the schematization resolution (geomorphic cell size). When exploring sediment connectivity patterns on longer timescales (e.g. months or years), long-term feedback mechanisms need to be considered when determining the initial cell network. On these longer timescales, gradients in sediment mass loads can eventually modify the estuarine morphology (e.g. Duong et al., 2016)., which in turn would modify sediment transport patterns. Additionally, long-term vertical land movement variations may affect accommodation space and sedimentation rates. Hence, both spatial and temporal scales influence connectivity patterns observed in coastal systems.

Understanding the interplay between hydrodynamics, sediment transport pathways, and physical characteristics of coastal systems is vital for the development of management strategies related to coastal erosion, increased flooding, and ecosystem functioning. Our study highlights that existing connectivity metrics can be effective for exploring the links between the aforementioned processes. However, sediment connectivity primarily describes transport pathways in a coastal system, and hence does not necessarily reflect patterns of sediment deposition and erosion. Metrics specifically developed for analyses of sediment transport as well as deposition in estuaries and tidal basins may provide opportunities to evaluate sediment connectivity and rates of sedimentation in these coastal systems in even more detail (Pearson et al., 2020). Previous studies have indicated that sub-basin size and intertidal geometry have a strong impact on the magnitude on hydrodynamics and sediment transport potential (e.g. Ridderinkhof et al., 2014). The links between geometry, hydrodynamics, morphology and sediment connectivity found in our research are mainly applicable to small-scale shallow tidal basins and shallow estuarine environments.

4.5 Conclusions

Sediment transport processes in shallow coastal systems are complex and dynamic. In order to reliably predict morphological evolution in these environments, a detailed understanding of sediment transport pathways is necessary at multiple scales. Our study results demonstrate that sediment connectivity, inferred from sediment mass loads in a shallow estuary, provides valuable insight into the connections between geomorphic regions within an estuary on different spatial scales. Additionally, our study illustrates that sediment connectivity can reveal details of transport pathways that were previously

unknown. Numerical model data indicates that sediment pathways are modulated by hydrodynamic energy, estuarine morphology (depth), local hypsometry and geometry (planform), and sediment grainsize. Sediment connectivity in the estuary is greatest for fine sediments, with peak connectivity values found in the deeper tidal channels of the main estuary, where hydrodynamic energy is greatest. Connectivity is reduced in shallower intertidal regions and inside small sub-basins adjacent to the main estuary, but still remains substantial in these areas for finer sediment grainsize classes. We show that tidal processes, sub-basin characteristics, and sediment connectivity are linked, with flood-dominant divergent basins representing sediment sinks, and ebb-dominant, convergent basins being sediment sources. However, these relationships are shown to be dynamic and non-linear. Our study highlights that connectivity metrics can be effective for exploring links between sediment connectivity, morphology and geometry, and hydrodynamic processes in shallow estuarine systems and tidal basins.

Chapter 5
General Conclusions

5.1 Review of Major Concepts

The research presented in this thesis aimed to enhance our understanding of the links between geometric and hypsometric characteristics of shallow estuarine systems, and the hydrodynamics, tidal processes, and sediment connectivity patterns inside these coastal environments. In Section 1.4, the aims of the thesis were abstracted into three research questions.

1. How do basin geometry and hypsometry affect hydrodynamics and tidal asymmetry in shallow tidally dominated basins?

Estuaries and tidal basins are ubiquitous coastal geomorphic systems shaped by connected fluxes of water and sediment. This research highlights the complexity of the links between geomorphological characteristics of shallow estuarine systems, tidal asymmetry, and bed shear stress patterns inside such systems, and the associated hypsometric intertidal profile shapes. Chapter 2 compared tidal energy within shallow, divergent microtidal basins, characterised by a narrow entrance with deep entrance channels and landward-increasing basin widths (BDF > 1.0), and more open, convergent microtidal basins with less-pronounced tidal channels (BDF ≈ 1.0). The findings are based on numerical modelling of a real-world shallow estuarine system. The accuracy of the numerical model was substantiated through calibration and validation of the model based on field data analysis.

Distortion of the tidal wave was found to be greatest in shallower basin sections, specifically in the upper intertidal regions of divergent basins. The sheltered basin centres of these constricted environments are associated with small bed shear stress values and high rates of flood-directed tidal velocity asymmetry, indicating a large potential for landward sediment transport of larger particles. Weakly ebb-directed asymmetries in slack water duration suggest a limited potential for export of finer sediments. Nonetheless, in general these relatively low-energy divergent basins can be described as infilled, depositional environments and sediment sinks. These sheltered divergent environments

are characterised by convex hypsometric profiles ($\gamma \approx 2.0$ - 2.5) with substantial, elevated intertidal regions. Such extensive intertidal flats offer increased protection against flooding and coastal erosion.

Shallow tidal basins with convergent geometries are characterised by comparatively high-energy conditions within basin centres. Consequently, bed shear stress values are larger and tidal velocity asymmetry is primarily ebb-directed, suggesting limited potential for sediment deposition in these unconstricted environments. The slack tide duration asymmetry is weakly flood-dominant, indicating that limited input of fine sediment into the basins is possible. The energetic conditions and mainly ebb-dominant tidal currents within the exposed basins result in a more concave hypsometric profile ($\gamma \approx 4.0$), with lower and less-pronounced intertidal flats. These convergent and more erosional environments may be preferred in shallow environments where navigability is of prime importance.

Chapter 2 highlights the impacts of specific geomorphologic basin characteristics, such as entrance constrictedness, basin width, and intertidal profile shape, on tidal processes in shallow estuarine basins. The ability to predict the non-linear interplay between tidal asymmetry and morphological changes in distinct tide-dominated systems is advantageous from a coastal management perspective, as the morphological evolution of estuarine sub- and intertidal regions affects present and future coastal ecosystem functioning, port and estuary navigability, and coastal protection potential.

2. How do wind-generated currents modulate velocity asymmetry in shallow tidal basins with varying geometries?

Meteorological forcing can play a substantial role in modulating the stability relationships between geomorphologic characteristics, hydrodynamics, and sediment transport potential in shallow estuarine systems, such as the microtidal basins described in Chapter 2. Wind-driven currents, specifically, are critical drivers of horizontal velocity asymmetry change in shallow tidal basins with varying planform shapes and bathymetry, as highlighted by the idealised numerical modelling study described in Chapter 3. The associated velocity asymmetry patterns are not a straightforward sum of the velocities caused by tide-only and wind-only forcing, but depend on the wind attributes, tidal basin geometry, local water depth and the characteristics of the underlying tide-induced currents. In general, an increase in wind speed promotes more extreme horizontal velocity

asymmetry (larger velocity asymmetry values) without substantially altering the overall spatial pattern of velocity asymmetry. This result holds true throughout both the mainly flood-dominant and infilled divergent basins, as well as the ebb-dominant, less-infilled and convergent basins described in Chapter 2. The wind forcing primarily influences residual and peak flow velocities, with a minimal effect on tidal harmonics inside both basin configurations. Changes to velocity asymmetry patterns are most evident for wind speeds of 6 m/s and greater, and for wind directions parallel to the main axes of the tidal channels in the basins. Shallow intertidal basin regions are characterized by a downwind-directed increase in velocity asymmetry, forced by wind-generated currents aligned with the wind direction. In deeper subtidal channels the wind-driven currents oppose the wind direction, resulting in asymmetry changes that can contrast with the intertidal velocity asymmetry. Consequently, the wind-driven velocity asymmetry changes inside shallow tidal basins are strongly depth-dependent. Timing and duration of a wind event can also influence the velocity asymmetry patterns in the shallow divergent and convergent basins. Wind events coinciding with flooding tides result in the most noteworthy differences between the relative magnitudes of the peak flood- and ebb directed currents, especially for wind event durations of 6 hours or less.

This work indicates that hydrodynamic and sediment transport processes, and associated morphological evolution in shallow estuarine systems are controlled by tidal forcing as well as wind event characteristics. The influence of wind-driven currents over a tidal cycle can produce the velocity asymmetries necessary for sediment to be transported at relatively short timescales in both infilled and divergent basins, as well as in more erosional and convergent, shallow environments. Considering the potential increased intensity of extreme meteorological events due to anthropogenically induced climate change in shallow coastal regions, the ability to predict future pathways of morphological change in such systems, based on specific meteorological conditions as well as well-defined local tidal regimes, is of key importance.

3. What are the relationships between geometry, hypsometry, and sediment connectivity in shallow estuarine systems?

Variations in sediment transport patterns can have a profound effect on the morphological evolution of shallow estuarine environments, which may lead to increased potential for coastal flooding and erosion. Sediment connectivity can provide valuable insight into sediment transport pathways in these dynamic coastal systems, and can reveal details of

transport pathways that were previously unknown. In Chapter 4, numerical modelling was used to analyse the links between functional sediment connectivity, hydrodynamic energy, and local hypsometry for twenty different geomorphic cells inside a shallow estuarine system (Tauranga Harbour, New Zealand), with a focus on the divergent and convergent microtidal basins described in Chapter 2 and Chapter 3. Connectivity matrices developed for five sediment grainsize classes indicate that the system-scale sediment connectivity in a shallow estuarine system is modulated by hydrodynamic energy, estuarine morphology (depth), geomorphic characteristics of the microtidal basins, and sediment characteristics. Sediment mass loads, which can be used as a proxy for sediment connectivity, are depth-dependent, and largest in the deep tidal channels located in the lower sections of the main estuary, where tidal energy is greatest. In the upper, more sheltered and increasingly shallow parts of the estuary, as well as inside the shallow divergent and convergent tidal basins, connectivity is reduced. Sediment transport and connectivity are further moderated by grainsize. For fine sediments (< 125 μm) connectivity is substantial throughout the main estuary and the shallow tidal basins, with estuary-level connectivity (link density) exceeding 50%. For coarser sediments (> 275 μm), dominant transport pathways are confined to the deeper regions of the system, with link density being ~20%. The smaller-scale sediment transport pathways, described by the sediment connectivity between the shallow tidal basins, are modulated by the geomorphological characteristics of the basins, as well as the morphology of the main estuary, in a dynamic and non-linear fashion. The results of Chapter 4 confirm the findings described in Chapters 2 and 3, by highlighting that shallow, flood-dominant, and divergent basins are accretionary environments (convex hypsometry) that mainly function as sediment sinks, whereas ebb-dominant convergent basins are markedly less infilled, and primarily act as sediment sources. The work also revealed a result of local significance: the exchange between the northern and southern basins of Tauranga Harbour was found to be relatively common (albeit small) for finer sediment fractions, in contrast to the previous assumption that connectivity between the basins is negligible. Our study highlights the effectiveness of the sediment connectivity framework for exploring present and future hydrodynamics, sediment transport pathways, and morphological and geometric variations in shallow, tidally-dominated estuarine systems.

In this research, the links between hydrodynamic processes, sediment connectivity patterns, and geomorphological characteristics inside a shallow estuarine system were explored. The results presented in this work are based on a depth-averaged, simplified

representation of a natural estuary. Furthermore, processes such as wave forcing, freshwater input, and sediment transport based on a mixture of varying sediment grainsizes were not considered. Consequently, the inclusion of three-dimensional hydrodynamic, meteorological, and detailed sedimentary processes could provide an opportunity to explore future changes in sediment connectivity patterns in shallow estuarine systems in even greater detail.

5.2 Recommendations for Future Research

5.2.1 Climate Change and Sea Level Rise

As demonstrated throughout the work presented in this thesis, estuaries and tidal basins are dynamic environments characterised by non-linear interactions between tidal processes, meteorological forcing, sediment transport processes, and morphological feedbacks. These highly dynamic coastal environments are susceptible to future climate change and associated sea level rise (SLR; e.g. Wong et al., 2014), as also highlighted in Section 1.3. The potential impacts of changes in sea level on future morphological functioning of shallow estuarine systems are still largely unknown. Shallow and small-scale coastal systems, such as the microtidal basins investigated in this research, may, for example, be especially sensitive to tidal amplification as a result of their limited mean water depth, potentially increasing the risk of flooding (Leuven et al., 2019). However, the SLR-induced response of shallow tidal basins also depends on a range of other factors, including sediment supply, local tidal processes, and geological constraints (e.g. Dalrymple et al, 1992; Robins et al., 2010; Fagherazzi et al., 2012).

An investigation into the effects of SLR in shallow estuarine systems with specific geomorphologic characteristics, such as the divergent and convergent basins described in this thesis, will require an improved understanding of the hydrodynamics, tidal processes, and morphological feedbacks inside these systems on longer timescales. Since the relative morphological adjustments of shallow estuarine systems, when compared to predicted changes in SLR, is modulated by sediment availability (e.g. Townend & Pethick, 2002; Leuven et al., 2019), an examination of SLR-induced effects should include a detailed description of sediment characteristics and supply. Additionally, future pathways of basin morphological evolution depend on the effects of wind climate. Winds may induce long-term morphological feedback mechanisms, controlled by wind-induced currents, as explored in Chapter 3, as well as changes in local wave climate. The long-term effects of wind-related currents and waves may be limited within sheltered divergent environments,

whereas more open convergent estuarine systems may be susceptible to increased erosion from morphologically significant waves. An exploration of the combined effects of predicted tidal processes and meteorological forcing would assist in determining critical conditions for substantial changes in patterns of erosion and sedimentation in estuarine systems. The resulting modifications of sediment pathways may affect ecological tipping points related to coastal vegetation such as seagrasses and mangroves. Consequently, it is crucial to adequately define meteorological forcing when studying future morphological evolution of shallow estuarine systems with specific geometrical, morphological, and landscape settings.

5.2.2 Estuarine System Modelling

Numerical modelling is an important tool for studying process-response dynamics and geomorphological adaptation related to predicted climate change in coastal systems. In order to analyse the non-linear interactions between a range of different processes related to tidal forcing, sediment connectivity, meteorological conditions, and morphology evolution inside shallow coastal systems, the development of a comprehensive numerical model that encompasses these processes is essential. The primarily depth-averaged idealised and real-world numerical models developed for this thesis could be further enhanced for the purpose of studying the effects of climate change in detail, by including a three-dimensional model representation of hydrodynamic and sedimentary processes that includes secondary circulation and density-driven flows as a result of salinity and temperature gradients. As noted above, the inclusion of potentially important processes such as wave forcing, freshwater input, and detailed sediment grainsize characteristics should also be considered.

The links between hydrodynamics, geometry, morphology and sediment connectivity described in our research are mainly applicable to small-scale shallow tidal basins and shallow estuarine environments. In order to further enhance our understanding of the potential morphological evolution induced by climate change inside estuarine systems worldwide, future modelling studies should be expanded to encompass a larger range of different estuarine systems with varying geometric and morphological characteristics.

5.3 Summary

This thesis explores the interplay between hydrodynamics, tidal processes, geomorphologic basin attributes, meteorological conditions, and sediment connectivity in shallow estuarine systems. Hypsometric and geometric characteristics of estuarine

basins, as well as wind forcing, were found to play a substantial role in modulating the tidal asymmetry and sediment connectivity patterns inside these shallow environments.

References

Agardy, T., and Alder, J. (2005) Coastal Systems. In: Hassan, R., Scholes, R. And Ash, N. (eds.) Ecosystems and Human Well-being: Current State and Trends, Volume 1. Findings of the Conditions and Trends Working Group of the Millennium Ecosystem Assessment. Island Press.

Alekseenko, E., and Roux, B. (2017) Numerical simulation of the wind influence on bottom shear stress and salinity fields in areas of Zostera noltei replanting in a Mediterranean coastal lagoon. Progress in Oceanography, 163, 147–160. DOI: 10.1016/j.pocean.017.05.001

Alekseenko, E., and Roux, B. (2019) Contribution to remediation of brackish lagoon: 3D simulation of salinity, bottom currents and resuspension of bottom sediments by strong winds. Estuarine, Coastal and Shelf Science, 216, 27–37. DOI: 10.1016/j.ecss.2018.05.021

Alekseenko, E., Roux, B., Sukhinov, A., Kotarba, R., and Fougere, D. (2013) Coastal hydrodynamics in a windy lagoon. Computers & Fluids, 77, 24–35. DOI: 10.1016/j.compfluid.2013.02.003

Allen, P.A., 2017. Sediment routing systems: The fate of sediment from source to sink. Cambridge University Press.

Balke, T., Herman, P.M.J., and Bouma, T.J. (2014) Critical transitions in disturbance-driven ecosystems: identifying windows of opportunity for recovery. Journal of Ecology 102: 700–708. DOI: 10.1111/1365-2745.12241

Barbier, E.B., Koch, E.W., Silliman, B.R., Hacker, S.D., Wolanski, E., Primavera, J., Granek, E.F., Polasky, S. Aswani, S., Cramer, L.A., Stoms, D.M., Kennedy, C.J., Bael, D., Kappel, C.V., Perillo, G.M.E., and Reed, D.J. (2008) Coastal ecosystem-based management with nonlinear ecological functions and values. Science, 319, 321–323.

Bearman, J.A., Friedrichs, C.T., Jaffe, B.E., and Foxgrover, A.C. (2010) Spatial trends in tidal flat shape and associated environmental parameters in south San Francisco Bay. Journal of Coastal Research 26(2): 342–349. DOI: 10.2112/08-1094.1

Bever, A. J., and Harris, C.K. (2014) Storm and fair-weather driven sediment-transport within Poverty Bay, New Zealand, evaluated using coupled numerical models. Continental Shelf Research, 86, 34-51. DOI: 10.1016/j.csr.2013.07.012

Bever, A.J., and Macwilliams, M. (2013) Simulating sediment transport processes in San Pablo Bay using coupled hydrodynamic, wave, and sediment transport models. Marine Geology 345: 235–253. DOI: 10.1016/j.margeo.2013.06.012

Bever, A.J., McNinch, J.E., and Harris, C.K. (2011) Hydrodynamics and sediment-transport in the nearshore of Poverty Bay, New Zealand: Observations of nearshore sediment segregation and oceanic storms. Continental Shelf Research, 31(6), 507-526. DOI: 10.1016/j.csr.2010.12.007

Bishop, M.J., Mayer-Pinto, M., Airoldi, L., Firth, L.B., Morris, R.L., Loke, L.H.L., Hawkins, S.J., Naylor, L.A., Coleman, R.A., Chee, S.Y., and Dafforn, K.A. (2017) Effects of ocean sprawl on ecological connectivity: impacts and solutions. J. Exp. Mar. Biol. Ecol. 492, 7–30.

Boelens, T., Schuttelaars, H., Schramkowski, G, and De Mulder, T. (2018) The effect of geometry and tidal forcing on hydrodynamics and net sediment transport in semi-enclosed tidal basins. Ocean Dynamics, 68(10), 1285–1309. DOI: 10.1007/s10236-018-1198-9

Bolle, A., Wang, Z.B., Amos, C., and De Ronde, J. (2010) The influence of changes in tidal asymmetry on residual sediment transport in the Western Scheldt. Continental Shelf Research, 30(8), 871–882. DOI: 10.1016/j.csr.2010.03.001

Boon, J.D., and Byrne, R.J. (1981) On basin hypsometry and the morphodynamic response of coastal inlet systems. Marine Geology, 40(1–2), 27–48. DOI: 10.1016/0025-3227(81)90041-4

BoPRC. (2011) Sea lettuce and nutrient monitoring in Tauranga Harbour, 1991-2010 (Report). Whakatane, NZ: Environment Bay of Plenty

Bouma, T.J., van Belzen, J., Balke, T., Zhu, Z.C., Airoldi, L., Blight, A.J., and Herman, P.M.J. (2014) Identifying knowledge gaps hampering application of intertidal habitats in coastal protection: opportunities and steps to take. Coastal Engineering 87: 147–157. DOI: 10.1016/j.coastaleng.2013.11.014

Boyd, R., Dalrymple, R.W. and Zaitlin, B.A. (1991) Classification of clastic coastal depositional environments. Sedimentary Geology 80: 139-150. DOI: 10.1016/0037-0738(92)90037-R

Bracken, L.J., Turnbull, L., Wainwright, J., and Bogaart, P. (2015). Sediment connectivity: A framework for understanding sediment transfer at multiple scales. Earth Surface Processes and Landforms, 40(2): 177–188. DOI: 10.1002/esp.3635

Bryan, K.R., Nardin, W., Mullarney, J.C., and Fagherazzi, S. (2017) The role of cross-shore tidal dynamics in controlling intertidal sediment exchange in mangroves in Cù Lao Dung, Vietnam. Continental Shelf Research 147: 128–143. DOI: 10.1016/j.csr.2017.06.014

Buijsman, M.C., and Ridderinkhof, H. (2007) Water transport at subtidal frequencies in the Marsdiep inlet. Journal of Sea Research, 58(4), 255–268. DOI: 10.1016/j.seares.2007.04.002

Castaing, P., and Allen, G.P. (1981) Mechanisms controlling seaward escape of suspended sediments from the Gironde: a macrotidal estuary in France. Marine Geology 40(1–2): 101–118. DOI: 10.1016/0025-3227(81)90045-1

Christiansen, C., Volund, G., Lund-Hansen, L.C., and Bartholdy, J. (2006) Wind influence on tidal flat sediment dynamics: Field investigations in the Ho Bugt, Danish Wadden Sea. Marine Geology, 235(1–4), 75–86. DOI: 10.1016/j.margeo.2006.10.006

Coco, G., Zhou, Z., van Maanen, B., Olabarrieta, M., Tinoco, R., and Townend, I. (2013) Morphodynamics of tidal networks: Advances and challenges. Marine Geology, 346, 1–16. DOI: 10.1016/j.margeo.2013.08.005

Colby, L.H., Maycock, S.D., Nelligan, F.A., Pocock, H.J., and Walker, D. J. (2010) An Investigation into the Effect of Dredging on Tidal Asymmetry at the River Murray Mouth. Journal of Coastal Research, 26, 843-850. DOI: 10.2112/08-1143.1

Csanady, G.T. (1973) Wind-induced barotropic motions in long lakes. Journal of Physical Oceanography, 3(4), 429–438. DOI: 10. 1175/1520-0485

D'Alpaos, A., Carniello, L., and Rinaldo, A. (2013) Statistical mechanics of wind wave-induced erosion in shallow tidal basins: Inferences from the Venice Lagoon. Geophysical Research Letters, 40(13), 3402–3407. DOI: 10.1002/grl.50666

Dalrymple, R.W., Zaitlin, B.A., and Boyd, R. (1992) Estuarine facies models: Conceptual basis and stratigraphic implications. Journal of Sedimentary Petrology, 62(6): 1130-1146. DOI: 10.1306/D4267A69-2B26-11D7-8648000102C1865D

Danielsen, F., Sørensen, M.K., Olwig, M.F., Selvam, V., Parish, F., Burgess, N.D., . . . Suryadiputra, N. (2005) The Asian Tsunami: A Protective Role for Coastal Vegetation. Science, 310(5748): 643-643. DOI: 10.1126/science.1118387

Dayton, P.K. (2003) The Importance of the Natural Sciences to Conservation. The American Naturalist, Vol. 162, No. 1, pp. 1-13. DOI: 10.1086/376572

De Lange, W.P., and Healy, T.R. (1990) Renourishment of a flood tidal delta adjacent beach, Tauranga Harbour, New Zealand. Journal of Coastal Research 6(3): 627–640.

de Ruiter, P.J., Mullarney, J.C., and Bryan, K.R. (2021). The effects of wind-generated currents on velocity asymmetry in tidal basins with varying geometries. Earth Surface Processes and Landforms, 47(1), 193-208. DOI: 10.1002/esp.5239

De Ruiter, P.J., Mullarney, J.C., Bryan, K.R., and Winter, C. (2017) The influence of entrance constriction on hydrodynamics and intertidal morphology within estuarine basins. Proceedings, Australasian Coasts and Ports 2017 Conference: Working with Nature, Cairns, Australia.

de Ruiter, P.J., Mullarney, J.C., Bryan, K.R., and Winter, C. (2019) The links between entrance geometry, hypsometry and hydrodynamics in shallow tidally dominated basins. Earth Surface Processes and Landforms, 44(10), 1957–1972. DOI: 10.1002/esp.4622

de Swart, H., and Zimmerman, J. (2009) Morphodynamics of tidal inlet systems. Annual Review of Fluid Mechanics, 41(1), 203–229. DOI: 10.1146/annurev.fluid.010908.165159

de Vet, P.L.M., Van Prooijen, B.C., Schrijvershof, R.A., van der Werf, J.J., Ysebaert, T., Schrijver, M.C., and Wang, Z.B. (2017) The importance of combined tidal and meteorological forces for the flow and sediment transport on intertidal shoals. Journal of Geophysical Research – Earth Surface, 123(10), 2464–2480. DOI: 10.1029/2018JF004605

De Vet, P.L.M., Van Prooijen, B.C., and Wang, Z.B. (2017) The differences in morphological development between the intertidal flats of the eastern and western Scheldt. Geomorphology 281: 31–42. DOI: 10.1016/j.geomorph.2016.12.031

Deltares. (2014) Delft3D – Flow simulation of multi-dimensional hydrodynamic flows and transport phenomena, including sediments. User Manual, Version: 3.15, Revision 36209. Deltares: Delft.

Dronkers, J. (1986) Tidal asymmetry and estuarine morphology. Netherlands Journal of Sea Research 20(2): 117–131. DOI: 10.1016/0077-7579(86)90036-0

Dronkers, J. (2016) Dynamics of coastal systems, second edition, Singapore: World Scientific Publishing. DOI: 10.1142/9818

Duong, T.M., Ranasinghe, R., Walstra, D.J.R., and Roelvink, D. (2016). Assessing climate change impacts on the stability of small tidal inlet systems: Why and how? Earth-Science Reviews, 154, 369–380. DOI: 10.1016/j.earscirev.2015.12.001

Duran-Matute, M., Gerkema, T., de Boer, G.G., Nauw, J.J., and Grawe, U. (2014) Residual circulation and freshwater transport in the Dutch Wadden Sea: A numerical modelling study. Ocean Science Discussions, 10(4), 611–632. DOI: 10.5194/os-10-611-2014

Dyer, K.R. (1997) Estuaries: A Physical Introduction, 2nd edition. John Wiley and Sons, Chichester.

Dyer, K.R., Christie, M.C., Feates, N., Fennessy, M.J., Pejrup, M., and van der Lee, W. (1999) An investigation into processes influencing the morphodynamics of an intertidal mudflat, the Dollard estuary, The Netherlands: I. Hydrodynamics and suspended sediment. Estuarine, Coastal and Shelf Science, 50(5), 607–625. DOI: 10.1006/ecss.1999.0596

Elias, E.P.L., Cleveringa, J., Buijsman,M.C., Roelvink, J., Roelvink, D., and Stive, M.J.F.M. (2006). Field and model data analysis of sand transport patterns in Texel tidal inlet (the Netherlands). Coastal Engineering, 53(5–6), 505–529. DOI: 10.1016/j.coastaleng.2005.11.006

Elias, E.P.L., and Hansen, J.E. (2013). Understanding processes controlling sediment transports at the mouth of a highly energetic inlet system (San Francisco Bay, CA). Marine Geology, 345, 207–220. DOI: 10.1016/j.margeo.2012.07.003

Elliott, S., Parshotam, A., and Wadhwa, S. (2010) Tauranga Harbour Sediment Study: Catchment model results (HAM2009-046). Hamilton, New Zealand: National Institute of Water & Atmospheric Research Ltd

Ellis, J., Clark, D., Hewitt, J., Taiapa, C., Sinner, J., and Patterson, M. (2013) Ecological Survey of Tauranga Harbor, revised edn: Manaaki Taha Moana: Nelson, New Zealand. Manaaki Taha Moana Research Report No. 13. Cawthron Report No. 2321. 56 pp. plus appendices.

Engelund, F., and Hansen, E. (1967) A Monograph on Sediment Transport in Alluvial Streams. Copenhagen: Teknish Forlag.

Fagherazzi, S., Kirwan, M.L., Mudd, S.M., Guntenspergen, G.R., Temmerman, S., D'Alpaos, A., . . . Clough, J. (2012) Numerical models of salt marsh evolution: Ecological, geomorphic, and climatic factors. Reviews of Geophysics, 50(1). DOI: 10.1029/2011RG000359

Fagherazzi, S., Palermo, C., Rulli, M.C., Carniello, L., and Defina, A. (2007) Wind waves in shallow microtidal basins and the dynamic equilibrium of tidal flats. Journal of Geophysical Research 112: 2156–2202. DOI: 10.1029/2006JF000572

Foster, D.M. (1992) Environmental Impacts of Recent Dredging and Inner Shelf Spoil Disposal at Tauranga, Masters Thesis. University of Waikato, Hamilton; 230 pp.

Friedrichs, C.T. (2010). Barotropic tides in channelized estuaries Contemporary Issues in Estuarine Physics: Cambridge University Press.

Friedrichs, C.T. (2011) Tidal flat morphodynamics: a synthesis. In Treatise on Estuarine and Coastal Science: Sedimentology and Geology, Flemming B.W., Hansom J.D. (eds). Academic Press: London, United Kingdom. 137–170. DOI: 10.1016/B978-0-12-374711-2.00307-7

Friedrichs, C.T., and Aubrey, D.G. (1988) Non-linear tidal distortion in shallow well-mixed estuaries: A synthesis. Estuarine, Coastal and Shelf Science, 27(5), 521–545. DOI: 10.1016/0272-7714(88)90082 0

Friedrichs, C.T., and Aubrey, D.G. (1996) Uniform bottom shear stress and equilibrium hypsometry of intertidal flats. Washington, DC: American Geophysical Union.

Gerritsen, F., Dunsbergen, D.W., and Israel, C.G. (2003) A rational stability approach for tidal inlets, including analysis of the effect of wave action. Journal of Coastal Research, 19(4), 1066-1081.

Gilbert, F., Aller, R.C., and Hulth, S. (2003) The influence of macrofaunal burrow spacing and diffusive scaling on sedimentary nitrification and denitrification: An experimental simulation and model approach. Journal of Marine Research, vol. 61, 101-125. DOI: 10.1357/002224003321586426

Green, M.O., Black, K.P., and Amos, C.L. (1997) Control of estuarine sediment dynamics by interactions between currents and waves at several scales. Marine Geology, 144(1), 97–116. DOI: 10.1016/S0025-3227(97)00065-0

Green, M.O., and Coco, G. (2007) Sediment transport on an estuarine intertidal flat: measurements and conceptual model of waves, rainfall and exchanges with a tidal creek. Estuarine, Coastal and Shelf Science 72(4): 553–569. DOI: 10.1016/j.ecss.2006.11.006

Green, M.O., and Coco, G. (2014) Review of wave-driven sediment resuspension and transport in estuaries. Reviews of Geophysics, 52(1), 77–117. DOI: 10.1002/2013RG000437

Hansen, D.V., and Rattray, M. (1966) New Dimensions in Estuary Classification. Limnology and Oceanography, 11(3), 319-326. DOI: 10.4319/lo.1966.11.3.0319

Hanslow, D.J., Morris, B.D, Foulsham, E, and Kinsela, M.A. (2018). A regional scale approach to assessing current and potential future exposure to tidal inundation in

different types of estuaries. Nature Scientific Reports 8, 7065. DOI: 10.1038/s41598-018-25410-y

Healy, T.R., Cole, R., and de Lange, W. (1996) Geomorphology and ecology of New Zealand shallow estuaries and shorelines. In Estuarine Shores: Evolution, Environments and Human Alterations; John Wiley and Sons: Chichester, England. 115–154.

Healy, T.R., and Kirk, R.M. (1982) Coasts. In Landforms of New Zealand, Soons J.M., Selby M.J. (eds). Longman Paul Ltd: Auckland; 81–104

Heath, R.A. (1985) A review of the physical oceanography of the seas around New Zealand — 1982. New Zealand Journal of Marine and Freshwater Research 19(1): 79–124. DOI: 10.1080/00288330.2014.992918

Henderson, S.M., Norris, B.K., Mullarney, J.C., and Bryan, K.R. (2017) Wave-frequency flows within a near-bed vegetation canopy. Continental Shelf Research 147: 91–101. DOI: 10.1016/j.csr.2017.06.003

Herrling, G., and Winter, C. (2014) Morphological and sedimentological response of a mixed-energy barrier island tidal inlet to storm and fair-weather conditions. Earth Surface Dynamics, 2(1), 363–382. DOI: 10.5194/esurf-2-363-2014

Herrling, G., and Winter, C. (2015) Tidally- and wind-driven residual circulation at the multiple-inlet system East Frisian Wadden Sea. Continental Shelf Research, 106, 45–59. DOI: 10.1016/j.csr.2015. 06.001

Hiatt, M., Addink, E.A., and Kleinhans, M.G. (2021) Connectivity and directionality in estuarine channel networks. Earth Surface Processes and Landforms 2021, 1–18. DOI: 10.1002/esp.5286

Hibma, A., Stive, M.J.F., and Wang, Z.B. (2004) Estuarine morphodynamics. Coastal Engineering, 51(8), 765-778. DOI: 10.1016/j.coastaleng.2004.07.008

Horstman, E.M., Lundquist, C.J., Bryan, K.R., Bulmer, R.H., Mullarney, J.C., and Stokes, D.J. (2018) The dynamics of expanding mangroves in New Zealand. In Threats to Mangrove Forests: Hazards, Vulnerability, and Management, Makowski C., Finkl C.W. (eds), Coastal Research Library, Volume 25. Springer International Publishing: Cham, Switzerland. DOI: 10.1007/978-3-319-73016-5_2

Hu, Z.,Wang, Z.B., Zitman, T.J., Stive, M.J.F., and Bouma, T.J. (2015) Predicting long term and short-term tidal flat morphodynamics using a dynamic equilibrium theory. Journal of Geophysical Research: Earth Surface 120(9): 1803–1823. DOI: 10.1002/2015JF003486

Hume, T.M., and Herdendorf, C.E. (1988) A geomorphic classification of estuaries and its application to coastal resource management – a New Zealand example. Ocean and Shoreline Management 11(3): 249–274. DOI: 10.1016/0951-8312(88)90022-7

Hume, T.M., Green, M.O., and Elliot, S. (2010) Tauranga Harbour Sediment Study: Assessment of predictions for management (HAM2009-139). Hamilton, New Zealand: National Institute of Water & Atmospheric Research Ltd

Hume, T.M., Snelder, T., Weatherhead, M., and Liefting, R. (2007) A controlling factor approach to estuary classification. Ocean and Coastal Management 50: 905–929. DOI: 10.1016/j.ocecoaman.2007.05.009

Huang, W., and Li, C. (2019) Spatial variation of cold front wind-driven circulation and quasi-steady state balance in Lake Pontchartrain Estuary. Estuarine, Coastal and Shelf Science, 224, 154–170. DOI: 10.1016/j.ecss.2019.04.031

Hunt, S., Bryan, K.R., and Mullarney, J.C. (2015) The influence of wind and waves on the existence of stable intertidal morphology in microtidal estuaries. Geomorphology, 228, 158–174. DOI: 10.1016/j.geomorph.2014.09.001

Hunt, S., Bryan, K.R., Mullarney, J.C., and Pritchard, M. (2016) Observations of asymmetry in contrasting wave- and tidally dominated environments within a microtidal basin: Implications for estuarine morphological evolution. Earth Surface Processes and Landforms, 41(15), 2207–2222. DOI: 10.1002/esp.3985

Juarez, B., Valle-Levinson, A., Chant, R., and Li, M. (2019) Observations of the lateral structure of wind-driven flow in a coastal plain estuary. Estuarine, Coastal and Shelf Science, 217, 262–270. DOI: 10.1016/j.ecss.2018.11.018

Keesstra, S., Pedro, J., Saco, P., Parsons, T., Poeppl, R., Masselink, R., and Cerdà, A. (2018). The way forward: Can connectivity be useful to design better measuring and modelling schemes for water and sediment dynamics? Science of The Total Environment, 644, 1557–1572. DOI: 10.1016/J.SCITOTENV.2018.06.342

Kirby, R. (2000) Practical implications of tidal flat shape. Continental Shelf Research 20(10–11): 1061–1077. DOI: 10.1016/S0278-4343(00)00012-1

Kirwan, M.L., Guntenspergen, G.R., D'Alpaos, A., Morris, J.T., Mudd, S.M., and Temmerman, S. (2010) Limits on the adaptability of coastal marshes to rising sea level. Geophysical Research Letters, 37(23) DOI: 10.1029/2010GL045489

Kirwan, M., and Temmerman, S. (2009) Coastal marsh response to historical and future sea-level acceleration. Quaternary Science Reviews, 28(17), 1801-1808. DOI: 10.1016/j.quascirev.2009.02.022

Kjerfve, B. (1986) Comparative oceanography of coastal lagoons. Estuarine Variability 1986: 63–81. DOI: 10.1016/B978-0-12-761890-6.50009-5

Krauss, K., Doyle, T., Doyle, T., Swarzenski, C., From, A., Day, R., and Conner, W. (2009). Water level observations in mangrove swamps during two hurricanes in Florida. Wetlands, 29(1), 142-149. DOI: 10.1672/07-232.1

Lanzoni, S., and Seminara, S. (2002) Long-term evolution and morphodynamic equilibrium of tidal channels. Journal of Geophysical Research 107(C1): 1–13. DOI: 10.1029/2000JC000468

Laval, B.E., Imberger, J., and Findikakis, A. (2005) Dynamics of a large tropical lake: Lake Maracaibo. Aquatic Sciences, 67(3), 337–349. DOI: 10.1007/s00027-005-0778-1

Le Hir, P., Roberts, W., Cazaillet, O., Christie, M., Bassoullet, P., and Bacher, C. (2000) Characterization of intertidal flat hydrodynamics. Continental Shelf Research, 20(12–13), 1433–1459. DOI: 10.1016/S0278-4343(00)00031-5

Lesser, G.R., Roelvink, J.A., van Kester, J.A.T.M., and Stelling, G.S. (2004) Development and validation of a three-dimensional morphological model. Coastal Engineering, 51(8–9), 883–915. DOI: 10.1016/jcoastaleng.2004.07.014

Lettmann, K.A., Wolff, J.-O., and Badewien, T.H. (2009) Modeling the impact of wind and waves on suspended particulate matter fluxes in the East Frisian Wadden Sea (Southern North Sea). Ocean Dynamics, 59(2), 239–262. DOI: 10.1007/s10236-009-0194-5

Leuven, J.R.F.W., Pierik, H.J., van der Vegt, M., Bouma, T.J., and Kleinhans, M.G. (2019) Sea-level-rise-induced threats depend on the size of tide-influenced estuaries worldwide. Nature Climate Change, 9(12), 986–992. DOI: 10.1038/s41558-019-0608-4

Leuven, J.R.F.W., Selakovic, S., and Kleinhans, M.G. (2018) Morphology of bar-built estuaries: Empirical relation between planform shape and depth distribution. Earth Surface Dynamics, 6(3), 763–778. DOI: 10.5194/esurf-6-763-2018

Li, C. (2013) Subtidal water flux through a multiple-inlet system: Observations before and during a cold front event and numerical experiments. Journal of Geophysical Research, Oceans, 118(4), 1877–1892. DOI: 10.1002/jgrc.20149

Liu, C.Z., de Lange, W.P., and Bryan, K.R. (2019) Estuary rejuvenation in response to sea level rise: an example from Tairua Estuary, New Zealand. Geo-Marine Letters 40: 269-280. DOI: 10.1007/s00367-019-00603-0

Luijendijk, A.P., Ranasinghe, R., de Schipper, M.A., Huisman, B.A., Swinkels, C.M., Walstra, D.J.R., and Stive, M.J.F. (2017) The initial morphological response of the Sand Engine: A process-based modelling study. Coastal Engineering, 119, 1–14. DOI: 10.1016/j.coastaleng.2016.09.005

Maan, D.C., van Prooijen, B.C., Wang, Z.B., and de Vriend, H.J. (2015) Do intertidal flats ever reach equilibrium? Journal of Geophysical Research. Earth Surface 120(11): 2406–2436. DOI: 10.1002/2014JF003311

MacPherson, D., Fox, B.R.S., and de Lange, W.P. (2017) Holocene evolution of the southern Tauranga Harbour. New Zealand Journal of Geology and Geophysics 60(4): 392–409. DOI: 10.1080/00288306.2017.1360917.

Mariotti, G., and Fagherazzi, S. (2013) A two-point dynamic model for the coupled evolution of channels and tidal flats. Journal of Geophysical Research: Earth Surface 118(3): 1387–1399. DOI: 10.1002/jgrf.20070.

McKinney, P., Austin, J.A., and Fai, G. (2019) The wind-driven formation of cross-shelf sediment plumes in a large lake. Limnology and Oceanography, 64(3), 1309–1322. DOI: 10.1002/lno.11117

McLusky, D.S., and Elliott, M. (2004) The Estuarine Ecosystem - Ecology, Threats and Management (3rd ed.). OUP Oxford, 2004.

Meerman, C., Rottschäfer, V., and Schuttelaars, H. (2018) Influence of geometrical variations on morphodynamic equilibria in short tidal basins. Ocean Dynamics, 69(2), 221–238. DOI: 10.1007/s10236-018-1236-7

Moilanen, A. (2011) On the limitations of graph-theoretic connectivity in spatial ecology and conservation. Journal of Applied Ecology, 48(6), 1543–1547. DOI: 10.1111/j.1365-2664.2011.02062.x

Montgomery, J.M., Bryan, K.R., Mullarney, J.C., and E.M. Horstman (2019) Attenuation of storm surges by coastal mangroves, Geophysical Research Letters, 46(5), P2680-2689, DOI: 10.1029/2018GL081636

Moore, R.D., Wolf, J., Souza, A.J., and Flint, S.S. (2008) Morphological evolution of the Dee Estuary, Eastern Irish Sea, UK: a tidal asymmetry approach. Geomorphology 103: 588–596. DOI: 10.1016/j.geomorph.2008.08.003.

Morrison, M.A., Zealand, N., and Ministry of, F. (2009) A review of land-based effects on coastal fisheries and supporting biodiversity in New Zealand (Report). Wellington, NZ: Ministry of Fisheries

Mullarney, J.C., and Henderson, S.M. (2018) Flows Within Marine Vegetation Canopies. In V. Panchang and J. Kaihatu (Eds.), "Advances in Coastal Hydraulics", P1-46, World Scientific Publishing Ltd, DOI: 10.1142/9789813231283_0001

Mullarney, J.C., Henderson, S.M., Norris, B.K., Bryan, K.R., Fricke, A.T., Sandwell, D.R., and Culling, D.P. (2017) A question of scale: how turbulence around aerial roots shapes the seabed morphology in mangrove forests of the Mekong Delta. Oceanography 30(3): 34–47. DOI: 10.5670/oceanog.2017.312.

National Institute of Water and Atmospheric Research (NIWA) (2015) Tide Forcaster. http://www.niwa.co.nz/services/online-services/tideforecaster

Narvaez, D.A., and Valle-Levinson, A. (2008) Transverse structure of wind driven flow at the entrance to an estuary: Nansemond River. Journal of Geophysical Research, 113(C9), 1–9. DOI: 10.1029/2008JC004770

Newman, M.E.J. (2003) The structure and function of complex networks. SIAM Review, 45(2), 167–256. DOI: 10.1137/S003614450342480

Nichol, S.L., Augustinus, P.C., Gregory, M. ., Creese, R., and Horrocks, M. (2000) Geomorphic and sedimentary evidence of human impact on the New Zealand coastal landscape. Physical Geography, 21(2), 109-132. DOI: 10.1080/02723646.2000.10642702

Nichols, M.M., and Biggs, R.B. (1985) Estuaries. In Coastal Sedimentary Environments. Davis RA (ed.). Springer: New York; 77–186. DOI: 10.1007/978-1-4612-5078-4_2

Pawlowicz, R., Beardsley, B., and Lentz, S. (2002) Classical tidal harmonic analysis including error estimates in MATLAB using T_TIDE. Computers and Geosciences 28(8): 929–937. DOI: 10.1016/S0098-3004(02)00013-4.

Pritchard, D., Hogg, A.J., and Roberts, W. (2002) Morphological modelling of intertidal mudflats: the role of cross-shore tidal currents. Continental Shelf Research 22(11–13): 1887–1895. DOI: 10.1016/S0278-4343(02)00044-4.

Pearson, S.G., van Prooijen, B.C., Elias, E.P.L., Vitousek, S., and Wang, Z.B. (2020) Sediment connectivity: A framework for analyzing coastal sediment transport pathways. Journal of Geophysical Research, Earth Surface, 125. DOI: 10.1029/2020JF005595

Phillips, J.D., Schwanghart, W., and Heckmann, T. (2015) Graph theory in the geosciences. Earth-Science Reviews, 143, 147–160. DOI: 10.1016/j.earscirev.2015.02.002

Ponte, A.L., Gutierrez de Velasco, G., Valle-Levinson, A., Winters, K.B., and Winant, C.D. (2011) Wind-driven subinertial circulation inside a semi-enclosed bay in the Gulf of California. Journal of Physical Oceanography, 42(6), 940–955. DOI: 10.1175/JPO-D-11-0103.1

Rees, J.G. (2006) Sea-level, topographical and sediment supply controls on holocene sediment composition in the Humber estuary, UK. Philosophical Transactions of the Royal Society A. Mathematical, Physical and Engineering Sciences 364(1841): 993–1008. DOI: 10.1098/rsta.2006.1750

Ridderinkhof, H. (1997). The Effect of Tidal Asymmetries on the Net Transport of Sediments in the Ems Dollard Estuary. Journal of Coastal Research, 41-48. DOI: 10.1007/s10236-010-0329-8

Ridderinkhof, W., de Swart, H.E., van der Vegt, M., Alebregtse, N.C., and Hoekstra, P. (2014) Geometry of tidal inlet systems: A key factor for the net sediment transport in tidal inlets. Journal of Geophysical Research, Oceans, 119(10), 6988–7006. DOI: 10.1002/2014JC010226

Roberts, W., Le Hir, P., and Whitehouse, R.J.S. (2000) Investigation using simple mathematical models of the effect of tidal currents and waves on the profile shape of intertidal mudflats. Continental Shelf Research 20(10): 1079–1097. DOI: 10.1016/S0278-4343(00)00013-3

Robins, P.E., and Davies, A.G. (2010) Morphological controls in sandy estuaries: the influence of tidal flats and bathymetry on sandy transport. Ocean Dynamics, 60, pp. 503-517. DOI: 10.1007/s10236-010-0268-4

Rodil, I.F., Lohrer, A.M., Chiaroni, L.D., Hewitt, J.E., and Thrush, S.F. (2011) Disturbance of sandflats by thin terrigenous sediment deposits: consequences for primary production and nutrient cycling. Ecological Applications, 21(2), 416-426. DOI: 10.1890/09-1845.1

Roelvink, J. (2006) Coastal morphodynamic evolution techniques. Coastal Engineering 53, 277–287. DOI: 10.1016/j.coastaleng.2005.10.015

Roelvink, J. (2015) Addressing local and global sediment imbalances: Coastal sediments as rare minerals. Coastal sediments 2015, 1–13, San Diego, CA: World Scientific

Rossi, V., Ser-Giacomi, E., Lõpez, C., and Hernández-García, E. (2014) Hydrodynamic provinces and oceanic connectivity from a transport network help designing

marine reserves. Geophysical Research Letters, 41, 2883–2891. DOI: 10.1002/2014GL059540

Sanay, R., and Valle-Levinson, A. (2005) Wind-induced circulation semienclosed homogeneous, rotating basins. Journal of Physical Oceanography, 35(12), 2520–2531. DOI: 10.1175/JPO2831.1

Sinner, J., Clark, D., Ellis, J., Roberts, B., Jiang, W., Goodwin, E., . . . Brown, S. (2011) Health of Te Awanui Tauranga Harbour (Report). Palmerston North, N.Z: Manaaki Taha Moana (MTM) Research Team

Smith, S.D., and Banke, E.G. (1975) Variation of the sea surface drag coefficient with wind speed. Quarterly Journal of the Royal Meteorological Society, 101(429), 665–673. DOI: 10.1002/qj.49710142920

Speer, P.E., and Aubrey, D.G. (1985) A study of non-linear tidal propagation in shallow inlet/estuarine systems, part II: theory. Estuarine, Coastal and Shelf Science 21: 207–224. DOI: 10.1016/0272-7714(85)90096-4

Stark, J., Smolders, S., Meire, P., and Temmerman, S. (2017) Impact of intertidal area characteristics on estuarine tidal hydrodynamics: a modelling study for the Scheldt estuary. Estuarine, Coastal and Shelf Science 198: 138–155. DOI: 10.1016/j.ecss.2017.09.004

Stokes, D.J., Healy, T.R., and Cooke, P.J. (2010) Expansion dynamics of monospecific, temperate mangroves and sedimentation in two embayments of a barrier-enclosed lagoon, Tauranga harbour, New Zealand. 26, 113–122. DOI: 10.2112/08-1043.1

Sutherland, J., Peet, A.H., and Soulsby, R.L. (2004) Evaluating the performance of morphological models. Coastal Engineering 51(8–9): 917–939. DOI: 10.1016/j.coastaleng.2004.07.015

Talke, S.A., and Stacey, M.T. (2008) Suspended sediment fluxes at an intertidal flat: The shifting influence of wave, wind, tidal, and freshwater forcing. Continental Shelf Research, 28(6), 710–725. DOI: 10.1016/j.csr.2007.12.003

Tang, M., and Kristensen, E. (2007) Impact of microphytobenthos and macroinfauna on temporal variation of benthic metabolism in shallow coastal sediments. Journal of experimental marine biology and ecology, 349(1), DOI: 99-112. 10.1016/j.jembe.2007.05.011

Tay, H.W., Bryan, K.R., Pilditch, C.A., Park, S., and Hamilton, D.P. (2012) Variations in nutrient concentrations at different time scales in two shallow tidally dominated estuaries. Marine and Freshwater Research 63(2): 95–109. DOI: 10.1071/MF11102

Tay H.W., Bryan K.R., de Lange W.P., and Pilditch, C.A. (2013) The hydrodynamics of the southern basin of Tauranga Harbour. New Zealand Journal of Marine and Freshwater Research 47(2): 249–274. DOI: 10.1080/00288330.2013.778300

Temmerman, S., de Vriend, H.J., Herman, P.M.J., Ysebaert, T.J.W., Meire, P., and Bouma, T.J. (2013) Ecosystem-based coastal defence in the face of global change. Nature 504(7478): 79–83. DOI: 10.1038/nature12859

Thrush, S.F., Hewitt, J.E., Cummings, V.J., Ellis, J.I., Hatton, C., Lohrer, A., . . . Göteborgs, U. (2004) Muddy Waters: Elevating Sediment Input to Coastal and Estuarine Habitats. Frontiers in Ecology and the Environment, 2(6), 299-306. DOI: 10.1890/1540-9295(2004)002

Townend, I. (2004). Identifying change in estuaries. Journal of Coastal Conservation, 10(1), 5-12. DOI: 10.1652/1400-0350

Townend, I. (2005) An examination of empirical stability relationships for UK estuaries. Journal of Coastal Research 21(5): 1042–1053. DOI: 10.2112/03-0066R.1

Townend, I. (2008) Hypsometry of estuaries, creeks and breached sea wall sites. Maritime Engineering 161: 23–32. DOI: 10.1680/maen.2008.161.1.23

Townend, I. (2010) An exploration of equilibrium in Venice lagoon using an idealised form model. Contintental Shelf Research 30(8): 984–999. DOI: 10.1016/j.csr.2009.10.012

Townend, I. (2012) The estimation of estuary dimensions using a simplified form model and the exogenous controls. Earth Surface Processes and Landforms 37(15): 1573–1583. DOI: 10.1002/esp.3256

Townend, I., and Pethick, J. (2002) Estuarine flooding and managed retreat. Philosophical Transactions of the Royal Society of London. Series A: Mathematical, Physical and Engineering Sciences, 360(1796), 1477-1495. DOI: 10.1098/rsta.2002.1011

van der Werf, J., Reinders, J., van Rooijen, A., Holzhauer, H., and Ysebaert, T. (2015) Evaluation of a tidal flat sediment nourishment as estuarine management measure. Ocean and Coastal Management, 114, 77–87. DOI: 10.1016/j.ocecoaman.2015.06.006

van Maanen, B., Coco, G., and Bryan, K.R. (2013) Modelling the effects of tidal range and initial bathymetry on the morphological evolution of tidal embayments. Geomorphology 191: 23–34. DOI: 10.1016/j.geomorph.2013.02.023

van Maanen, B., Coco, G., and Bryan, K.R. (2015) On the ecogeomorphological feedbacks that control tidal channel network evolution in a sandy mangrove setting. Proceedings of the Royal Society A: Mathematical, Physical and Engineering Science, 471(2180), 20150115. DOI: 10.1098/rspa.2015.0115

van Maren, D.S., Van Kessel, T., Cronin, K., and Sittoni, L. (2015) The impact of channel deepening and dredging on estuarine sediment concentration. Continental Shelf Research 95(1): 1–14. DOI: 10.1016/j.csr.2014.12.010

van Maren, D.S., and Winterwerp, J.C. (2012) The role of flow asymmetry and mud properties on tidal flat sedimentation. Continental Shelf Research 60: 71–84. DOI: 10.1016/j.csr.2012.07.010

van Rijn, L.C. (1993). Principles of Sediment Transport in Rivers, Estuaries and Coastal Seas. Aqua Publications, The Netherlands.

van Santen, P., Augustinus, P.G.E.F., Janssen-Stelder, B.M., Quartel, S., and Tri, N.H. (2007) Sedimentation in an estuarine mangrove system. Journal of Asian Earth Sciences 29: 566–575. DOI: 10.1016/j.jseaes.2006.05.011

van Sebille, E., Delandmeter, P., Schofield, J., Hardesty, B.D., Jones, J., and Donnelly, A. (2019) Basin-scale sources and pathways of microplastic that ends up in the Galapagos Archipelago. Ocean Sci. 15, 1341–1349. DOI: 10.5194/os-15-1341-2019

Vermeulen, T.J. (2003) Sensitivity Analysis of Fine Sediment Transport in the Humber Estuary, Master Thesis. Delft University of Technology.

Wang, Z.B., Elias, E.P., van der Spek, A.J., and Lodder, Q.J. (2018) Sediment budget and morphological development of the Dutch Wadden Sea: Impact of accelerated sea-level rise and subsidence until 2100. Netherlands Journal of Geosciences, 97(03), 183–214. DOI: 10.1017/njg.2018.8

Wang, Z.B., Jeuken, M.C.J.L., Gerritsen, H., de Vriend, H.J., and Kornman, B.A. (2002) Morphology and asymmetry of the vertical tide in the Westerschelde estuary. Continental Shelf Research 22(17): 2599–2609. DOI: 10.1016/S0278-4343(02)00134-6

Weisberg, R.H., and Zheng, L. (2006) Circulation of Tampa Bay driven by buoyancy, tides, and winds, as simulated using a finite volume coastal ocean model. Journal of Geophysical Research, 111(C1), C01005. DOI: 10.1029/2005JC003067

White, J.W., Carr, M.H., Caselle, J.E., Washburn, L., Woodson, C.B., Palumbi, S.R., Carlson, P.M., Warner, R.R., Menge, B.A., Barth, J.A., Blanchette, C.A., Raimondi, P.T., and Milligan, K. (2019) Connectivity, dispersal, and recruitment: connecting benthic communities and the coastal ocean. Oceanography 32 (3), 50–59. DOI: DOI:10.5670/oceanog.2019.310

Whitehouse, R.S.R., Roberts, W., and Mitchener, H. (2000) Dynamics of estuarine muds : a manual for practical applications. Wallingford, UK: HR Wallingford

Wohl, E., Brierley, G., Cadol, D., Coulthard, T.J., Covino, T., and Fryirs, K.A. (2019) Connectivity as an emergent property of geomorphic systems. Earth Surface Processes and Landforms, 44(1), 4–26. DOI: 10.1002/esp.4434

Wolters, M., Bakker, J.P., Bertness, M.D., Jefferies, R.L., and Möller, I. (2005) Saltmarsh Erosion and Restoration in South-East England: Squeezing the Evidence Requires Realignment. Journal of Applied Ecology, 42(5), 844-851. DOI: 10.1111/j.1365-2664.2005.01080.x

Wong, K.C. (1994) On the nature of transverse variability in a coastal plain estuary. Journal of Geophysical Research, 99(C7), 14209–14222. DOI: 10.1029/94JC00861

Wong, K.C., and Valle-Levinson, A. (2002) On the relative importance of the remote and local wind effects on the subtidal exchange at the entrance to the Chesapeake Bay. Journal of Marine Research, 60(3), 477–498. DOI: 10.1357/002224002762231188

Wong, P. P. et al. in Climate Change 2014: Impacts, Adaptation, and Vulnerability (eds Field, C. B. et al.) 361–409 (IPCC, Cambridge Univ. Press, 2014)

Woodin, S.A., Wethey, D.S., Hewitt, J.E., and Thrush, S.F. (2012) Small scale terrestrial clay deposits on intertidal sandflats: Behavioral changes and productivity

reduction. Journal of experimental marine biology and ecology, 413, 184-191. DOI: 10.1016/j.jembe.2011.12.010

Woodroffe, C.D., Chappell, J.M.A., Thom, B.G., and Wallensky, E. (1989) Depositional model of a macrotidal estuary and flood plain, South Alligator River, Northern Australia: Sedimentology 36, 737-756. DOI: 10.1111/j.1365-3091.1989.tb01743.x

Yu, J., Zhang, X., Feng, Y., Jiang, W., and Deng, F. (2021) Analysis of tidal-induced connectivity among coastal regions in the Bohai Sea using the complex network theory. Estuarine, Coastal and Shelf Science 260. DOI: 10.1016/j.ecss.2021.107506

Zarzuelo, C., López-Ruiz, A., Díez-Minguito, M., and Ortega-Sánchez, M. (2016) Tidal and subtidal hydrodynamics and energetics in a constricted estuary. Estuarine, Coastal and Shelf Science 185: 55–68. DOI: 10.1016/j.ecss.2016.11.020

Zhou, Z., Chen, L.Y., Townend. I., Coco, G., Friedrichs, C., and Zhang, C.K. (2018) Revisiting the relationship between tidal asymmetry and basin morphology: a comparison between 1D and 2D models. Journal of Coastal Research 85: 6–10. DOI: 10.2112/SI85-003.1

Zhou, Z., Coco, G., Townend, I., Gong, Z., Wang, Z.B., and Zhang, C.K. (2018) On the stability relationships between tidal asymmetry and morphologies of tidal basins and estuaries. Earth Surface Processes and Landforms, 43(9), 1943–1959. DOI: 10.1002/esp.4366

Zhou, Z., Coco, G., Townend, I., Olabarrieta, M., van der Wegen, M., Gong, Z., D'Alpaos, A., Gao, S., Jaffe, B.E., Gelfenbaum, G., He, Q., Wang, Y., Lanzoni, S., Wang, Z., Winterwerp, H., and Zhang, C. (2017) Is "Morphodynamic Equilibrium" an oxymoron? Earth-Science Reviews 165: 257–267. DOI: 10.1016/j.earscirev.2016.12.002.

Zhou, Z., Coco, G., van der Wegen, M., Gong, Z., Zhang, C.K., and Townend, I. (2015) Modeling sorting dynamics of cohesive and noncohesive sediments on intertidal flats under the effect of tides and wind waves. Continental Shelf Research, 104, 76–91. DOI: 10.1016/j.csr.2015.05.010